ISSP

ACTIVITY REPORT OF SYNCHROTRON RADIATION LABORATORY

2021

Activity Report 2021
TABLE OF CONTENTS

10) **ELECTRONIC STATES OF FUNCTIONAL MATERIALS IN HYDROGEN ADSORPTION/DESORPTION STUDIED BY AMBIENT PRESSURE SOFT X-RAY PHOTOELECTRON SPECTROSCOPY**

Takanori Koitaya, Susumu Yamamoto, Iwao Matsuda, Jun Yoshinobu and Toshihiko Yokoyama

11) **O K-edge soft X-ray emission spectroscopy of the solvents in electrolyte solutions for redox flow batteries**

Eiji Hosono, Daisuke Asakura, Akihiro Ohira, Wenxiong Zhang, Naoya Kurahashi, Ralph J. Ugalino, Hisao Kiuchi, and Yoshihisa Harada

12) **Co L3-edge Soft X-ray Emission spectroscopy of LiCoO2 for Li-ion batteries**

Daisuke Asakura, Eiji Hosono, Kosuke Yamazoe, Naoya Kurahashi, Ralph J. Ugalino, Hisao Kiuchi, and Yoshihisa Harada

13) **REAL-TIME OBSERVATION OF HYDROGEN-ABSORPTION PROCESS IN PD-AU ALLOYS BY OPERANDO AP-XPS**

Takanori KOITAYA, Susumu YAMAMOTO, Masafumi HORIO, Iwao MATSUDA, Jun YOSHINOBU, and Toshihiko YOKOYAMA

14) **HALF-METALLIC ELECTRONIC STATES OF BULK-SINGLE CRYSTAL Co2MnZ (Z = Ge AND Ga) HEUSLER ALLOYS PROBED BY RESONANT INELASTIC SOFT X-RAY SCATTERING (SX-RIXS) IN A MAGNETIC FIELD**

Rie Y. Umetsu, Hidenori Fujiwara, Jun Miyawaki, Rika Kasahara, Takuma Nishioka, Akane Ose, Akira Sekiyama, Yoshihisa Harada and Shigemasa Suga

15) **KINETIC SQUARE SCHEME IN OXYGEN-REDOX BATTERY ELECTRODES**

Masashi OKUBO

16) **ORBITAL TORQUE IN COFE/CU/AL2O3: INVESTIGATION ON THE LARGE TORQUE WITHOUT HEAVY ELEMENT**

Junyeon KIM

17) **MAGNETIC STATE OF VNB3S6 DETERMINED BY X-RAY MAGNETIC CIRCULAR DICHROISM**

Masafumi HORIO, Tomoaki SENOO, Tetsuya WADA, Yasuyuki HIRATA, Shota OKAZAKI, Takao SASAGAWA, Iwao MATSUDA

18) **MEASUREMENT OF X-RAY MAGNETIC LINEAR DICHROISM BY ROTATING POLARIZATION ANGLE OF SOFT X-RAY GENERATED BY A SEGMENTED CROSS UNDULATOR**

Masafumi HORIO, Yoshiki KUDO, Toshihide SUMI, Tetsuya WADA, Yasuyuki HIRATA, Kohei YAMAMOTO, Takuo OHKOCHI, Toyohiko KINOSHITA, Iwao MATSUDA

19) **DEVELOPMENT OF ANGLE-RESOLVED SOFT X-RAY EMISSION SPECTROSCOPY**

Naoya Kurahashi, Jun Miyawaki, Kosuke Yamazoe and Yoshihisa Harada

20) **CHARGE EXCITATION RESEARCH ON THE T* PHASE HOLEDOPED CUPRATES BY RESONANT SOFT X-RAY SCATTERING**

Xie PEIAO, Shinnosuke KITAYAMA, Takanori TANIGUCHI, Hisao KIUCHI, Kenji ISHII, and Masaki FUJITA

21) **Co L3-edge Soft X-ray Emission spectroscopy of La0.6Sr0.4CoO3-♎ for solid oxide fuel cells**

Daisuke Asakura, Eiji Hosono, Tomohiro Ishiyama, Riyan Achmad Budiman, Haruo Kishimoto, Kosuke Yamazoe, Naoya Kurahashi, Ralph J. Ugalino, Hisao Kiuchi, and Yoshihisa Harada

22) **POSSIBLE ANAPOLE ORDER IN THE ANTIFERROMAGNETIC PHASE OF MULTIFERROIC CUO**

Ryusuke MISAWA, Keito ARAKAWA, Hiroki UEDA, Jun MIYAWAKI, Hisao KIUCHI, Yoshihisa HARADA, Yoshikazu TANAKA, and Tsuyoshi KIMURA

23) **ELECTRONIC STRUCTURE ANALYSIS OF OXYFLUORIDE CATHODE OF ALL-SOLID-STATE FLUORIDE BATTERY USING RESONANT INELASTIC X-RAY SCATTERING**

Kentaro YAMAMOTO, Datong ZHANG, Hisao KIUCHI, Jun MIYAWAKI, Tomoki UCHIYAMA, Toshiki WATANABE, Tsuyoshi TAKAMI, Toshiyuki MATSUNAGA, Yoshihisa HARADA, Yoshiharu UCHIMOTO

24) **OPERANDO AMBIENT PRESSURE PHOTOELECTRON SPECTROSCOPY OF CHEMICAL REACTION ON THE FUNCTIONALIZED BASAL AND EDGE SURFACES OF MoS_2**

F. OZAKI, Y. CHOI, H. Li, Y. SAWAGUCHI, S. TANAKA, K. MUKAI, M. HORIO, I. MATSUDA and J. YOSHINOBU

25) **ELECTRONIC STATE ANALYSIS OF EARTH-ABUNDANT FE–AL–SI THERMOELECTRIC (FAST) MATERIALS USING SCANNING PHOTOELECTRON MICROSCOPY**

Yoshiki TAKAGIWA, Shunsuke TSUDA, Naoka NAGAMURA, Asako YOSHINARI, Shingo TAKEZAWA, Kenta OISHI, Kentaro FUKU, Wenxiong ZHANG

26) **ANALYSIS OF WATER STRUCTURE OF THERMORESPONSIVE POLYMER MODIFIED INTERFACE**

Kenichi NAGASE, Naoya KURAHASHI, Hisao KIUCHI, Yoshihisa HARADA

27) **RESONANT INELASTIC X-RAY SCATTERING SPECTROSCOPY OF CU-PROTEINS**

Kentaro FUJII, Jun MIYAWAKI, Naoya KURAHASHI, Hisao, KIUCHI, Yoshihisa HARADA, Motoyasu ADACHI, Akinari YOKOYA

Experiments at E-Labo

1) **STUDY ON THE HELICAL SPIN TEXTURE OF TOPOLOGICAL SURFACE STATE IN SUPERCONDUCTOR 2M-WS2**

Soonsang Huh, Soohyun Cho, Hua Bai, Yuqiang Fang, Fuqiang Huang, Yuto Fukushima, Ayumi Harasawa, Yunhao Lu, Gang Mu and Dawei Shen and Takeshi Kondo

2) **ENHANCED RASHBA-SPLITTING OF AU(111) SURFACE STATES BY THE MELAMINE HONEYCOMB LAYERS**

Rena MOUE, Yuta KOKUBO, Kozo MUKAI, Hirotaka MIZUSHIMA, Yuto FUKUSHIMA, Kaishu KAWAGUCHI, Takeshi KONDO, Ayumi HARASAWA, Jun YOSHINOBU, Shik SHIN, Kaname KANA

3) **ELECTRONIC STATES OF TOPOLOGICAL SEMIMETALS STUDIED BY SPIN- AND ANGLE-RESOLVED PHOTOEMISSION**

Y.X. Wan, K. Kuroda, C. Bareille, Y. Ishida, A. H. Mayo, H. Takahashi , M. S. Bahramy, C. Lin, Y. Arai, H. Tanaka, Y.Y. Dong, M. Hashimoto, D.H. Lu, T. Muro, S. Ishiwata, T. Kondo

4) **LASER-SARPES STUDY OF SPIN-POLARIZED ELECTRONIC STATES FOR PB(BI1-XSBX)2TE4**

Koichiro YAJI, Yuya HATTORI, Shunsuke YOSHIZAWA, Shunsuke TSUDA, Youhei YAMAJI, Yuto FUKUSHIMA, Kaishu KAWAGUCHI, Takeshi KONDO, Yuki TOKUMOTO, Keiichi EDAGAWA, and Taichi TERASHIMA

5) **ELECTRONIC STRUCTURES OF HALF-METALLIC FERROMAGNET La1-xSrxMnO3 BY HIGH-RESOLUTION SPINRESOLVED PHOTOEMISSION SPECTROSCOPY**

T. Setoguchi, N. Kataoka, K. Kawaguchi, Y. Fukushima, A. Harasawa, K. Kuroda, T. Kondo, S. Shin, T. Wakita, Y. Muraoka, and T. Yokoya

5 **Staff**

6 **Publication List**

Preface

The Synchrotron Radiation Laboratory (SRL) of the Institute for Solid State Physics (ISSP) has been cooperating with the Synchrotron Radiation Research Organization of the University of Tokyo to operate the BL07LSU soft X-ray beamline and its experimental end stations at SPring-8 since 2006. The beamline has a 27-m-long polarization-controlled undulator and monochromator covering the photon energy range from 250 eV to 2 keV, with an average photon flux of 10^{12} photons/s. Since 2009, the SRL staff has been playing an essential role in promoting the ISSP's joint research program for domestic and international users of the BL07LSU. The three end stations—ambient pressure X-ray photoemission spectroscopy, three dimensional nanoESCA, and the high-resolution soft X-ray emission spectroscopy stations—have excellent ability to operate under high pressure (~20 mbar), high spatial resolution (~70 nm), and high energy resolution ($E/\Delta E \approx 10{,}000$), respectively. During FY2021, as the COVID-19 pandemic persisted, we conducted joint research experiments while applying infection control measures in accordance with the SPring-8 facility policy. All of the experiments were carried out as scheduled, except for those involving the international user groups, who could not come to Japan. We thus conducted the experiments on their behalf via remote connection.

To utilize the characteristics of BL07LSU, new challenges were undertaken, including the first observation of rotational X-ray magnetic linear dichroism (XMLD), which is a soft X-ray magneto-optical measurement during rotation of the angle of the linearly polarized beam and the X-ray magneto-optical Kerr effect when utilizing polarization switching. A soft X-ray XAFS imaging experiment has been launched using a 50 nm focused beam produced by a Walter-type soft X-ray focusing mirror system. This experiment serves as both research and development for the next-generation synchrotron radiation facility in Sendai and a way to take advantage of the characteristics of BL07LSU. A high-resolution soft X-ray charge-coupled device detector has been introduced for soft X-ray emission spectroscopy to obtain a resolution of $E/\Delta E > 10000$. The ambient-pressure photoemission spectroscopy system has also been improved to increase the measurement pressure to 100 Torr. All of these improvements were made as part of research and development for the upcoming synchrotron radiation facility. We have also expanded our activities to include the time-resolved soft X-ray magneto-optical effect and nonlinear spectroscopy experiments using a focused beam of several hundred nanometers at the X-ray free electron laser facility SACLA.

The SRL will terminate the joint research program at SPring-8 in the first half of 2022 and transfer most of the instruments to the new facility. In addition, SRL will continue to develop a novel soft X-ray imaging system that can most effectively make use of the new light source.

In addition to the cutting-edge activities using synchrotron radiation and SACLA, the SRL has promoted the scientific use of laser-based high-harmonic generation in the vacuum ultraviolet and soft X-ray regions at the Kashiwa campus. Since 2015, the SRL has operated a joint research program of the high-resolution laser spin- and angle-resolved photoelectron

spectroscopy (SARPES) system, which is designed to provide high-energy (1.7 meV) and -angular resolutions with high-efficiency spin detectors for various types of solids, such as spin-orbit coupled materials and ferromagnetic materials.

Our goal is to provide users with a platform that uses both synchrotron radiation and high-harmonic laser generation through strong collaboration with other LASOR group members.

June 30, 2022

Yoshihisa Harada

Director of SRL-ISSP

1. Status of Beamline BL07LSU at SPring-8

The University-of-Tokyo high-brilliance synchrotron soft X-ray outstation beamline BL07LSU at SPring-8 has been maintained by the permanent staff members with adjuncts for user operations. The scientific aim of the beamline is to promote advanced spectroscopy for solid state and soft (including bio-) materials. There are three regular endstations for ambient pressure X-ray photoelectron spectroscopy, 3D-scanning photoelectron microscope (3D nano-ESCA) and high-resolution soft X-ray emission spectroscopy (HORNET) that are open for users. There is also a free port station for users who bring in their own experimental apparatus.

The beamline BL07LSU is equipped with a segmented cross-type undulator. Circularly and linearly polarized soft X-rays can be used in user experiments at full energy range (250 – 2000 eV). By using phase shifters between the neighboring undulator segments, polarization of the soft X-ray beam is regulated continuously and the switching frequency can be tuned up to 13 Hz. At the end-stations, various scientific experiments were carried out by both the laboratory staffs and users with applications of G-type (general), S-type (special), or P-type (priority). A user group of the S-type spends the long-term beamtime to pursue the challenging issues in synchrotron radiation research. A user team of the P-type proceeds an experiment mainly for developing technologies of beamline and end-station for the next generation light source.

It should be mentioned that the coronavirus (COVID-19) pandemic has continuously been a serious issue in 2021. Safety and health of users at the beamline have been taken care during their beamtime experiment at the end-station.

Status of the individual end-stations are briefly described below.

(1) Ambient-pressure X-ray photoelectron spectroscopy (AP-XPS)

AP-XPS station is aimed mainly for *operando* observations of catalytic reactions at the gas/solid interface. The AP-XPS system is equipped with a differentially pumped electron analyzer (SPECS, PHOIBOS 150 NAP) and an ambient pressure gas cell. XPS measurements can be performed both under ultrahigh vacuum and in near-ambient gas pressure up to 100 mbar. Reactant and product molecules of a catalytic reaction are monitored by mass spectrometer and, simultaneously, chemical states of the reaction intermediates at a surface can be examined by AP-XPS.

In 2021, a variety of research projects was conducted at the AP-XPS station, for example, *operando* observations of hydrogen permeations at metal alloys and of catalytic reactions at model surfaces.

(2) 3D-scanning photoelectron microscope (3D-nanoESCA)

3D-nanoESCA can be used for sub-100 nm range microscopic 2D mapping and depth profile of the chemical structure of functional materials and devices. In 2021, visible light responsive Al-doped $SrTiO_3$ photocatalytic particles and $BaTaO_2N$ photocatalytic particles, developed by Prof. Hisatomi group at Shinshu University, were measured to capture changes in band alignment by single-particle measurements. A core-level shift reflecting the Fermi energy shift caused by a change in catalytic efficiency was successfully monitored. As a demonstration study of the next-generation operando spectromicroscopy system with a piezoelectric four-tip unit, the potential distribution of single-layer CVD graphene on a p^+-Si/SiO_2 substrate was measured under an electric field applied to the probe, where the probe was fixed to a sample holder. As a result, a clear peak shift was detected only in the vicinity of the tip contact, suggesting a potential drop at the domain boundary.

(3) Ultra high-resolution soft X-ray emission spectroscopy (HORNET)

The station is dedicated for soft X-ray emission (or resonant inelastic X-ray scattering: RIXS) spectroscopy measurements with high-resolution ($E/\Delta E > 10{,}000$) and under various environmental conditions (gas, liquid, and solid).

In the beginning of this term, new soft X-ray CCD detector with ultra-high spatial resolution (< 5mm) for next-generation synchrotron radiation (NanoTerasu) was introduced. Although the total resolution was only slightly improved due to the limited beam size on the sample, it is expected that the resolution at NanoTerasu will be approximately three times higher than the current improvement.

HORNET station was used for studies on temperature-dependent water hydrogen-bond behavior in electrolyte membranes, spin polarization in half metals by RIXS-MCD, demonstration of soft x-ray inelastic diffraction, CO_2 sorption process in PDMS for silicon materials. Two abroad applications (RIXS-MCD of CrX_3 and dd excitation observation of Fe-Co spinel materials) were conducted remotely. As part of the New Academic Field Research, outstanding results were obtained in the study of a water molecule confined in C_{60}, and ionization of ultrafine water upon adsorption to hydrophilic and hydrophobic surfaces.

(4) Soft X-ray imaging (Free-port station)

This year, we developed a new soft X-ray ptychography system at the free-port station. The reflecting surface of the Wolter mirror, which was covered with Au, enables seamless

ptychographic measurements in a wide energy range of soft X-rays at BL07LSU.

A soft X-ray ptychographic system with a total-reflection Wolter mirror achieved a resolution of approximately 50 nm in a test chart evaluation. We have also shown that it is possible to visualize the microstructure of a mammalian cell over a wide photon energy range without chromatic aberration. Furthermore, taking advantage of the long working distance of the optical system, stereo imaging with a large rotation angle was also attempted to measure the cell sample. Ptychographic imaging with a pink beam from the undulator was also possible.

The soft X-ray ptychography system based on the Wolter mirror optics is expected to be highly effective for investigating thick samples with complex three-dimensional structures and chemical compositions.

2． Status of SARPES

Spin and angle-resolved photoemission spectroscopy (SARPES) is a powerful experimental technique to reveal various information about the occupied electronic states in solids, including their energy, momentum, and spin. In recent years, the demand for spin-resolved measurements has been getting high because of much interest in Rashba surface states and topological materials with spin-polarized electronic structures derived from strong spin-orbit interactions. These experiments require high energy resolution and enough photoelectron yield rates to detect their small energy scales (~several meV). Following these demands and requirements, we have developed a high-energy resolution SARPES apparatus using a vacuum-ultraviolet (6.994-eV) laser and very-low-energy-electron-diffraction (VLEED) type spin detectors at the Laser and Synchrotron Research Center (LASOR) in the Institute for Solid State Physics (ISSP) [1]. Our SARPES apparatus is currently utilized to obtain precise information on fine distributed spin-dependent electronic structures near the Fermi level in solids. We started the project to construct the laser-SARPES apparatus in FY 2014 and joint research at this station started in FY2015.

Our laser-SARPES apparatus consists of an analysis chamber, a carousel sample-bank chamber connected to a load-lock chamber, and a molecular beam epitaxy (MBE) chamber. All of these chambers are connected via UHV gate valves. Figure 1 represents the hemispherical electron analyzer, which is a custom-made ScientaOmicron DA30-L, modified to attach the VLEED type spin detectors. The electrons are currently excited by 6.994-eV photons, yielded by the 6th harmonic of a high-power Nd:YVO_4 quasi-continuous wave laser. A helium discharge lamp (VG Scienta, VUV5000) is also available as a photon source. At the MBE chamber, samples can be heated by a direct current heating or electron bombardment. The surface evaluating and preparing instruments, such as evaporators, low energy electron diffraction, sputter-gun, and quartz microbalance can be installed. At the carousel chamber, 16-samples can be stocked in the UHV environment. Spin-polarized states were investigated in both bulk and surface of various topological materials including magnetic and superconducting ones, atomic layers, and ferromagnetic compounds.

Spin-resolved technique with highly efficient photoelectron yield rates has advantages not only in high-resolution measurements but also in time-resolved

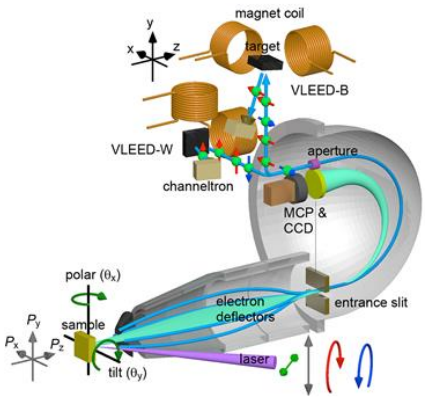

Figure 1: The laser-SARPES apparatus at LASOR in ISSP [1]. The double VLEED spin detectors are attached to a hemispherical analyzer (DA30-L, ScientaOmicron). Currently, 7-eV laser for high energy resolution measurement and 10.7eV pulsed laser for pump- probe measurements are available.

measurements based on pump-probe methods. A combination of SARPES with pump-probe laser techniques makes it possible to image the optically excited spin-polarized electron population in the unoccupied bands in energy-momentum space and track the dynamics of charge and spin in the ultrafast time-domain, which is useful for studying novel optical responses of many materials such as topological and spin-valley materials. Since FY2018, we have started to upgrade our laser-SAPRES apparatus by combining a pomp-probe laser, setting up the system named time-resolved SARPES (tr-SARPES). This project requires a short pulse laser, and thus we newly installed a pulsed 10.7-eV laser system [2,3] developed by the Kobayashi group at ISSP's LASOR. This fundamental laser system is ytterbium fiber-based, achieving a 270-fs, 1-MHz repetition rate, and high power by a chirped pulse amplification technique, which allows the pump-probe measurements with high photoelectron yield rates. In addition to a great capability of the time-resolution, our 10.7-eV laser gives more wide momentum information in contrast to the low photon energy sources such as 7-eV.

The development progressed, and now tr-SARPES measurements have been realized. The 10.7-eV laser as the probe photon is obtained as the third harmonic generation in Xe gas, and a unique Xe gas chamber has been developed for the system up to the monochromatization and the focusing system. In addition, the light polarization of the 10.7-eV laser can be selectively controlled by MgF_2 half-wave plate. The pump photon is selectable from 1.19-eV or 2.38-eV for a wide variety of band-gap materials. The beamline is designed as a vacuum chamber after 10.7-eV generation, and it is connected to the UHV analyzer chamber through a differential pumping system without a vacuum window. Furthermore, some mirror and lens in the vacuum beamline are movable, allowing the system to switch between 7-eV and 10.7-eV beamlines. In this way, this system has made tr-SARPES possible, which is demonstrated in Fig. 2. This state-of-the-art tr-SARPES apparatus can be widely used for studying unoccupied electronic states in spintronics materials and their ultrafast carrier/spin dynamics.

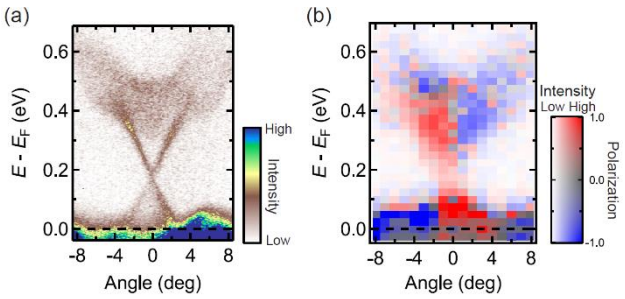

Figure 2: Time-resolved ARPES (a) and tr-SARPES mapping (b) of unoccupied topological surface state in Sb_2Te_3, observed by 10.7-eV laser after 1.19-eV laser pumping.

References:

[1] K. Yaji, A. Harasawa, K. Kuroda, S. Toyohisa, M. Nakayama, Y. Ishida, A. Fukushima, S. Watanabe, C.-T. Chen, F. Komori and S. Shin, Rev. Sci. Instrum. 87, 053111 (2016).

[2] Z. Zhao and Y. Kobayashi, Opt. Exp. 25, 13517 (2017).

[3] Z. Zhao, K. Kuroda, A. Harasawa, T. Kondo, S. Shin and Y. Kobayashi, Chin. Opt. Lett. 17, 051406 (2019).

3. Seminar

(ISSP Lectures by Visiting Professors)
Date: May 13, 2021
Title: Surface hydration and biocompatibility
Speaker: Dr. Tomohiro Hayashi (Tokyo Institute of Technology)

(ISSP Colloquiums)
Date: December 20, 2021
Title: A new approach of X-ray microscopy using high-precision optical devices
Speaker: Dr. Takashi Kimura (ISSP, The University of Tokyo)

(LASOR Seminar)
Date: January 19, 2022
Title: Study of strongly correlated systems by complementary use of vacuum-ultra-violet and soft x-ray photoemission spectroscopy
Speaker: Dr. Masafumi Horio (ISSP, The University of Tokyo)

Operando measurement of ethanol steam reforming reaction on Ni(111) using ambient pressure X-ray photoelectron spectroscopy

Susumu Yamamoto[1,2], Kota Moriyama[3]

[1] *International Center for Synchrotron Radiation Innovation Smart (SRIS), Tohoku University*

[2] *Institute of Multidisciplinary Research for Advanced Materials (IMRAM), Tohoku University*

[3] *Department of Electrical, Information and Physics Engineering, School of Engineering, Tohoku University*

Ethanol steam reforming (ESR) reaction, which produces hydrogen from ethanol (CH_3CH_2OH (EtOH) + $3H_2O \rightarrow 2CO_2 + 6H_2$), has attracted much attention toward the realization of a hydrogen society. However, the reaction mechanism of the ESR reaction is not fully understood. This is mainly because there are many side reactions in the ESR reaction, which produce various molecules such as CH_4, C_2H_4, CO. To elucidate the reaction path and reaction mechanism of the ESR reaction, we performed *operando* measurements of the ESR reaction using ambient pressure X-ray photoelectron spectroscopy (AP-XPS).

The experiments were performed using the AP-XPS system installed at SPring-8 BL07LSU [1-4]. The Ni(111) surface was cleaned by a cycle of Ar^+ ion sputtering and annealing, and used as a catalyst for the ESR reaction. The Ni(111) catalyst was placed in the mixed gas atmosphere of 3 mbar EtOH and 9 mbar H_2O, and was heated from 300 K to 700 K. For comparison, the Ni(111) catalyst was heated in the pure gas atmosphere of 3 mbar EtOH (or 9 mbar H_2O). The catalytic activity was monitored by mass spectrometry (MS), and the surface chemical states and surface adsorbed molecules of the Ni catalyst were measured by AP-XPS.

Figure 1 shows the catalytic activity of Ni(111) in the mixed gas of EtOH and H_2O as a function of temperature. At 600-700 K, the formation of H_2 and CO_2 is confirmed. The MS and AP-XPS results for EtOH + H_2O and pure EtOH were almost identical. This indicated that EtOH decomposition, one of the elementary processes of the ESR reaction, was the dominant process in the current reaction conditions. Furthermore, in the Ni 2*p* AP-XPS spectra, the Ni surface was oxidized only when EtOH was introduced, and the surface oxidation/reduction coincided with EtOH introduction/decomposition, indicating that EtOH acts as an oxidant on the Ni surface.

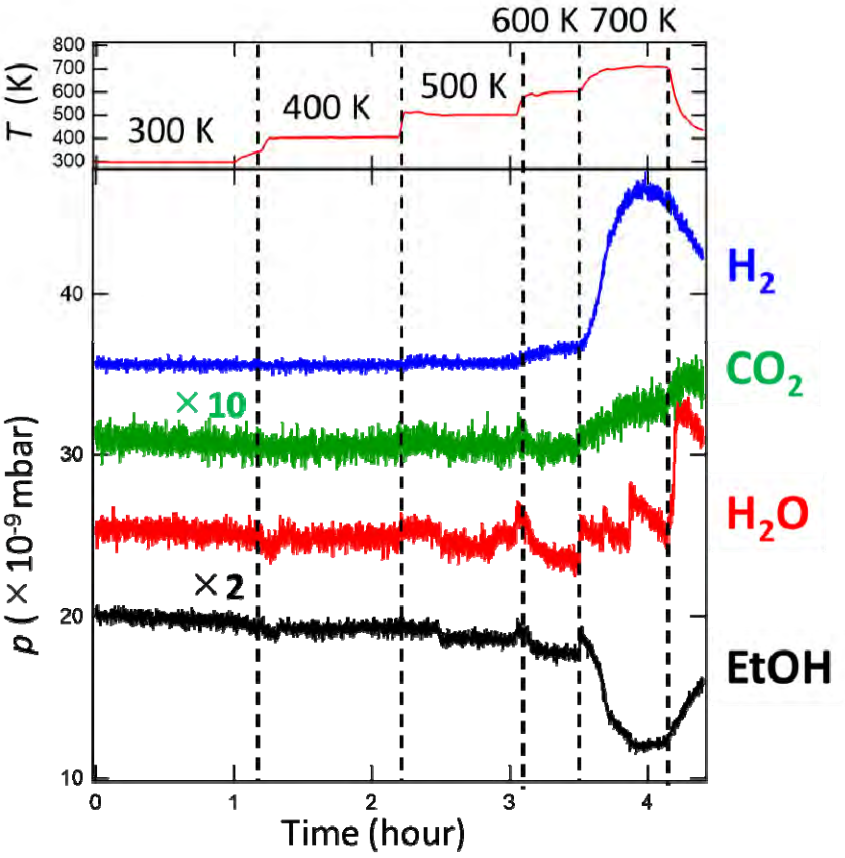

Figure 1. Catalytic activity measurements of Ni(111) for an ESR reaction. Gas composition was monitored with mass spectrometer, while the Ni catalyst was heated in a stepwise manner from 300 K to 400 K, 500 K, 600 K and 700 K in the mixed gas of 3 mbar EtOH and 9 mbar H_2O.

REFERENCES

[1] T. Koitaya, S. Yamamoto *et al.*, *Topics in Catalysis* **59**, 526-531 (2016).

[2] T. Koitaya, S. Yamamoto *et al.*, *e-J. Surf. Sci. Nanotechnol.* **17**, 169-178 (2019).

[3] S. Yamamoto *et al.*, *Synchrotron Radiat. News*, in press (2022).

[4] S. Yamamoto *et al.*, *Journal of the Japanese Society for Synchrotron Radiation Research* **35**, 182-190 (2022). (in Japanese)

DEVELOPMENT OF SOFT X-RAY MICROSCOPY SYSTEM WITH CYLINDRICAL-SHAPE WOLTER MIRROR

Takashi KIMURA,[1] Yoko TAKEO,[1,2] Kai SAKURAI,[3] Noboru FURUYA,[3]
Satoru EGAWA,[4] Gota YAMAGUCHI,[5] Yusuke MATSUZAWA,[6] Takehiro KUME,[6]
Hidekazu MIMURA,[7] Mari SHIMURA,[8] Haruhiko OHASHI,[2,5]
Iwao MATSUDA,[1] and Yoshihisa HARADA[1]

[1]*The Institute for Solid State Physics, The University of Tokyo*

[2]*Japan Synchrotron Radiation Research Institute*

[3]*Department of Applied Physics, School of Engineering, The University of Tokyo*

[4]*RIKEN Center for Advanced Photonics*

[5]*RIKEN, SPring-8 Center, 1-1-1*

[6]*Technology Center, Natsume Optical Corporation*

[7]*Department of Precision Engineering, School of Engineering, The University of Tokyo*

[8]*Research Institute, National Center for Global Health and Medicine*

X-ray microscopy has a wide range of applications in science due to its high spatial resolution and variety of analytical techniques. Ptychography provides a particularly high spatial resolution by reconstructing the sample image using phase recovery calculations[1, 2]. The combination of ptychography and spectroscopy in the soft X-ray region is promising for investigating samples with light-element-rich heterogeneous structures. For example, in the combination of soft X-ray ptychography with X-ray absorption spectroscopy, mapping the chemical state of magnetic nanoparticles in bacteria[3] and the visualization of the cathode degradation mechanism of the lithium-ion batteries[4] have been demonstrated.

For ptychography at multiple X-ray wavelengths, total reflection mirror optics have the optimal character of achromatic aberration and high focusing efficiency. The current achievable focusing size of total reflection mirrors in soft X-rays is around a few hundred nanometers[5], much larger than that of zone plates. However, the spatial resolution obtained in ptychography is independent of the focusing beam size, which makes the total reflection mirrors a potential candidate. In addition, the long working distance of the mirror optics also makes it suitable for applications in tomographic and in-situ/operand measurements.

In this work, we developed a new total-reflection Wolter mirror optics for soft X-ray ptychography and demonstrated that it can be used to measure cellular samples[6]. The total-reflection Wolter mirror was fabricated by modifying our previous precision electroforming process. The reflecting surface of the Wolter mirror, which was covered with Au, enables seamless ptychographic measurements in a wide energy range of soft X-rays. Figure 1 shows the schematic illustration of the system

A soft X-ray ptychographic system with a total-reflection Wolter mirror achieved a resolution of approximately 50 nm in a test chart evaluation. We have also shown that it is possible to visualize the microstructure of a mammalian cell over a wide photon energy range without chromatic aberration. Figure 2 shows the retrieved image of the mammalian cell from 250 eV to 1.2 keV. Furthermore, taking advantage of the long working distance of the optical system, stereo imaging with a large rotation angle was also attempted to measure the cell sample. Ptychographic imaging with a pink beam from the undulator was also possible. The soft X-ray typography system based on the Wolter mirror optics developed in this study is expected to be highly effective for investigating thick samples with complex three-dimensional structures and chemical compositions.

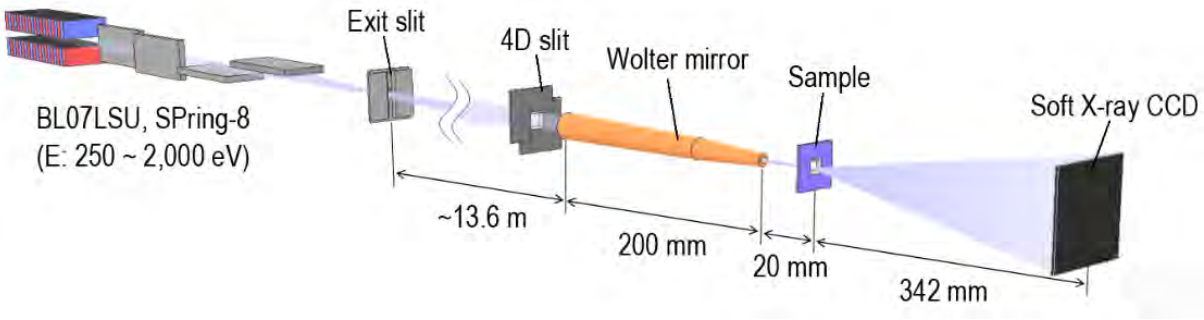

Figure 1. Schematic illustration for the soft X-ray ptychography system at BL07LSU of SPring-8.

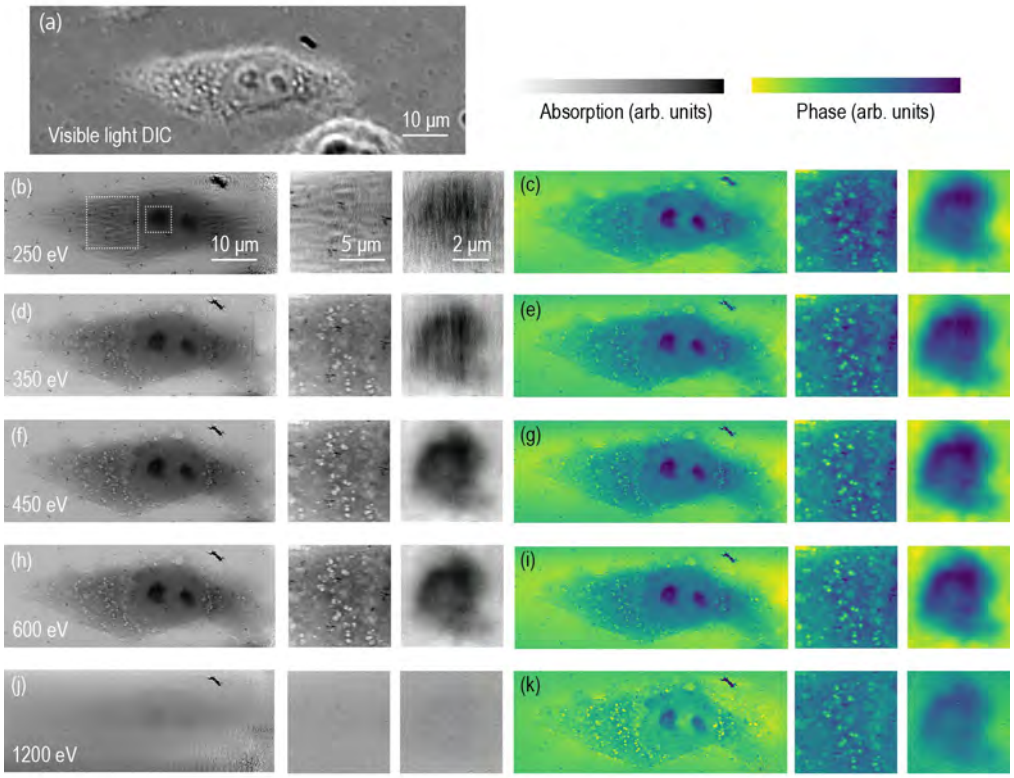

Figure 2. Soft X-ray ptychography measurement of a mammalian cell. (a) Visible light differential interference contrast image. (b-k) Reconstructed absorption (b,d,f,h,j) and phase (c,e,g,i,k) images at 250 eV, 350 eV, 450 eV, 600 eV, and 1200 eV. The magnified images to the right of the main images are taken from areas corresponding to the dotted rectangles shown in (b).

REFERENCES

[1] A. M. Maiden, J. M. Rodenburg, Ultramicroscopy, 109 (10), 1256 (2009).
[2] P. Thibault, et al., Science, 321, 379 (2008).
[3] X. Zhu, et al. Proc. Natl. Acad. Sci. , 113 (51) E8219 (2016).
[4] T. Sun, et al., ACS Nano, 15, 1475 (2021).
[5] Y. Takeo, et al., Appl. Phys. Lett. 117, 151104 (2020)
[6] T. Kimura, et al., Opt. Express, accepted.

A NOVEL MEASUREMENT METHOD OF NEAR-EDGE X-RAY ABSORPTION FINE STRUCTURE USING CONTNIOUS ROTATION OF LINEAR POLARIZATION ANGLES

Masafumi HORIO[1], Yoshiki KUDO[1], Yasuyuki HIRATA[2], Masahito NIIBE[3], Masato KOTSUGI[4], Iwao MATSUDA[1]

[1]*The Institute for Solid State Physics, The University of Tokyo*

[2]*Department of Applied Physics, National Defence Academy*

[3]*Laboratory of Advanced Science and Technology for industry, University of Hyogo*

[4]*Department of Materials Science and Technology, Tokyo University of Science*

Near-edge X-ray absorption fine structure (NEXAFS) is one of the X-ray spectroscopy methods employed to analyze the electronic state [1]. In recent years, NEXAFS measurements have evolved into nano-spatial imaging and *openrando* experiments, allowing, for example, to identify orbital types and determine molecular configurations by use of linear polarization. In such measurements, NEXAFS spectra are acquired by changing the angle between the molecule and the linear polarization. Typically, at a synchrotron radiation facility, the linear polarization of the beam is fixed, and a series of angle-resolved data is collected while the sample is rotated. This experimental method is simple, but at the same time, it limits the conditions of the sample environment. For example, the sample must be uniform to cover the misalignment between the beam spot and the sample rotation axis. On the other hand, in the case of nano-beam NEXAFS and *operando* experiments, it is technically difficult to ensure the exact beam position after sample rotation on a non-uniform and complex nanodevice. Therefore, it is now required to rotate the linear polarization of the X-ray beam instead of rotating the sample. In the present research, we designed a novel control method of linear polarization angles by the segmented undulator of SPring-8 BL07LSU.

The light source of SPring-8 BL07LSU consists of an 8-segment insertion device (ID) and a 7-segment phase shifter (PS), as shown in Fig. 1 [2]. The ID segments are either horizontal or vertical figure-8 undulators. The horizontal (H) and vertical (V) ID segments are alternately placed between the PS, which is used to adjust the relative phase of the radiation. To achieve linear polarization at arbitrary angles, two waves of left and right circular polarization produced by sets A and B of ID segments were combined, as shown in Fig. 1 (b). Set A consists of H1, V2, H3, and V4 segments, while set B is assembled with H5, V6, H7, and V8 segments. If set A generates right (left) circular polarization, set B generates left (right) circular polarization. The rotation angle θ of the linearly polarized light could then be controlled by changing the phase difference between the left and right circular polarizations with PS #4. As a demonstration of NEXAFS using this new polarization control, experiments were performed in the ultrahigh vacuum chamber of the SPring-8 BL07LSU. Hexagonal boron nitride (h-BN) films were prepared as samples. h-BN microcrystals have a flat shape, and the films were found to be oriented in two dimensions when mechanically pressurized. NEXAFS spectra were recorded by total electron yield at room temperature.

Figure 2(a) shows a collection of N K-edge NEXAFS spectra of oriented h-BN films, measured at the incident angle of 80° with linearly polarized light in the horizontal and vertical direction. The horizontal direction and the rotation axis of the sample were set perpendicular to each other. As shown in the figure, two prominent peaks were found at $h\nu =$ 401.5 and 408.0 eV corresponding to π^* and σ^* orbitals of h-BN. In the horizontal polarization experiment, the intensity of the π^* peak is found to be larger while the σ^* peak is enhanced by vertical polarization. This spectral behavior is explained in terms of a dipole

transition in optical absorption. Since the π^* (σ^*) orbitals are oriented out-of-plane (in-plane), the peak intensity is enhanced when the linearly polarized light is parallel to the out-of-plane (in-plane) direction.

We focus on the π^* and σ^* peaks and track their intensity changes with the angle of linear polarization θ [Fig. 2(b)] Since this NEXAFS technique differs from the conventional one, it is hereafter referred to as a rotational NEXAFS measurement. The intensity at $h\nu = 401.5$ eV (π^*, plotted in green) is maximum at $\theta = 0$, π, 2π (horizontal) and minimum at $\theta = \pi/2$, $3\pi/2$ (vertical) while at $h\nu = 408.0$ eV (σ^*, plotted in yellow) the opposite trend is seen. This result is consistent with the conventional NEXAFS results shown in Fig. 2(a). However, the rotational NEXAFS data contain angle-dependent data, which increases the reliability of the experiment and thus allows more precise determination of orbital configuration. In future, this technique could be combined with nano-focusing and/or fast polarization switching by electromagnetic PSs. This will allow quick and sensitive detection of NEXAFS signals from non-uniform functional materials and enhance the potential of NEXAFS in modern science.

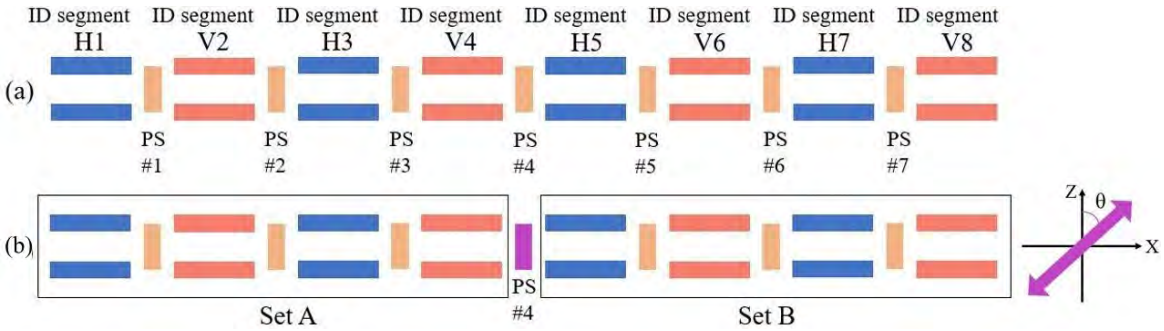

Fig. 1: Segmented cross undulator. (a) The light source composed of eight segments of the insertion device (ID) and seven phase shifters (PS's). Horizontal (H) and vertical (V) IDs are positioned alternately. (b) The setup for producing linear polarization at arbitrary azimuthal angles. Circularly polarized light with opposite helicities is produced by undulator sets A and B, and interfere with a relative phase difference controlled by PS #4.

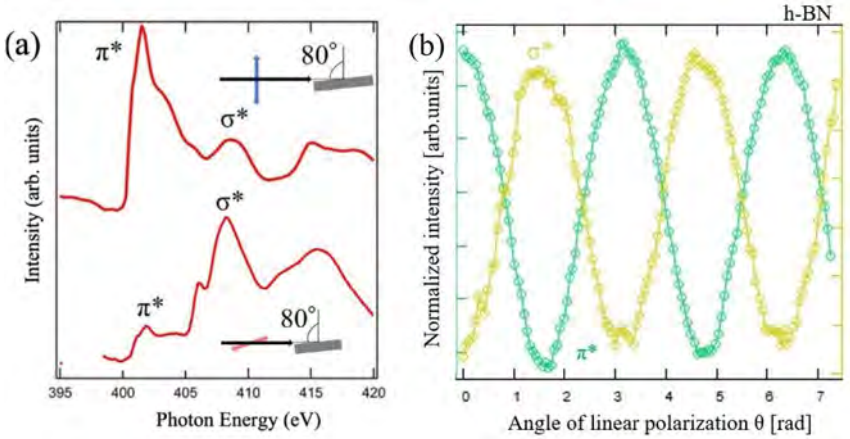

Fig. 2: NEXAFS spectra of h-BN recorded with a grazing incidence of 80°. (a) NEXAS measured by using the horizontal (top) and vertical (bottom) polarization. (a) Absorption intensity of the selected transition as indicated, plotted versus linear-polarization angle.

REFERENCES

[1] J. Stöhr, NEXAFS Spectroscopy (Springer, Berlin, Heidelberg, 1992).
[2] S. Yamamoto *et al*., J. Synchrotron Rad. **21**, 352 (2014).

Coherence Effect of Intermediate State in Resonant Inelastic Soft X-ray Diffraction

J. Miyawaki[1,3], T. Yachi[2], S. Maki[2], K. Kanie[2] and Y. Harada[3]

[1]*Institute for Advanced Synchrotron Light Source, National Institutes for Quantum and Radiological Science and Technology*
[2]*Institute of Multidisciplinary Research for Advanced Materials, Tohoku University*
[3]*Institute for Solid State Physics, The University of Tokyo*

The fundamental determinants of the physical properties of materials (external field response) are elementary excitations such as phonons, magnons, and crystal field excitations. These elementary excitations are very sensitive to structural changes in materials, suggesting the importance to identify both the structure and these excitations simultaneously. Resonant inelastic X-ray scattering (RIXS) is the most direct method to observe these elementary excitations. Since elastic scattering contains information related to diffraction, RIXS also contains diffraction-derived structural information. Therefore, RIXS originally has the potential to correlate the structural information with the electronic state, i.e., to observe the electronic state in a structure-selective manner.

We have been conducting angle-resolved RIXS experiments with several Fe-containing nanoparticles to demonstrate the diffraction-assisted enhancement of the RIXS intensity using small angle X-ray scattering (SAXS), which is caused by diffraction phenomena from nanoparticles. The combined method of RIXS and SAXS is the inelastic version of SAXS and can be called small angle inelastic X-ray scattering (SAIXS). SAXS and SAIXS were measured at the Fe *L*-edge for two types of nanoparticles, Fe_3O_4 (insulator) and FePt (metal), and the angle dependence of the elastic scattering was clearly observed for both types of nanoparticles: SAXS in the soft X-ray region was successfully observed. On the other hand, we have reported that SAIXS was observed in FePt, but not in Fe_3O_4; the observation of SAIXS in FePt demonstrated that diffraction-assisted inelastic scattering can be realized when the conditions are met, but the results that SAIXS was not observed in Fe_3O_4 nanoparticle were not fully interpreted.

In order for angular (momentum) dependence of RIXS to be observed, the absorption and core-hole decay processes must be undisturbed by other relaxation effects such as electron-electron and electron-phonon interactions, and temporally coherent so that they can be regarded as RIXS processes. In addition, for the core-hole of the final state to be momentum-dependent, it must be delocalized so that it has well-defined crystal momentum in the crystal. This corresponds to spatial coherence, and both temporal and spatial coherence are considered to be necessary for SAIXS to be observed [1]. In this study, SAIXS was measured at near the threshold of the absorption edge, where the temporal coherence was enhanced [2], and the effects of temporal and spatial coherence were investigated.

Fig. 1(a) shows the SAXS results of Fe_3O_4 nanoparticles. The average particle size of the nanoparticles was 5.9 nm, and the incident energy was set to 707.5 eV, which was the threshold of the L_3 absorption edge. Linear vertical polarization was used to focus on the intensity of the elastic scattering. The SAXS profile obtained was slightly ambiguous than when measured at the top of the L_3 peak because of the weak resonance effect at the threshold of the absorption edge, but the similar SAXS profile were obtained. The profile was good agreement with the simulation, suggesting that the SAXS profiles were successfully observed. Next, RIXS measurements were performed at the same diffraction condition as SAXS, using linear horizontal polarization to focus on inelastic scattering. The SAIXS profile which was obtained by integrating the intensity of the inelastic component in RIXS spectra from ~1 to

~8 eV is shown in Fig. 1(b) together with the SAXS profile. No clear SAIXS profile was observed at the threshold of XAS, as was the case for measurements at the L_3 peak top.

Since the incident energy in this experiment was set at the threshold of the absorption edge, we believe that temporal coherence is >50%, which is sufficiently high to observe SAIXS. Therefore, it is difficult to conclude that SAIXS was not observed due to the influence of temporal coherence. On the other hand, as for spatial coherence, since Fe_3O_4 is the insulator and valence orbitals are well localized, the observed inelastic components such as *dd* and charge-transfer excitations are mainly due to relaxation from the localized orbitals. Thus, the lack of SAIXS observed in Fe_3O_4 nanoparticles would be attributed to the lack of spatial coherence rather than temporal coherence. These results are consistent with the results of SAIXS observed for the metal FePt, in which the valence state is well delocalized in the crystal and the spatial coherence is high enough for SAIXS.

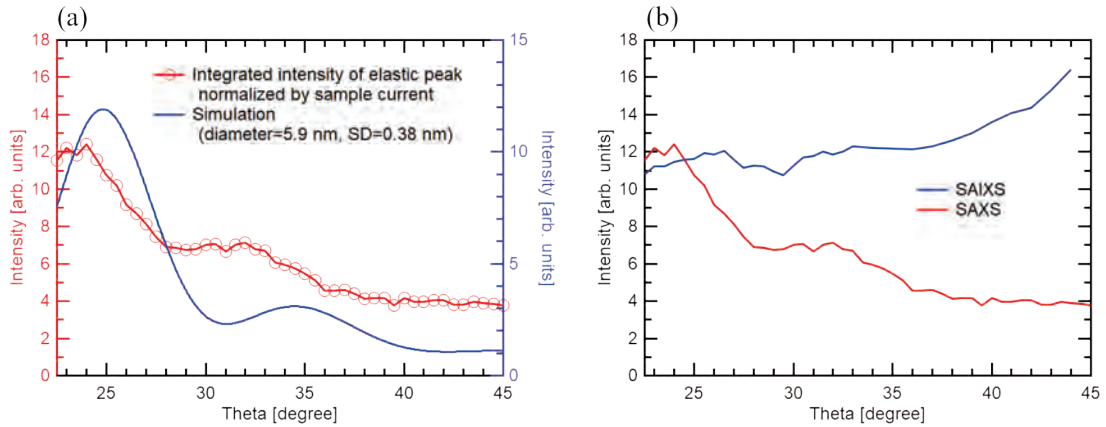

Fig. 1 SAXS and SAIXS of Fe_3O_4 nanoparticle measured at $h\nu$=707.5 eV. (a) Experimental (red) and simulated (blue) SAXS profile measured by σ polarization. (b) SAIXS spectra (blue) measured by π polarization compared with SAXS profile (red).

REFERENCES

[1] Y. Ma, Phys. Rev. B **49**, 5799 (1994).
[2] L. Zhang *et al.*, Fuller. Nanotub. Carbon Nanostructures **23**, 471 (2014).

ANALYSIS OF ELECTRONIC STATES OF PARTICULATE PHOTOCATALYSTS BY 3D NANO-ESCA

Takashi HISATOMI,[1,2] Naoka NAGAMURA,[2,3,4] Wenxiong ZHANG,[5] Kenta OHISHI,[2,3,4] Asako YOSHINARI,[3,4] Shingo TAKEZAWA,[3,4] Masaharu OSHIMA,[5] Yoshihisa HARADA[5]

[1]*Research Initiative for Supra-Materials, Shinshu University*

[2]*Precursory Research for Embryonic Science and Technology, Japan Science and Technology Agency*

[3] *Research Center for Advanced Measurement and Characterization National Institute for Materials Science*

[4]*Department of Materials Science and Technology, Tokyo University of Science*

[5]*The Institute for Solid State Physics, The University of Tokyo*

The water splitting reaction using particulate semiconductor photocatalysts is studied as a means of renewable solar hydrogen production on a large scale. $BaTaO_2N$ is an oxynitride photocatalyst material having a band gap energy of 1.9 eV and band edge potentials suitable for both hydrogen and oxygen evolution from water [1,2]. The photocatalytic activity of this material is dependent strongly on the preparation methods. In many cases, the activity for the hydrogen evolution reaction utilizing excited electrons is low. This is probably because $BaTaO_2N$ is an n-type semiconductor and has a large Schottky-type barrier that prevents the transfer of excited electrons at the interface with cocatalyst nanoparticles serving as an active site. In fact, it is known that doping Al^{3+} into the Ti^{4+} site of the $SrTiO_3$ photocatalyst to cancel the n-type semiconducting properties drastically improves the photocatalytic water splitting activity [3]. These facts suggests that there is a certain correlation between the semiconducting characters such as the Fermi level and the hydrogen evolution activity of semiconductor photocatalysts.

In this work, the electronic states of $BaTaO_2N$ and $SrTiO_3$ photocatalysts were analysed by three-dimensional nano-electron spectroscopy for chemical analysis (3D-nano ESCA). With high spatial resolution reaching less than 100 nm, it is expected that the valence band spectrum of individual photocatalyst particles without signals originating from the conductive sample stage can be obtained [4]. This will allow us to determine the Fermi level of particulate photocatalyst materials and the investigate the correlation between the Fermi level and photocatalytic activity.

Two kinds of $BaTaO_2N$ and $SrTiO_3$ were prepared according to literature. $BaTaO_2N$ nitrided from $BaCO_3$ and Ta_2O_5 in the presence of RbCl flux, denoted as $BaTaO_2N$ (RbCl), showed high hydrogen evolution activity [1]. The other $BaTaO_2N$ nitrided from nominally $Na_{1/4}Ba_{3/4}Zn_{1/4}Ta_{3/4}O_3$ and $BaCO_3$ in the presence of NaCl flux, denoted as $BaTaO_2N$ (NBZTO), showed high oxygen evolution activity [2]. Commercial $SrTiO_3$ as received, denoted as $SrTiO_3$, was hardly active in overall water splitting, while $SrTiO_3$ doped with Al in the presence of $SrCl_2$ flux, denoted as $SrTiO_3$:Al, was highly active in overall water splitting and showed an external quantum efficiency exceeding 90% in the near ultraviolet region [3]. These particulate photocatalysts had particle sizes of 200–500 nm and were immobilized on Au thin film by using the particle transfer method [5]. Figure 1 shows a scanning electron microscope image of a representative $BaTaO_2N$ sample embedded on Au film.

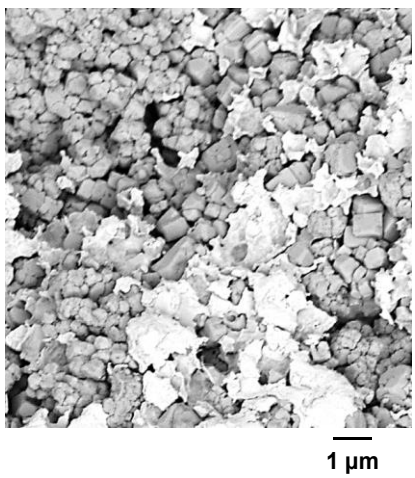

Figure 1. A scanning electron microscope image of $BaTaO_2N$ (NBZTO) embedded on Au film.

The core level and valence band X-ray photoelectron spectroscopy (XPS) data were acquired using the 3D-nanoESCA at BL07LSU of SPring-8. The incident

photon energy was set to 1200 eV. The spectral data were acquired with energy and spatial resolutions of 100 meV and 200 nm, respectively.

It was possible to acquire a valence band spectrum of a particulate photocatalyst free from the signal of the underlying Au thin film by choosing the measurement spot carefully (Figure 2Ab). However, at almost all measurement points, the signal of Au 5*d* orbitals derived from Au fragments exposed from the gap among photocatalyst particles overlapped in the valence band region (Figure 2Aa), and spectra that could be used for the determination of the Fermi level was not obtained in a reasonable time. Therefore, the Fermi level shift was estimated from the change in the binding energy of core levels.

Figures 2B and 2C show Ta 4*f* and Ba 3*d* spectra of the $BaTaO_2N$ materials, respectively. $BaTaO_2N$ (RbCl) had binding energies smaller than $BaTaO_2N$ (NBZTO) by 0.2 eV. The binding energy reflects the energy gap between the Fermi level and the core level. Given that the binding energy shift was attributable solely to the Fermi level shift, $BaTaO_2N$ (RbCl) should have a Fermi level at a 0.2 eV more positive potential than $BaTaO_2N$ (NBZTO). As a result, $BaTaO_2N$ (RbCl) was closer to the intrinsic semiconductor and had a weaker Schottky-type barrier at the interface with the cocatalyst. This may account for the higher hydrogen evolution activity of $BaTaO_2N$ (RbCl). However, the energy shift was relatively small. More comprehensive analysis of the materials properties will be needed to make a decisive conclusion. On the other hand, $SrTiO_3$:Al had binding energies smaller than $SrTiO_3$ by 0.4 eV for both Sr 3*d* and Ti 2*p* orbitals and thus was closer to the intrinsic semiconductor. This clear Fermi level shift confirms the corelation of the semiconducting properties and water splitting activity of the $SrTiO_3$ photocatalyst.

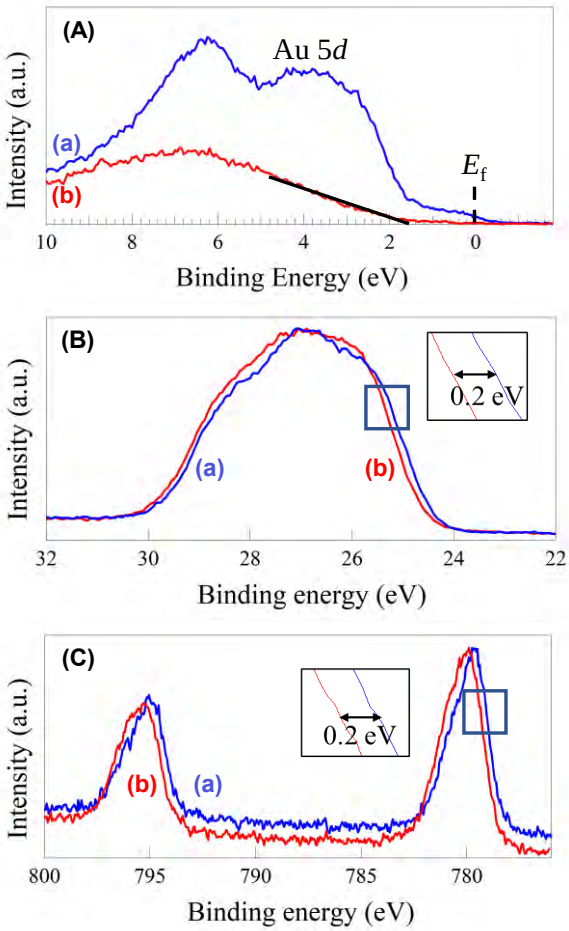

Figure 2. (A) Valence band, (B) Ta 4*f*, and (C) Ba 3*d* spectra of (a) $BaTaO_2N$ (RbCl) and (b) $BaTaO_2N$ (NBZTO). The valence band spectrum of $BaTaO_2N$ (RbCl) was overwhelmed by the signal from Au fragments.

In summary, the Fermi level shift could be estimated from the core level shifts, although measurement results that took advantage of the high spatial resolution were not obtained. Considering that the observed signal is given by the weighted average of the signals from the particulate sample and Au, it may be possible to extract the signal of the sample by statistical analysis of a large number of spectra.

REFERENCES

[1] Wang *et al. Nat. Commun.* **2021**, *12*, 1005.
[2] Jadhav *et al. J. Mater. Chem. A* **2020**, *8*, 1127.
[3] Takata *et al. Nature* **2020**, *581*, 411.
[4] Sakai *et al.*, *Nanoscale* **2016**, *8*, 18893.
[5] Minegishi *et al. Chem. Sci.* **2013**, *4*, 1120.

SPECTRAL IMAGING ANALYSIS OF EDGE-CONTROLLED 2D MATERIALS

Naoka NAGAMURA[1,2,3], Mitsuhiro OKADA[4], Ryo NOUCHI[3,5], Tarojiro MATSUMURA[4], Yasunobu ANDO[4], Asako YOSHINARI[1,2], Shingo TAKEZAWA[1,2], Kenta OHISHI[1,2,3], Kentaro FUKU[6], Wenxiong ZHANG[7], and Masaharu OSHIMA[7]

[1]*National Institute for Materials Science (NIMS), Tsukuba, Ibaraki, Japan.*
[2]*Tokyo University of Science, Katsushika, Tokyo, Japan*
[3]*PRESTO, Japan Science and Technology Agency, Honcho, Saitama, Japan.*
[4]*National Institute of Advanced Industrial Science and Technology (AIST), Tsukuba, Ibaraki, Japan*
[5]*Osaka Metropolitan University, Sakai, Osaka, Japan*
[6]*Tohoku University, Sendai, Miyagi, Japan*
[7]*The University of Tokyo, Kashiwa, Chiba, Japan*

In atomic layer semiconductor sheets, edge states are remarkably effective to the transport properties. Highly reactive dangling bonds exist at the edges of finite-size two-dimensional (2D) materials. Structures and chemical bonding states of the edges are easily modulated, so direct observation of edge states is important to discuss the characteristics of 2D materials. Here we have investigated the spatial distribution of electronic states and chemical bonding states of the edge-controlled functional 2D materials, the monolayer MoS_2–Nb-doped MoS_2 lateral homojunctions and the gate-controlled UV photo-oxidized graphene field effect transistors, using the 3D nano-ESCA[1] system at BL07LSU of SPring-8.

1. MoS_2–Nb-doped MoS_2 lateral homojunctions

Monolayer transition metal dichalcogenides (TMDs) are promising materials for various next-generation semiconductor devices. However, carrier doping techniques for TMDs have not been completely established yet. We synthesized monolayer MoS_2–Nb-doped MoS_2 lateral homojunctions using chemical vapor deposition (CVD).

To analyse the spatial elemental composition and the carrier distribution of MoS_2–MoS_2:Nb, we performed 3D nano-ESCA measurements. Peak fitting of X-ray photoemission spectroscopy (XPS) spectra was performed using the spectrum- adapted expectation-conditional maximization (ECM) algorithm[2,3].

The Mo 3*d* and S 2*s* core levels of the MoS_2:Nb region had smaller binding energies than those of the pure MoS_2 region (Δ ~0.3 eV) as shown in Fig. 1(a). This difference was attributed to the Fermi-level (E_F) downshift by hole doping[4]. Fig. 1(b) presents the intensity mapping of Nb^{4+} $3d_{5/2}$ core level peak in a MoS_2–MoS_2:Nb sheet. Signals from Nb^{4+} were observed only in the edge regions. Moreover, in the peak position mapping of Mo^{4+} $3d_{5/2}$ (Fig. 1(c)), low-binding energy shift were observed also only at the edge region. Therefore, the grown MoS_2–MoS_2:Nb is revealed to have a built-in *p*–*n* lateral homojunction[5].

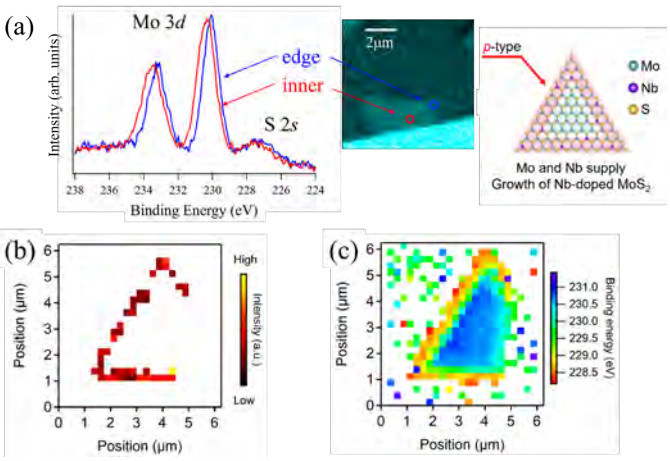

Figure 1 (a) Mo 3*d* and S 2*s* core level spectra measured at points indicated in the inserted image. Right picture is MoS_2–MoS_2:Nb growth strategy. (b) peak intensity mapping image of Nb^{4+} $3d_{5/2}$ and (c) peak position mapping image of Mo^{4+} $3d_{5/2}$ measured on MoS_2–MoS_2:Nb sheet.

2. Gate-controlled UV photo-oxidized graphene field effect transistor

Photo-oxidation is one of the means for surface modifications to control the electronic and chemical properties. Recently, the gate controllability of photo-oxidation reaction in graphene has been verified using a field-effect-transistor (FET) configuration[6,7]. However, the chemical structure of photo-oxidized graphene surface has not yet been experimentally measured. Then we performed an XPS analysis with a high spatial resolution using the 3D nano-ESCA.

Fig. 2(a) shows pin-point XPS spectra of C 1*s* taken at the edge region and the center region of the photo-oxidized graphene FET. The binding energy of the main peak at the edge is 0.12 eV lower than that at the center. This energy shift is considered to be caused by the Fermi-level (E_F) shift induced by charge doping[4]. The concentration of the doped holes in graphene at the edge is estimated to be 1.1×10^{12} cm^{-2}, which is consistent with the previous studies on thermal annealing[8].

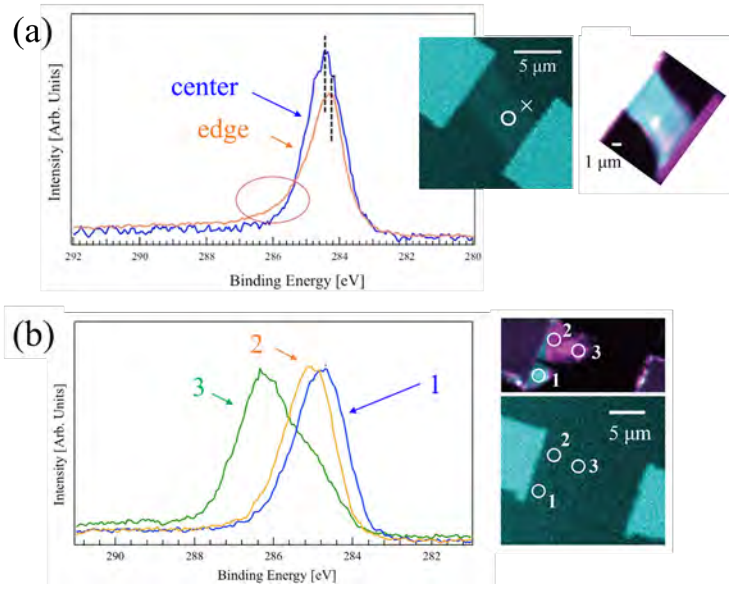

Figure 2 Pin-point C 1*s* and core level spectra measured at (a) the mildly photo-oxidized graphene FET and (b) the heavily photo-oxidized graphene FET.

As oxidation reactions progress, the shape of the spectrum changes. Fig. 2(b) shows pin-point XPS spectra of C 1*s* at several locations in the heavily photo-oxidized graphene FET. Peak components at higher binding energies, derived from sp^3 bonding and carbon-oxygen chemical bonding, seems to increase as oxidation progress.

Therefore, we revealed that the gate-controlled UV photo-oxidation reaction proceed as follows: hole doping via adsorbed molecules at the edge region → defect introduction by chemical reactions with adsorbed molecules → decomposition and disappearance[9].

REFERENCES

[1] K. Horiba, Y. Nakamura, N. Nagamura, S. Toyoda, H. Kumigashira, M. Oshima, K. Amemiya, Y. Senba, and H. Ohashi, *Rev. Sci. Instrum.* **82**, 113701 (2011).

[2] T. Matsumura, N. Nagamura, S. Akaho, K. Nagata, and Y. Ando, *Sci. Technol. Adv. Mater.* **20**, 733 (2019).

[3] T. Matsumura, N. Nagamura, S. Akaho, K. Nagata, and Y. Ando, *Sci. Technol. Adv. Mater.: Methods* **1**, 45 (2021).

[4] N. Nagamura, H. Fukidome, K. Nagashio, K. Horiba, T. Ide, K. Funakubo, K. Tashima, A. Toriumi, M. Suemitsu, K. Horn, and M. Oshima, *Carbon* **152**, 680 (2019).

[5] M. Okada, N. Nagamura, T. Matsumura, Y. Ando, A. Lu, N. Okada, W. Chang, T. Nakanishi, T. Shimizu, T. Kubo, T. Irisawa, and T. Yamada, *APL Mater.* **9**, 121115 (2021).

[6] N. Mitoma, and R. Nouchi, *Appl. Phys. Lett.* **103**, 201605 (2013).

[7] R. Nouchi, M. Matsumoto, and N. Mitoma, *J. Mater. Chem. C* **7**, 1904 (2019).

[8] S. Ryu, L. Liu, S. Berciaud, Y. Yu, H. Liu, P. Kim, G. W. Flynn, and L. E. Brus, *Nano Lett.* **10**, 4944 (2010).

[9] N. Nagamura, S. Konno, M. Matsumoto, W. Zhang, M. Kotsugi, M. Oshima and R. Nouchi, *in preparation.*

RIXS-MCD Study of Chromium Trihalides CrX_3 (X = Cl, Br, I)

C. S. Pathiraja, J. N. Ranhili, Y. C. Shao, Y. -D. Chyang, B. Freelon

In the recently discovered 2D magnets formed by chromium trihalides CrX_3 (X = Cl, Br, I), a rich interplay between stacking and interlayer exchange has eventually led to a range of applications in spintronics, heterostructures, and twisted-layer devices. However, one of the most important open questions in this new field is what is the nature of the magnetic anisotropic interactions? Magnetic circular dichroism (MCD) in Resonant Inelastic X-ray Scattering (RIXS-MCD) is well-suited to address this issue because the technique allows the determination of d-orbitals that are associated with magnetic (dichroic) signals. The purpose of this beamtime was to use high-resolution RIXS-MCD and determine the detailed excitations that are relevant for the magnetic interaction in the CrX_3. Magnetic dichroic effect was studied for each d-d excitation to track their evolution.

During the beamtime, the data were taken for three samples $CrCl_3$, $CrCl_{0.8}Br_{0.2}$ and CrI_3. Samples were aligned with the c- axis along antiparallel to the incident beam and the magnetic field was parallel to the incident beam. With the incident angle 45^0 at Room temperature, L-edge Cr RIXS-MCD were collected for both RCP and LCP at ~ 6 excitation energies with the incident wave vector directed along the direction of magnetization of the given 3 samples. Then the incident angle was changed to 90^0 and the measurements was repeated. Finally, the temperature was cooled down to liquid nitrogen temperature(~73.9K). At 74K, we could collect RIXS-MCD data only for $CrCl_3$ and $CrCl_{0.8}Br_{0.2}$ because the limited time.

The experiment was successful, and we could observe some dichroism in the materials under given circumstances. In $CrCl_3$, the dichroism could be observed in the XAS, and it was almost vanished in the RIXS-MCD spectra (Figure 1). For the mix halide RIXS-MCD spectra, lots of the loss features had no noticeable dichroic dependence; however, there was some small circular polarization difference d-d region of 576.5 eV spectrum. Moreover, 3-5 eV loss region was rich with some features. Even though there was not much dichroic dependence in that region, the spectral evolution was interesting. (Figure 2) When comparing the XAS spectra for different materials, there was a shift in the peak position for CrI_3 nearly around 576.1 eV (Figure 3). As a summary, dichroism could observe in the XAS spectra and for the RIXS-MCD as we expected and further data analysis is still on the process. In the upcoming future, we are planning to work with theorists and obtain a theoretical point of view for our experimental results.

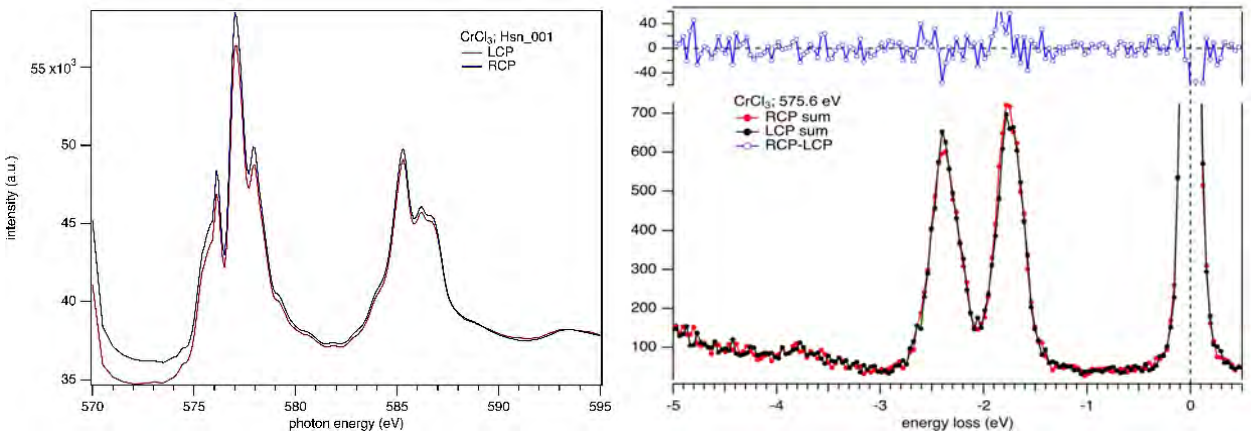

Figure 1: XAS and RIXS-MCD comparison of $CrCl_3$ for different excitation energies

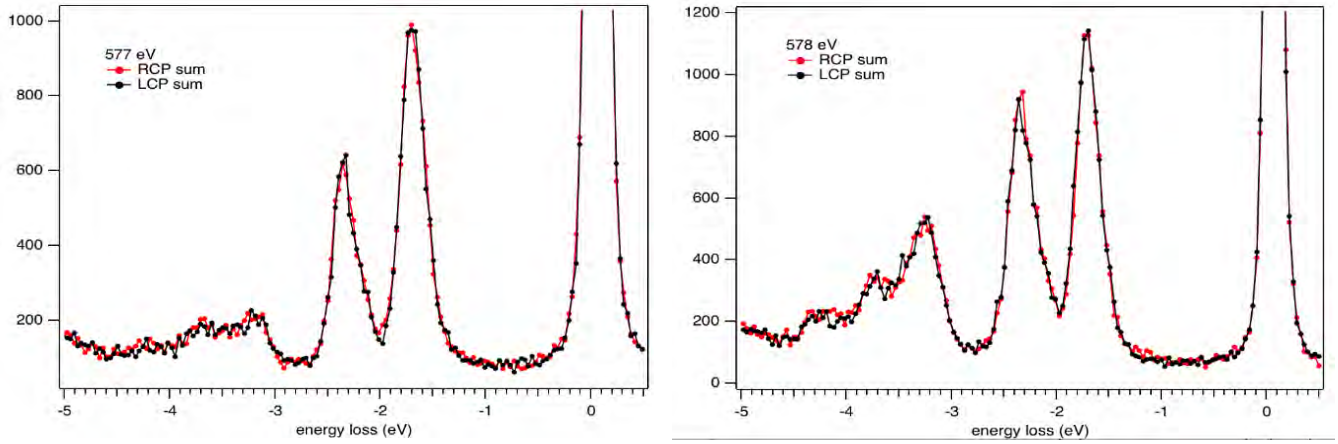

Figure 2: RIXS-MCD comparison of mix halide for different excitation energies

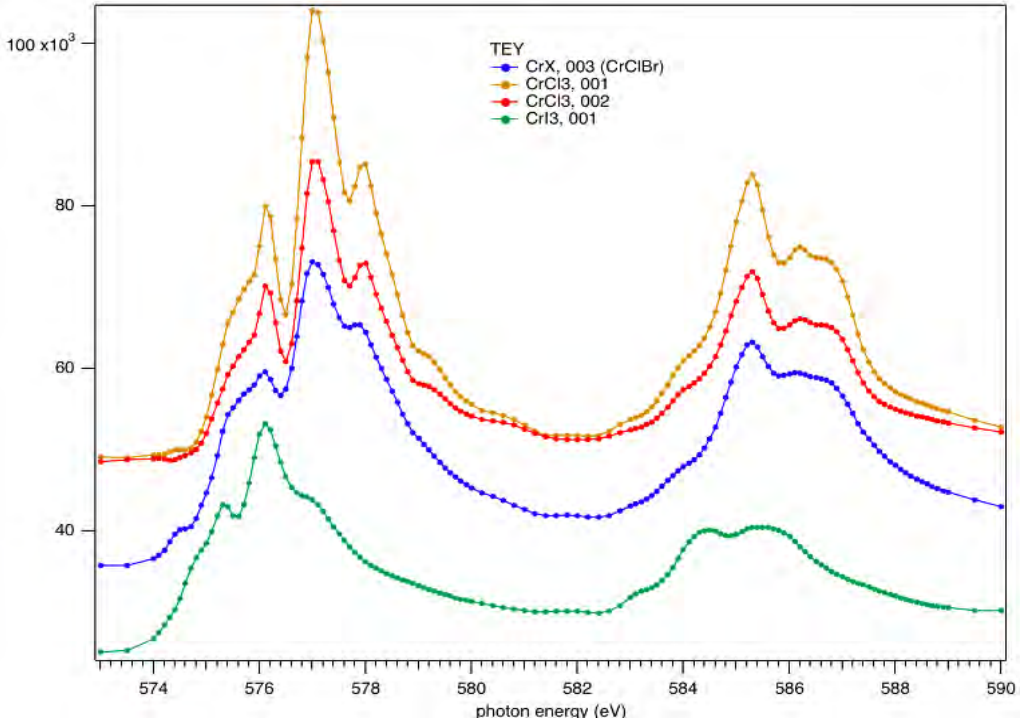

Figure 3: XAS comparison of different materials

INVESTIGATION OF ELECTRONIC STRUCTURE OF FE-CO SPINELS BY 2P3D RIXS AND L-EDGE XAS

Olaf Rüdiger,[1] Minmin Chen,[1] Derek Rice,[1] Hisao Kiuchi[2], Wenxiong Zhang[2], Ralph J. Ugalino[3], Naoya Kurahashi[2], Yoshihisa Harada[2,3], Serena DeBeer[1]

1. Max Planck Institute for Chemical Energy Conversion, Mülheim an der Ruhr, Germany

2. Synchrotron Radiation Laboratory, The Institute for Solid State Physics, The University of Tokyo

3. Graduate School of Frontier Sciences, The University of Tokyo

We collected cobalt $L_{2,3}$ X-ray absorption spectra and 2p3d RIXS spectra of a series of Fe-loaded Co-based spinels relevant for water and alcohol oxidation reactions.[1] Fe loading in a Co spinel is known to induce spinel inversion, but the degree of inversion cannot be easily obtained by XRD. Spinels have a general formula $A^{2+}B^{3+}{}_2O_4$, with *A* occupying a tetrahedral site (T_d) and *B* an octahedral one (O_h). For an inverse spinel, the +3 ions are equally distributed among the T_d and O_h sites, while the +2 ion sits at a O_h site. In order to obtain the spectral signatures of the different sites, we collected spectra from the inverse spinel $CoFe_2O_4$, containing only $Co^{2+}{}_{Oh}$, and from the spinels $CoAl_2O_4$ (containing only $Co^{2+}{}_{Td}$), and $ZnCo_2O_4$ ($Co^{3+}{}_{Oh}$).

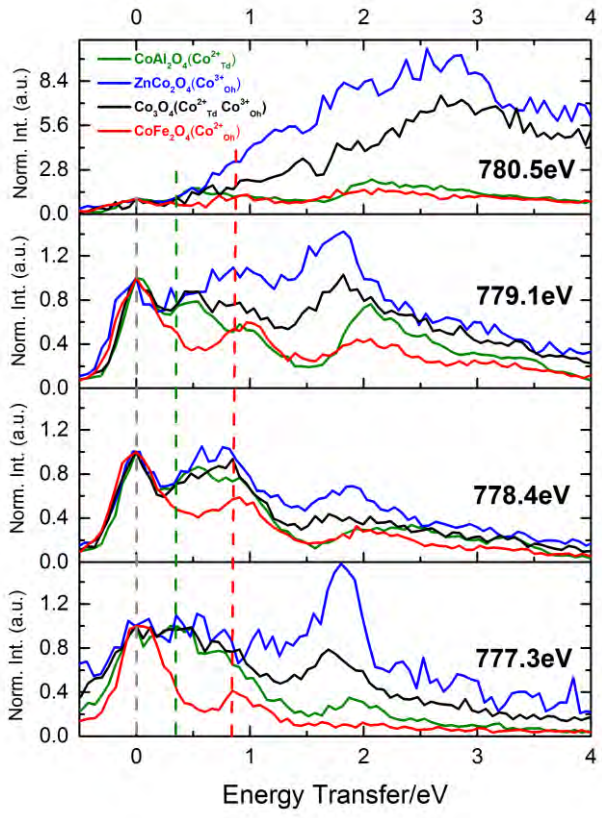

Figure 1. 2p3dRIXS of (a) $CoAl_2O_4$, (b) $ZnCo_2O_4$, (c) Co_3O_4, and (d) $CoFe_2O_4$ at incident energy 777.3eV, 778.4eV, 779.1eV, and 780.5eV respectively.

Figure 1 shows the 2p3d RIXS spectra of Al_2CoO_4, Co_2ZnO_4, Co_3O_4, and $CoFe_2O_4$.The spectra show significant differences that can be assigned to the distinct spinel sites (Figure 1). At low incident energy we are primarily exciting the Co^{2+} ions, and we can clearly observe the differences between the T_d and O_h sites comparing the Al_2CoO_4 and $CoFe_2O_4$ samples, where the former has an emission signature at very low energy loss (0.5 eV). In contrast, the $ZnCo_2O_4$ sample has a transition at 0.7 eV, while the first inelastic peak for the inverse spinel appears at slightly higher energy.

To fully understand the different transitions, we are currently running multiplet calculations within the ORCA code.[2] In Figure 2, we show preliminary calculations for the CoO and $CoAl_2O_4$ samples. The best fit to the spectra gave a 10 Dq value of 0.97 eV in a O_h geometry and a reduction of the atomic Slater-Condom parameters by 65% to account for covalency. For the T_d geometry we obtained a 10 Dq value of 0.52 eV and a reduction of the atomic Slater-Condom parameters of 70% for F_k and 63% for G_k have been used to reproduce $CoAl_2O_4$ spectra, although we found an inconsistency for the spectra at 779.1eV that we are still trying to refine. Similar calculations are being carried on for the $Co^{3+}{}_{Oh}$ using the measured Co_2ZnO_4 as references.

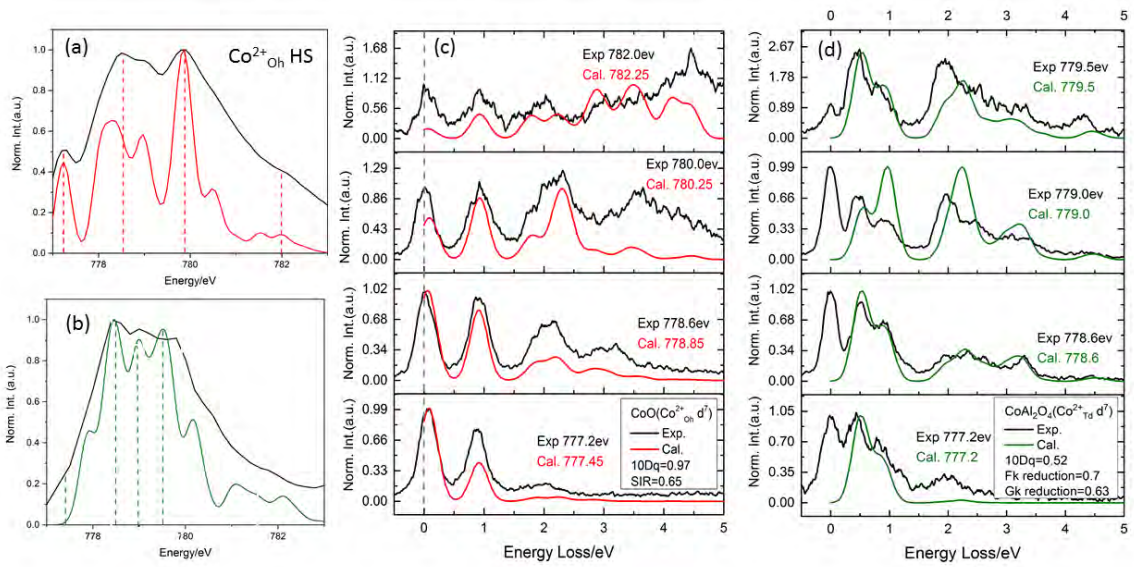

Figure 2. (a) L_3-edge XAS calculation of $Co^{2+}{}_{Oh}$ and (b) $Co^{2+}{}_{Td}$ used the same parameter as their 2p3d RIXS calculation. (c) 2p3d RIXS calculation of $Co^{2+}{}_{Oh}$ and (d) $Co^{2+}{}_{Td}$ at incident energy 777.3eV, 778.4eV, 779.1eV, and 780.5eV with ORCA-LFT.

Figure 3 shows the 2p3d RIXS spectra of a series of Co-spinels with increasing amounts of Fe-loading at an incident excitation energy of 779.1 eV. The first conclusion that can be extracted is that the intensity at 0.5 eV, as well as the position of the peak between 0.6 and 1 eV energy transfer, appears to correlate with the degree of spinel inversion. This way we can easily assign the Co_2FeO_4 as a spinel, while the $Co_{1.5}Fe_{1.5}O_4$ resembles much more the inverse spinel. Another interesting conclusion is that the position of the peaks for the Co_2FeO_4 is shifted with respect to the pure Co_3O_4 spinel. This is indicative of a modulation of the crystal field parameters of the Co ions by Fe substitution. Fe loading is known to improve the catalytic properties of Co spinel for water oxidation.[1b] In the present work, we show evidence of how the Fe loading influences the Co electronic structure, as well as a technique to identify spinel inversion in these materials.

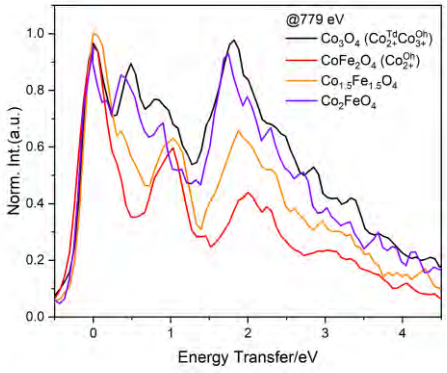

Figure 3. 2p3d RIXS spectra for a series of Fe-substituted Co spinels at 779.1 eV incident energy. The data has been smoothed by applying a 5-point moving average.

REFERENCES

[1] a) D. Waffel, E. Budiyanto, T. Porske, J. Büker, T. Falk, Q. Fu, S. Schmidt, H. Tüysüz, M. Muhler, B. Peng, *Molecular Catalysis* **2020**, *498*, 111251; b) E. Budiyanto, M. Q. Yu, M. M. Chen, S. DeBeer, O. Rudiger, H. Tuysuz, *Acs Applied Energy Materials* **2020**, *3*, 8583-8594.

[2] F. Neese, *Wiley Interdisciplinary Reviews: Computational Molecular Science* **2012**, *2*, 73-78.

STUDY ON THE ELECTRONIC STATE OF WATER MOLECULES IN POLYMER ELECTROLYTE MEMBRANES

Naoya Kurahashi[1], Ugalino Ralph John[2] and Yoshihisa Harada[1]

[1]*Synchrotron Radiation Laboratory, The Institute for Solid State Physics, The University of Tokyo*

[2]*Graduate School of Frontier Sciences, The University of Tokyo*

A fuel cell is a power generation device that directly converts chemical energy such as hydrogen into electrical energy. Fuel cells are highly energy efficient and do not generate carbon dioxide during power generation, so they are expected to contribute to the reduction of greenhouse gas emissions. In Japan, stationary fuel cells for home use were put on the market in 2009, and fuel cell vehicles were put on the market in 2014, but further spread and expansion are required. In particular, polymer electrolyte fuel cells (PEFCs) are being installed in automobiles because they are small and can generate electricity at low temperatures.

In PEFCs, when hydrogen gas is supplied to the anode, hydrogen ions (H^+) are generated on the electrodes. The generated hydrogen ions pass through the polymer electrolyte membrane (PEM) and move to the cathode, where hydrogen ions react with oxygen gas on the electrodes to generate energy and water molecules. Therefore, the polymer electrolyte membrane must have high gas barrier properties, water resistance, and mechanical strength, while allowing only hydrogen ions to permeate with high efficiency. Most of the polymers used in PEMs have a structure in which a strong acid group such as a sulfo group is introduced at the end of a hydrophobic skeleton. When these macromolecules aggregate, they take an inverted micelle structure and form nanometer-order channel structures[1]. When the PEM is humidified, water is taken into the channel and hydrogen ions are released from the superacid group, which is thought to be a conduction path for hydrogen ions[2]. Therefore, it is necessary to evaluate the hydrogen-bond property of water molecules in the PEM in order to understand the proton permeability. However, experimental research was lacking because it was difficult to directly observe the water molecules incorporated inside the membrane. The authors have previously attempted to evaluate the diffusion of water molecules incorporated into the Nafion membrane using nuclear magnetic resonance spectroscopy. As a result, it was clarified that the motility of water molecules changes significantly around a temperature of around 15 °C. The authors predicted that the cause of the change in motility was the change in the size of the proton channel, but we could not reach a conclusion only by NMR measurement. Therefore, we considered searching for the cause of the change in motility by investigating the electronic state of water molecules in the proton channel by soft X-ray emission spectroscopy. The sample was prepared by casting commercially available Nafion suspension onto a SiC plate and evaporate the solvent. By controlling both the temperature and humidity of the atmosphere control cell, the temperature dependence of the electronic state can be measured.

We evaluated the damage to Nafion because it was reported that soft X-rays would damage the fluorinated material. In the emission spectroscopy, the sample was moved at regular intervals to prevent damage to the SiC window and the sample, so that the same place is not continuously irradiated with synchrotron radiation. As a result of measuring the soft X-ray emission spectrum from Nafion by changing the X-ray irradiation time per point, it was concluded that damage to Nafion can be avoided if the X-ray irradiation is 5 seconds per point or less. Subsequently, the soft X-ray emission spectra from Nafion in a dry state with circulating nitrogen gas and in a humidified state at 80 % relative humidity were measured, and the difference spectrum between the two was calculated. As a result, only the emission spectrum derived from water molecules incorporated into the Nafion membrane could be extracted.

The soft X-ray emission spectra measured with photon energy of 550 eV and energy resolution of 150 meV is shown in Fig. 1. The spectra of water molecules confined in Nafion are quite different from that of bulk water measured under the same temperatures, with a largest peak that is thought to be $1b_1$" at all temperatures. This suggests that water molecules confined in Nafion and in the bulk form different hydrogen bonding networks. On the other hand, since the emission spectrum has four overlapping peaks, it was difficult to evaluate the temperature dependence of the spectra. Therefore, in order to quantitatively evaluate the temperature dependence, we performed a peak-fitting of the emission spectrum with four Gaussians and evaluate the temperature dependence of the fitting parameters. Fitting of the spectra was performed using the following function,

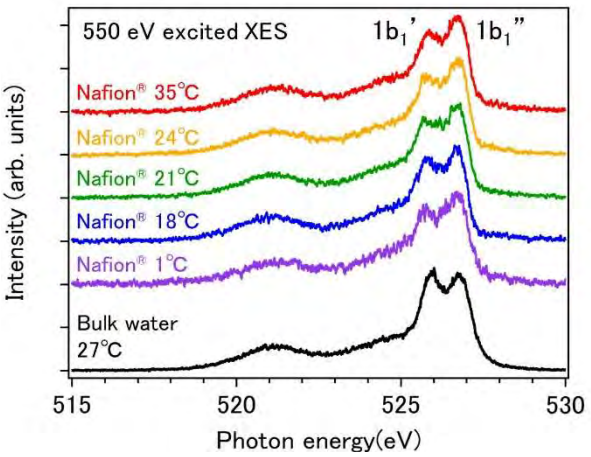

Fig. 1 Soft X-ray emission spectrum of bulk water and water molecules in Nafion at 80% relative humidity

$$I(x) = I_0 + \sum_i \frac{A_i}{\sqrt{2\pi\sigma_i^2}} e^{-\frac{(x-X_i)}{2\sigma_i}} \quad (i = 1b_2,\ 3a_1, 1b_1',\ 1b_1^{"}) \qquad (1)$$

where I_0, A_i, X_i, and σ_i are the baseline, peak area, peak position, and standard deviation of the peak, respectively. As a result, the peak area of $1b_1$' and $1b_1$" show an interesting temperature dependence (Fig. 2). The $1b_1$' emission intensity of water molecules confined into Nafion reached a maximum at 18 °C, while the $1b_1$" emission intensity reached a minimum at 18 °C. The $1b_1$' and $1b_1$" intensities of bulk water showed monotonic changes in the range from 1 to 50 °C. This suggests that the water molecules confined into Nafion reach a maximum rate of hydrogen bonding in tetrahedral coordination around 18 °C. Combined with the results of previous NMR studies, this suggests that the size of proton channels in Nafion may change around 18 °C.

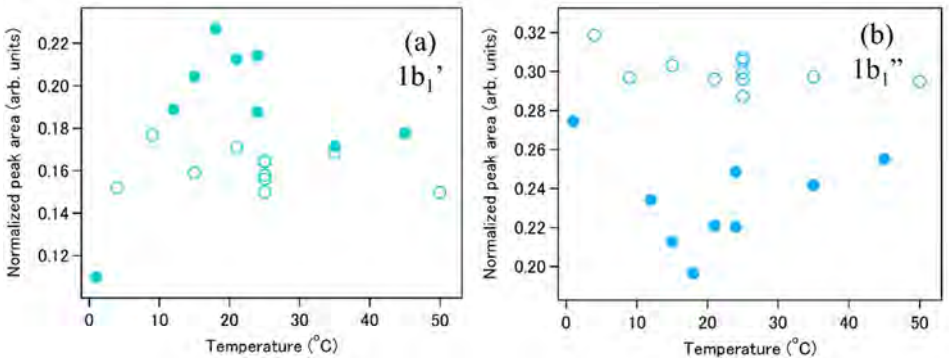

Fig. 2 Temperature dependence of $1b_1$' (a) and $1b_1$" (b) peak areas by fitting. Filled and open circles are the results for water in Nafion and for bulk water, respectively. The result of Nafion was that the area of $1b_1$' was the largest and the area of $1b_1$" was the smallest at 18 °C.

REFERENCES

[1] M. Rikukawa, *Journal of Synthetic Organic Chemistry*, *66*, 488 (2008).
[2] M. Yoshida-Hirahara *et al.*, *RSC Adv.*, *10*, 12810 (2020).

ELECTRONIC STATES OF FUNCTIONAL MATERIALS IN HYDROGEN ADSORPTION/DESORPTION STUDIED BY AMBIENT PRESSURE SOFT X-RAY PHOTOELECTRON SPECTROSCOPY

F. OZAKI, W. OSADA, Y. CHOI, H. YOSHIOKA, S. TANAKA, K. MUKAI, M. HORIO, I. MATSUDA and J. YOSHINOBU

The Institute for Solid State Physics, The University of Tokyo

Introduction

In this research, we have studied the electronic and chemical states of functional materials whose electronic and chemical properties are changed by the interaction with hydrogen, by the use of ambient-pressure photoelectron spectroscopy (AP-XPS) at BL07LSU, SPring-8. Molybdenum disulfide (MoS_2) is a layered material and it has been used as a hydrogenation catalyst [1]. For example, MoS_2 has long been used as a hydrodesulfurization catalyst to selectively remove sulfur from petroleum to produce clean fuels [2]. MoS_2 has also attracted attention for its high activity as a hydrogen evolution electrocatalyst [3]. Thus, understanding the interactions between MoS_2 surfaces and hydrogen is an important issue. Here, we report the interaction of the MoS_2 basal surface and the Pd-deposited MoS_2 basal surface with hydrogen, because it is known that the basal plane of MoS_2 is inert for the dissociation of molecular hydrogen at room temperature.

Experimental

A natural MoS_2 crystal was used as a sample. After the sample was mounted on metal plates, scotch tape was used to peel the surface layers off. The sample was transferred to a load lock chamber within 10 min after the exfoliation and annealed at approximately 550 K for 30 min in an ultrahigh vacuum (UHV) chamber. To prepare a Pd-deposited MoS_2 surface, Pd atoms were deposited on a MoS_2 basal surface at 300 K by resistive heating of a Pd wire. The deposited Pd atoms were considered to aggregate to form islands on the MoS_2 surface at 300 K [4].

AP-XPS measurements were performed in a chamber equipped with a hemispherical electron energy analyzer (SPECS, PHOIBOS150 NAP) at BL07LSU of SPring-8, Japan [5]. All XPS spectra were obtained at room temperature using the photon energy of 680 eV. The binding energies of the measured spectra were calibrated by the Fermi energy of a gold foil on the sample holder. The high-purity H_2 gas was introduced into an ambient-pressure gas cell, where the base pressure was below 5×10^{-10} mbar.

Results and discussion

In the Mo 3d, S 2p, and valence-band photoelectron spectra of a bare MoS_2 surface, little change was observed in the energy shift before and after exposure to hydrogen gas (not shown here; please refer to Ref. 6). At the Pd-deposited MoS_2 surface under hydrogen gas exposure, the Mo 3d, S 2p, valence-band and Pd 3d XPS spectra were measured by AP-XPS [Figure 1(a) –(d)]. The peak energy of Pd 3d gradually shifted to a higher binding energy as a function of hydrogen exposure, which can be ascribed to the dissociative adsorption of molecular hydrogen. We performed fitting of the Pd $3d_{5/2}$ XPS spectra before and after the exposure to hydrogen gas. The fitting result before hydrogen exposure is shown in the lower part of Fig. 1(e), where the low energy component (334.9 eV, green) and high energy component (335.6 eV, blue) can be assigned to the surface and bulk Pd components in the Pd island, respectively Note that each peak in the photoelectron spectra (Mo 3d, S 2p, and valence-band) shifted to a lower binding energy with 0.1 eV [Figure 1(f)]. These results indicate that the dissociation of molecular hydrogen and the adsorption of atomic hydrogen occur on the Pd-deposited sites on the MoS_2 surface, and thereafter hydrogen atoms spillover onto the MoS_2 surface.

The present study shows that the active site for the dissociation of molecular hydrogen is created on an inert MoS_2 basal surface by Pd deposition. In addition, the electronic state of the MoS_2 substrate is modulated by hydrogen atoms spilled over onto the MoS_2 surface. The details of this study have been published elsewhere [6].

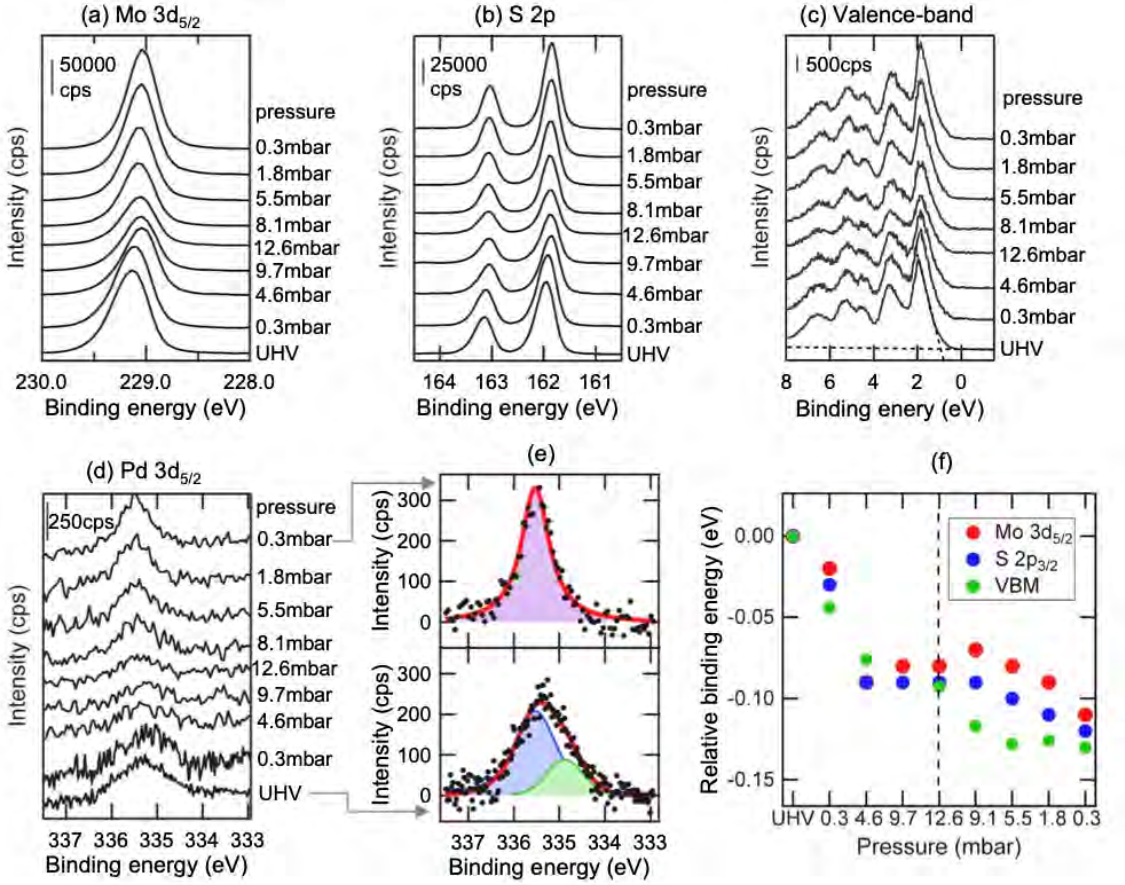

Figure 1 (a) Mo $3d_{5/2}$, (b) S 2p, (c) valence-band, and (d) Pd $3d_{5/2}$ spectra of the Pd/MoS_2 as a function of H_2 gas pressure at 300 K. The amount of deposited Pd was estimated to be 2.0 % for the amount of Mo atoms on the outermost MoS_2 layer. (e) The upper and lower figures show the fitting results for the Pd $3d_{5/2}$ AP-XPS spectra before and after the hydrogen exposure, respectively. The green component and blue component in the lower figure are assigned to be surface and bulk components of the Pd islands, while the pink component consists of both the bulk component and hydrogen atoms-adsorbed surface component. (f) The relative binding energies for the Mo $3d_{5/2}$, S $2p_{3/2}$ and valence band maximum (VBM) as a function gas exposure process. [6].

ACKNOWLEDGMENTS

The AP-XPS measurements using synchrotron radiation were performed at SPring-8 BL07LSU as joint research in the Synchrotron Radiation Research Organization, The Institute for Solid State Physics, The University of Tokyo (Proposal No. 2020A7481, 2021A7426). We thank Mr. Yu Tsuchihara at the initial stage of this research.

REFERENCES

[1] J. Mao et al., Front. Phys. **13** (2018) 138118.
[2] H. Topsøe et al., Ind. Eng. Chem. Fundamen. **25** (1986) 25.
[3] Y. Yan et al., ACS Catal. **4** (2014) 1693.
[4] H. Dong et al., ACS Appl. Mater. Interfaces **9** (2017) 38977.
[5] T. Koitaya et al., Top. Catal. **59** (2016) 526.
[6] F. Ozaki et al., Appl. Surf. Sci. **593** (2022)153313.

O *K*-edge soft X-ray emission spectroscopy of the solvents in electrolyte solutions for redox flow batteries

Eiji Hosono[1,2], Daisuke Asakura[2,3], Akihiro Ohira[3], Wenxiong Zhang[4], Naoya Kurahashi[4], Ralph J. Ugalino[4], Hisao Kiuchi[4], and Yoshihisa Harada[2,4]

[1]*Global Zero Emission Research Center, National Institute of Advanced Industrial Science and Technology (AIST)*

[2]*AIST-UTokyo Advanced Operando-Measurement Technology Open Innovation Laboratory, AIST*

[3]*Research Institute for Energy Conservation, AIST*

[4]*Synchrotron Radiation Laboratory, The Institute for Solid State Physics, The University of Tokyo*

Redox flow battery (RFB) is a rechargeable battery which is attractive for application to large-scale energy storage system. RFBs consist of electrolyte solutions containing the active materials, positive and negative electrodes soaked in the electrolyte solutions, and an electrolyte membrane that separates the two electrodes. It is characteristic for RFBs that the electrolyte solutions are mainly responsible for the redox reactions unlike Li-ion batteries where the solid-state electrodes are redox active. For example, vanadium RFB is most promising for practical use. The redox reaction is vanadium's $V^{4+} \leftrightarrows V^{5+}$ in the electrolyte for cathode and $V^{3+} \leftrightarrows V^{2+}$ in that for anode. Thus, the battery capacity depends on the vanadium ion concentration in the electrolyte solutions.[3]

To increase the capacity of RFBs, it is important to understand the redox reaction at the interface between the active material and the electrode in the electrolyte solution, which is directly connected with the concentration. Thus, the electronic structure analysis is of particular importance. Especially, it is necessary to clarify the solvation and de-solvation behavior of the active material due to the redox reaction. X-ray emission spectroscopy (XES) is one of the promising techniques to understand those properties. For aqueous electrolyte solutions, O *K*-edge XES is highly useful to investigate the coordination mechanisms of H_2O molecules. In this study, we apply O *K*-edge XES to aqueous electrolyte solutions including organic active materials.[1]

The O *K*-edge XES measurements were carried out by using HORNET spectrometer at BL07LSU, SPring-8. The energy resolution was set to 170 meV at 540 eV. The aqueous electrolyte solutions including organic active materials and reference solution samples were put in a flow-type liquid cell with a 150-nm-thick Si_3N_4 membrane window to separate the liquid samples from vacuum. The samples were flowed with a flow rate of 1 ml/min by a peristaltic pump (Fig. 1) during the XES measurements.

Figure 2 shows the O *K*-edge XES spectra for pure H_2O (25 ℃) and 1 M NaCl/H_2O (room temperature) that is used as the solvent of the electrolyte solutions. The excitation energy was 550 eV in the post-edge region at the O *K* edge. The peaks around 521.2, 524.6, 525.8 and 527.7 eV are attributed to $1b_2$, $3a_1$, $1b_1$' and $1b_1$" as reported in previous papers.[2,3] The $1b_1$' and $1b_1$" peaks are of ice-like tetrahedral coordination of H_2O molecules and distorted coordination environment, respectively. For 1 M NaCl/H_2O, the $1b_1$' peak is slightly lower than the $1b_1$" peak in contrast to the spectrum for pure H_2O, suggesting that the H_2O molecules in 1 M NaCl/H_2O should be less coordinated than those in pure H_2O. Moreover, the higher $3a_1$ peak, which is dipole-forbidden transition in tetrahedral symmetry, for 1 M NaCl/H_2O indicates that the H_2O tetrahedron is relatively distorted. The electrolyte solutions including organic active materials showed similar tendencies, while slight differences in the O *K*-edge XES spectra were observed among the solution samples. In the near future, the XES

spectra will be analyzed in detail. Then, we will try the *operando* XES with charge-discharge measurement.

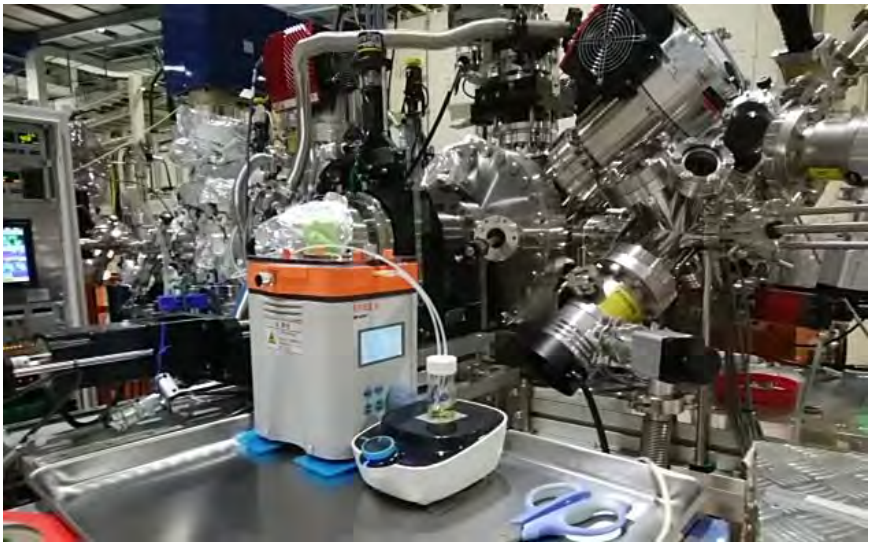

Fig. 1. A picture of the liquid flow system with a peristaltic pump for the *in situ* XES measurements.

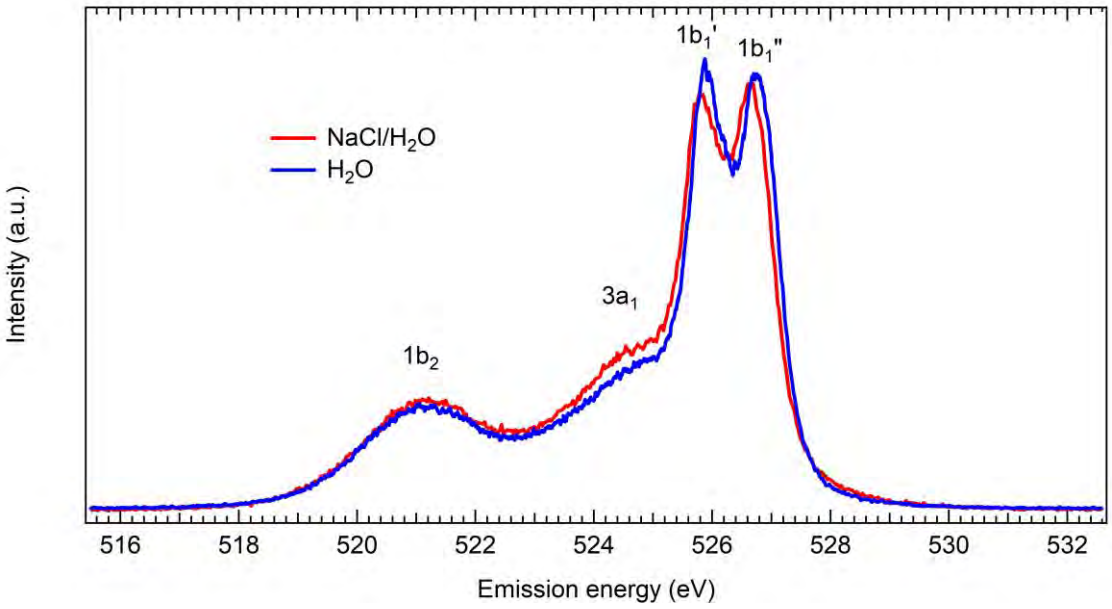

Fig. 2. O *K*-edge XES spectra for $NaCl/H_2O$ and H_2O. The excitation energy was set to 550 eV.

REFERENCES

[1] A. Ohira *et al*., ACS Appl. Energy Mater. **3**, 4377 (2020).
[2] T. Tokushima *et al*., Chem. Phys. Lett. **460**, 387 (2008).
[3] K. Yamazoe *et al*., Langmuir **33**, 3954 (2017).

Co L_3-edge Soft X-ray Emission spectroscopy of $LiCoO_2$ for Li-ion batteries

Daisuke Asakura[1,2], Eiji Hosono[2,3], Kosuke Yamazoe[4], Naoya Kurahashi[4], Ralph J. Ugalino[4], Hisao Kiuchi[4], and Yoshihisa Harada[2,4]

[1]*Research Institute for Energy Conservation, National Institute of Advanced Industrial Science and Technology (AIST)*

[2]*AIST-UTokyo Advanced Operando-Measurement Technology Open Innovation Laboratory, AIST*

[3]*Global Zero Emission Research Center, AIST*

[4]*Synchrotron Radiation Laboratory, The Institute for Solid State Physics, The University of Tokyo*

Li-ion battery (LIB) is one of the key energy-storage devices for CO_2 reduction. To further enhance the performances of LIBs for applications to electric vehicles and large-scale stationary energy storage systems, increasing the charge-discharge capacity of the cathode is highly demanded. Electronic-structure analysis using X-ray spectroscopy has been playing an important role on the clarification of the redox mechanism of cathode materials, which will lead to increase of the charge-discharge capacity. By clarifying the redox mechanism of typical cathode materials, strategies for designing novel cathode materials could be obtained.

We have been studying the electronic structure of several cathode materials using soft X-ray absorption (XAS) and emission spectroscopy (XES). For example, the Mn *L*-edge XAS and XES studies for $LiMn_2O_4$ revealed the redox reaction of $Mn^{3+} \Leftrightarrow Mn^{4+}$ at the Mn^{3+} site in the initial state. The Mn^{4+} state has very strong charge-transfer effect between the O 2*p* and Mn 3*d* orbitals, resulting in the important role of O 2*p* orbital on the redox reaction.[1,2] For $LiFePO_4$, the redox reaction of Fe was confirmed by Fe *L*-edge XAS and XES, which was attributed to simple ionic redox of $Fe^{2+} \Leftrightarrow Fe^{3+}$.[3] Then, $LiCoO_2$ (LCO) is a prototypical cathode material for practical use like $LiMn_2O_4$ and $LiFePO_4$. While the electronic structure of LCO has been studied by XAS,[4] we demonstrate the Co *L*-edge XES to further understand the Co 3*d* and O 2*p* orbitals.

Powdered LCO sample was pasted with acetylene black and PTFE. The pasted LCO electrode was assembled as a three-electrode beaker cell with Li-metal counter and reference electrodes and an organic electrolyte solution. We prepared two cells to make charged-state and discharged-state samples with different modes by cyclic voltammetry. The charged/discharged cells were disassembled in an Ar-filled glovebox. The LCO samples were transferred from the glovebox to a transfer vessel without exposure to the air. *Ex situ* Co *L*-edge XAS and XES measurements for the pristine and the two charged samples were carried out by HORNET spectrometer at BL07LSU, SPring-8. The energy resolution for the XES measurement was set to 330 meV at 785 eV.

Figure 1 shows the Co L_3-edge XES spectra measured with an excitation energy of 780.4 eV. Considering the Co $L_{3,2}$-edge XAS results (not shown), the XES spectrum for the initial state should be of Co^{3+} low-spin state as with the XAS spectrum. On the other hand, the XES line shape is relatively different from that for $LaCoO_3$ having a Co^{3+} low-spin electron configuration.[5] One of the reasons should be the lower symmetry of the CoO_6 octahedron in LCO, which should reflect the different structures for the *dd* excitation around 779 eV compared to the XES results for $LaCoO_3$.[5] These differences could be obtained by the high-resolution XES while the XAS line shapes of both LCO and $LaCoO_3$ are quite similar.

For the charged state, the XES line shape is greatly changed, indicating that the oxidation reaction of Co due to charge (Li-extraction) reaction. For the discharged state, the line shape is almost the same as the initial state. Therefore, the redox reaction of Co is highly reversible.

The XES spectra will be analyzed by using charge-transfer multiplet calculations in detail. We will focus on the charge-transfer effect between the O 2*p* and Co 3*d* orbitals like $LiMn_2O_4$.[1,2] Then, the relation between the electronic structure and the electrode performance will be further investigated. Also, we will try the *operando* measurement with an all-solid-state-type *operando* cell for LIB (under construction), because LCO works in all-solid-state LIB[6] which is highly attractive for application to electric vehicles.

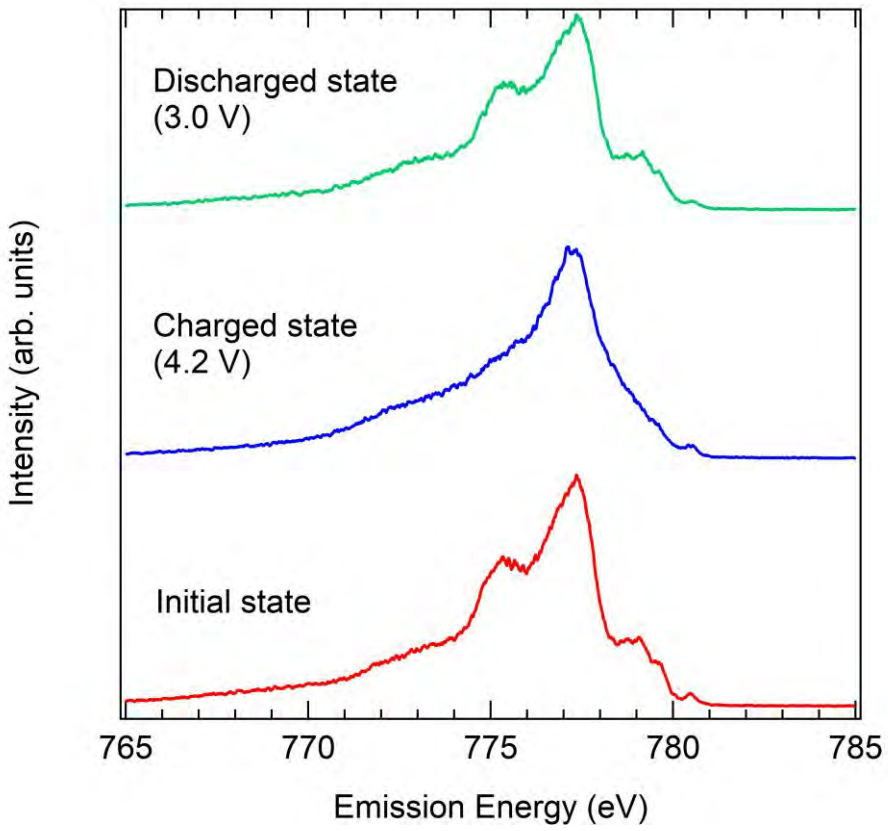

Fig. 1. Co L_3-edge XES spectra for $LiCoO_2$. The excitation energy was set to 780.4 eV.

REFERENCES

[1] D. Asakura *et al*., Electrochem. Commun. **50**, 93 (2015).
[2] D. Asakura *et al*., Phys. Chem. Chem. Phys. **21**, 18363 (2019).
[3] D. Asakura *et al*., ChemPhysChem **19**, 988 (2018).
[4] For example, W.-S. Yoon *et al*., J. Phys. Chem. B **106**, 2526 (2002) and T. Mizokawa *et al*., Phys. Rev. Lett. **111**, 056404 (2013).
[5] Y. Yokoyama *et al*., Phys. Rev. Lett. **120**, 206402 (2018).
[6] For example, Y. Kato *et al*., J. Phys. Chem. Lett. **9**, 607 (2018).

REAL-TIME OBSERVATION OF HYDROGEN-ABSORPTION PROCESS IN PD-AU ALLOYS BY OPERANDO AP-XPS

Takanori KOITAYA,[1, 2] Susumu YAMAMOTO,[3, 4] Masafumi HORIO,[5] Iwao MATSUDA,[5] Jun YOSHINOBU,[5] and Toshihiko YOKOYAMA[1]

1 Department of Materials Molecular Science, Institute for Molecular Science
2 Precursory Research for Embryonic Science and Technology (PRESTO), Japan Science and Technology Agency (JST)
3 International Center for Synchrotron Radiation Innovation Smart (SRIS), Tohoku University
4 Institute of Multidisciplinary Research for Advanced Materials (IMRAM), Tohoku University
5 The Institute for Solid State Physics, The University of Tokyo

Palladium-based alloys are widely known as hydrogen storage materials, and hydrogen absorption/desorption processes on the sample surfaces have been extensively studied. Palladium-gold (Pd-Au) alloy is expected to be used in various fields such as a hydrogen sensor [1] and a heterogeneous catalyst [2]. It has been also revealed that the adding gold to palladium promotes hydrogen absorption compared with pure palladium, which is caused by destabilization of chemisorbed surface hydrogen and decrease of a hydrogen penetration barrier from the surface into the subsurface [3].

In order to clarify the effects of the alloying with gold in the hydrogen absorption process, it is very important to perform operando spectroscopy under the conditions in which the absorption of hydrogen occurs. In this study, we measured the electronic states of the Pd-Au alloys during the hydrogen adsorption/desorption processes by soft X-ray near ambient-pressure photoelectron spectroscopy (AP-XPS), to reveal the nature of the interaction between the palladium alloy and absorbed hydrogen.

The experiments were performed using the AP-XPS system installed at the SPring-8 BL07LSU. Recently, the AP-XPS apparatus was improved, which enables AP-XPS measurements at higher gas-phase pressures up to 100 mbar. As a result, real-time AP-XPS measurements of the hydrogen adsorption/desorption processes have become possible with enough signal intensity and energy resolution to detect change in the chemical states of the Pd-Au alloys by the interaction with absorbed hydrogen. Before the AP-XPS experiments, the Pd-Au samples were cleaned by a cycle of Ar^+ ion sputtering and annealing.

A series of AP-XPS spectra were measured while controlling the hydrogen pressure with a constant ramp rate (β = 0.01 mbar/s) at a sample temperature of 297.2 K. Figures 1(a) and (b) show the Pd 3d and Au 4f AP-XPS spectra of the Pd-Au alloy sample during the absorption and desorption processes as a function of hydrogen pressure. When the hydrogen pressure rises to about 15 mbar, hydrogen absorption occurs and the core-level peaks of the substrate change accordingly (Fig. 1(a)). In Fig. 1 (b), the spectral change in the hydrogen desorption process is observed at hydrogen pressure of 5 mbar. The transition pressure is clearly different between the absorption process and the desorption process (pressure hysteresis). This result indicates that the observed change in the chemical states of the alloy is caused by a metal-hydride phase transition.

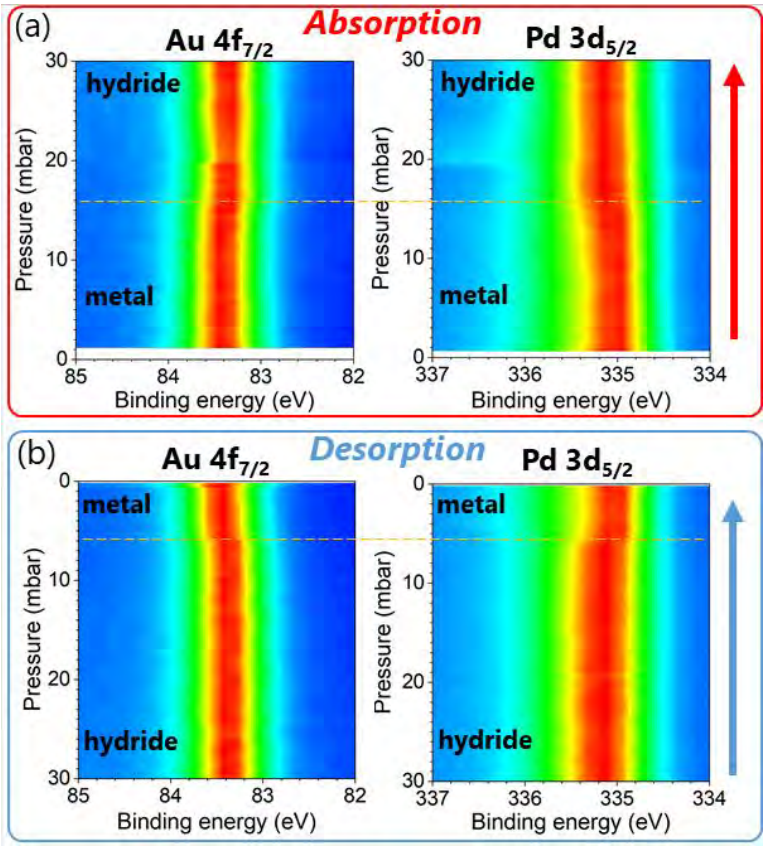

Figure 1. A series of Au 4f and Pd 3d AP-XPS spectra of the Pd-Au alloy (Au: 12 at%) in (a) absorption and (b) desorption processes as a function of hydrogen pressure. The gas-phase pressure was linearly changed at a constant rate of 0.01 mbar/s, whereas sample temperature was kept at 297.2 K. All the spectra were measured at photon energy of 1600 eV.

REFERENCES

[1] C. Wadell et al., Nano Lett. **15**, 3563 (2015).
[2] Y. He et al., Catal. Today **339**, 48 (2020).
[3] K. Namba et al., Proc. Natl. Acad. Sci. **115**, 7896 (2018).

HALF-METALLIC ELECTRONIC STATES OF BULK-SINGLE CRYSTAL Co_2MnZ (Z = Ge AND Ga) HEUSLER ALLOYS PROBED BY RESONANT INELASTIC SOFT X-RAY SCATTERING (SX-RIXS) IN A MAGNETIC FIELD

Rie Y. Umetsu[1], Hidenori Fujiwara[2], Jun Miyawaki[3], Rika Kasahara[2], Takuma Nishioka[2], Akane Ose[2], Akira Sekiyama[2], Yoshihisa Harada[4,5] and Shigemasa Suga[6]

[1] *Institute for Materials Research (IMR), Tohoku University, Miyagi, Japan*
[2] *Graduate School of Engineering Science, Osaka University, Osaka, Japan*
[3] *National Institutes for Quantum and Radiological Science and Technology (QST), Miyagi, Japan*
[4] *The Institute for Solid State Physics (ISSP), The University of Tokyo, Tokyo, Japan*
[5] *Synchrotron Radiation Research Organization, The University of Tokyo, Hyogo, Japan*
[6] *SANKEN, Osaka University, Osaka, Japan*

Introduction

In our research group, several kinds of Heusler alloys have been investigated by soft x-ray resonant inelastic x-ray scattering (SX-RIXS) measurements in magnetic field to reveal their half-metallic electronic structures [1-3]. The RIXS is a bulk sensitive photon-in and photon-out spectroscopy, and very powerful to investigate such as *d*-*d* excitations for open shell 3*d* orbitals and magnetic excitations for spin systems as well as 2*p*-3*d* transitions in element- and symmetry-specific ways. From comparison between the experimental and theoretical spectra, it was found that the quantitative analyses of the spin-polarized valence band electronic structures related to the half-metallicity would be possible, including such as the Zeeman splitting energy and the spin dependent band gap width across the Fermi level.

RIXS experiments for single crystal of bulk Co_2FeSi Heusler alloy was performed in a previous study. This material has been controversial as a half-metallic ferromagnet, because the given spin polarization is different depending on the theoretical calculation method [4]. The weak structure in the RIXS-MCD spectra between the elastic component and strong fluorescence component suggested the existence of the density of states of Fe-3*d* orbitals at the Fermi level, suggesting that the obtained results follow the electronic structures given by the generalized gradient approximation (GGA) but not by the local density approximation with considering the electron-electron correlation (LDA+U) [4].

In the present study, we focus on the Co_2MnGa Heusler alloy, which is predicted as one of the Weyl semimetals. It would be very useful to discuss the difference of the electronic structures between such a Weyl semimetal and typical half-metallic materials as Co_2MnSi and Co_2MnGe.

Experiments

a) Sample preparation

Single crystals of bulk Co_2MnGe and Co_2MnGa was prepared by Bridgman method after preparing a master alloy by induction furnace melting in Ar gas atmosphere, and annealed at 1273 and 1323 K, respectively. The sample compositions identified by scanning electron microscope-energy dispersive x-ray spectrometry were Co: 49.3, Mn: 24.9, Ge: 25.8 at.%, and Co: 49.4, Mn: 25.2, Ga: 25.4 at.%. Crystal orientations were checked by the Laue method and the specimens were cut in the stripe form with the length of 5 mm along the <100> with about 1 × 1 mm^2 cross section. Magnetic properties were investigated with SQUID magnetometer and the magnetic moments converted from the spontaneous magnetizations at 5 K for Co_2MnGe and Co_2MnGa were 4.96 and 4.07 μ_B/f.u., respectively, and the Curie temperatures measured by differential scanning calorimetry were 913 and 697 K, respectively.

b) RIXS experiment

RIXS experiments were performed using a high-resolution soft x-ray emission

spectrometer installed at the end of the BL07LSU of SPring-8. The specimens were fractured in a VUV chamber. The RIXS spectra for Mn 2*p* core excitation were measured with use of the right and left helicity circularly polarized light at room temperature. A permanent magnet with the field of 0.25 T was installed in the chamber and arranged as the x-ray incidence direction and the magnetic field direction become parallel.

Results

Figures (a) and (b) show the intensity maps of RIXS-MCD spectra obtained by parallel (μ^+) and antiparallel (μ^-) configurations between the photon helicity and the magnetic field at incoming photon energy, for Mn L_3 edge in Co_2MnGe and Co_2MnGa, respectively. Strong RIXS-MCD signals are recognized in both the elastic and fluorescence components. The former is observed at the zero-energy loss and the latter shifts linearly with the excitation photon energy. The fluorescence MCD signals contain both negative (blue) and positive (red) signs. The blue area is dominant in lower incoming photon energy regions, and the red area dominates in higher energy regions.

Figures (c) and (d) are intensity maps obtained by calculated spectra of RIXS-MCD for Mn L_3 edge in Co_2MnGe and Co_2MnGa, respectively. The features pointed out above are qualitatively reproduced. In details, the distributions of the RIXS-MCD of the fluorescence components for Co_2MnGa are slightly shifted to lower energy loss regions, reflecting the different number of the electrons in the valence band between Co_2MnGa and Co_2MnGe.

REFERENCES

[1] K. Nagai, H. Fujiwara *et al*., Phys. Rev. B 97 (2018) 035143.
[2] R.Y. Umetsu *et al*., Phys. Rev. B 99 (2019) 134414.
[3] H. Fujiwara *et al*., Sci. Rep., 11 (2021) 18654.
[4] K. Nishimoto, H. Fujiwara, R.Y. Umetsu *et al*., in preparation.

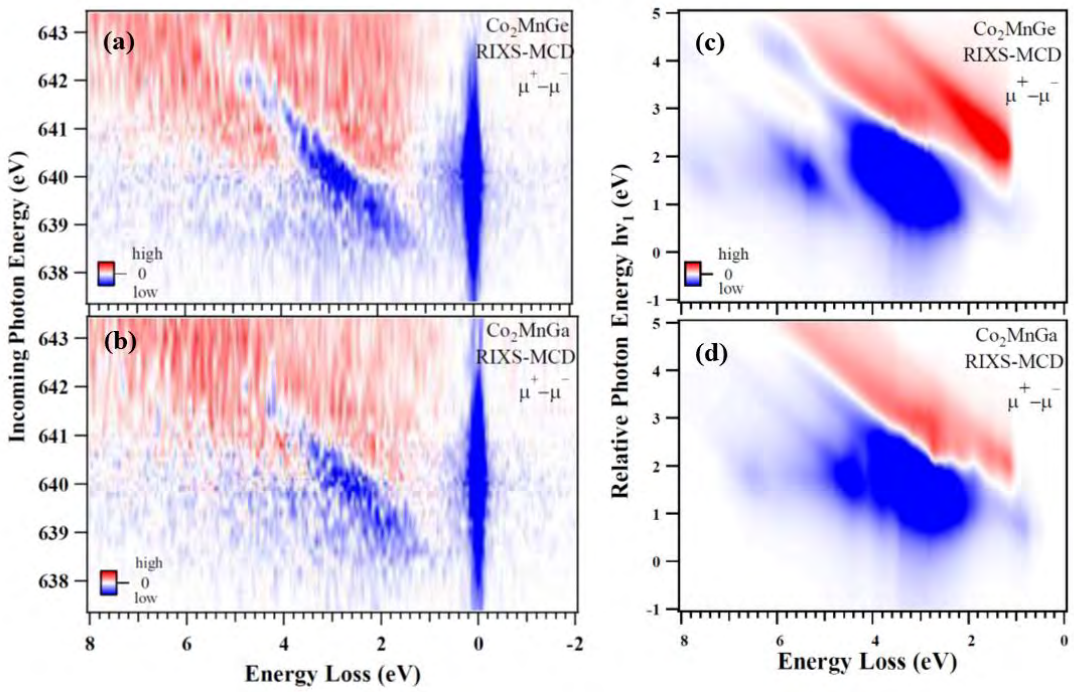

Figs. Intensity maps of RIXS-MCD spectra for L_3 edge in Co_2MnGe (a) and Co_2MnGa (b). The RIXS spectra recorded for parallel (μ^+) and antiparallel (μ^-) configurations of the photon helicity. Calculated spectra by Kramers-Heisenberg formula based on the GGA for Co_2MnGe (c) and Co_2MnGa (d).

KINETIC SQUARE SCHEME IN OXYGEN-REDOX BATTERY ELECTRODES

Masashi OKUBO
Department of Electrical Engineering and Bioscience, School of Advanced Science and Engineering, Waseda University

The rapid market growth of electric vehicles (EVs) has significantly increased the industrial demands for their improved performance, such as longer driving distance, longer calendar life, and lower cost. For example, the driving distance of an EV is determined by the energy density of in-vehicle lithium-ion batteries (LIBs). However, current LIBs possess an unsatisfactory gravimetric energy density of 200–250 Wh/kg, powering typical EVs for 300–400 km per charge, which is below most consumers' requirements. Thus, increasing the energy density of LIBs is crucial for the widespread use of EVs. The energy density of LIBs is limited in part by the specific capacity of the positive electrode (cathode) material. Conventional cathode materials, i.e., layered transition-metal oxides $LiMO_2$ (M = transition metal), deliver a modest capacity of approximately 160 mAh/g, where the dominant mechanism of charge compensation for lithium-ion (de)intercalation is the valence change of the transition metal. Further increase in the cathode capacity requires an additional redox center. To activate redox reactions of oxide ions (oxygen redox), lithium-rich transition-metal oxides have been extensively studied for over a decade as they deliver much larger reversible capacities (> 200 mAh/g).

This work focuses on O2-type lithium-rich layered transition-metal oxides as cathode materials with structural integrity (O2: lithium ions occupy octahedral sites between the MO_2 layers and the packing arrangement of the oxide ions is ABCBA), which is an emerging class of oxygen-redox electrode materials. In the O2-type oxides, the structural degradation upon cycling is suppressed because migration of M to the Li^+ layers is unfavorable: M in a Li^+ layer

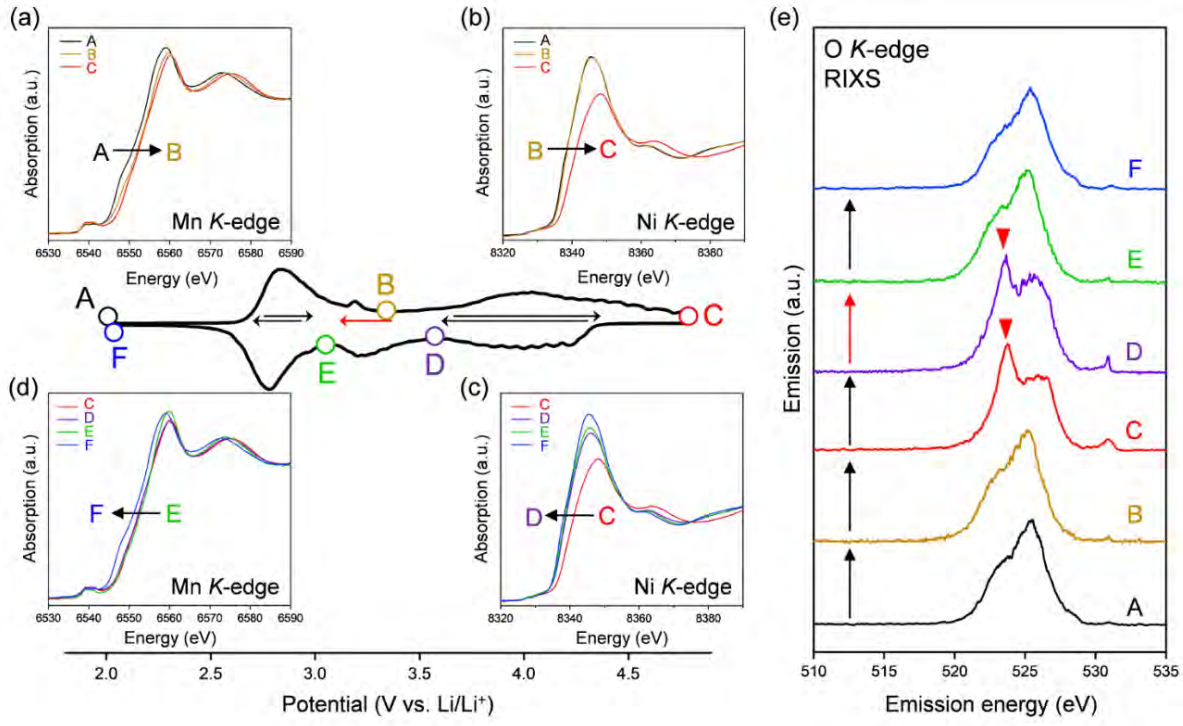

Figure 1. Redox couples in O2-$Li_{1.12-y}Ni_{0.17}Mn_{0.71}O_2$. dQ/dV plot during the second cycle at a charge/discharge rate of C/20. (a–d) Ex situ Mn and Ni K-edge X-ray absorption spectra upon charge and discharge. (e) Ex situ O K-edge resonant inelastic X-ray scattering (RIXS) spectra excited by an incident photon energy of 531 eV.

suffers from strong Coulombic repulsion from face-sharing M^{n+} in an adjacent MO_2 layer. Moreover, O2-type Li-rich layered oxides exhibit negligible O2 gas release. As a consequence, O2-$Li_{1.12-y}Ni_{0.17}Mn_{0.71}O_2$ provides a large reversible capacity greater than 200 mAh/g with minimal voltage decay and capacity fading upon cycling.

O2-$Li_{1.12-y}Ni_{0.17}Mn_{0.71}O_2$ was synthesized by the Na^+/Li^+ ion-exchange method using P2-$Na_{0.71}[Li_{0.12}Ni_{0.17}Mn_{0.71}]O_2$ as a precursor. The powder X-ray diffraction pattern of O2-$Li_{1.12-y}Ni_{0.17}Mn_{0.71}O_2$ shows Bragg peaks indexed to a hexagonal system (space group: $P6_2mc$, typical of the O2 phase), indicating the successful transformation of the P2-type sodium layered oxide to the O2-type lithium layered oxide. Indeed, a high-angle annular dark-field scanning transmission electron microscopy image confirms the O2-type stacking of the transition-metal layers. Galvanostatic charge/discharge measurements show that O2-$Li_{1.12-y}Ni_{0.17}Mn_{0.71}O_2$ delivers a large discharge capacity of approximately 210 mAh/g, exceeding the M-redox capacity (193 mAh/g). After 80 cycles, 98% of the discharge capacity in the second cycle is retained, while the decay of the average discharge voltage is negligibly small (< 5 mV). Typically, conventional O3-type oxygen-redox layered oxides exhibit structural degradation initiated by the migration of M to Li^+ layers. In contrast, in O2-type layered oxides, M^{n+} ions migrated to Li^+ layers would be subjected to strong Coulombic repulsion from face-sharing M^{n+} ions in the adjacent MO_2 layers, such that the migration of M would be energetically unfavorable to mitigate both capacity fading and voltage decay during the charge/discharge cycles.

To identify the redox center, ex situ X-ray absorption/emission spectroscopy measurements were conducted. Mn and Ni K-edge X-ray absorption near-edge structure (XANES) spectra during the second cycle show that the redox reaction at 2.8 V vs. Li/Li^+ corresponds to the oxidation and reduction of Mn while that at 3.9 V vs. Li/Li^+ can be attributed to the oxidation and reduction of Ni (Figure 1a-d). These attributions (Mn and Ni redox reactions at 2.8 and 3.9 V vs. Li/Li^+, respectively) are double-confirmed by Mn and Ni *L*-edge absorption spectra. After charging to 4.8 V vs. Li/Li^+, O K-edge X-ray absorption spectroscopy shows the emergence of new absorption at approximately 531 eV, while resonant inelastic X-ray scattering (RIXS) spectra with the incident photon energy of 531 eV show intense emission at 524 eV (Figure 1e), both of which are characteristic features of charged oxygen-redox electrode materials. Thus, the anodic dQ/dV peak at 4.5 V vs. Li/Li^+ corresponds to the oxidation of oxide ions. These signals for oxidized oxygen do not completely disappear even after discharging to 3.6 V vs. Li/Li^+. Instead, the disappearance is confirmed after discharging to 3.1 V vs. Li/Li^+. Considering the similar emission peaks observed for Li_2O_2, CaO_2, and O_2 molecule, dimerized oxygen species O_2^{n-} (n = 0 or 2) exists in charged O2-$Li_{1.12-y}Ni_{0.17}Mn_{0.71}O_2$ at 4.5 V. It is noteworthy that an enhancement in the elastic peak region was observed after charge (spectrum C and D in Figure 1e). A possible explanation is the Raman scattering arising from the vibrational transition of O–O bond although its origin is still under debates.

Overall, the O–O dimerization in O2-$Li_{1.12-y}Ni_{0.17}Mn_{0.71}O_2$ can be summarized by the square scheme. Upon charge, O^{2-} with non-bonding 2p states is oxidized to O^- above 4.2 V vs. Li/Li^+. At the early stage of oxygen oxidation, O^- is thermodynamically more favorable than O_2^{2-}. However, with further oxygen oxidation, the over-oxidized oxide ions dimerize to form O_2^{2-}.

REFERENCES

[1] K. Kawai, X. M. Shi, N. Takenaka, J. Jang, B. Mortemard de Boisse, A. Tsuchimoto, D. Asakura, J. Kikkawa, M. Nakayama, M. Okubo, A. Yamada, *Energy Environ. Sci.* **2022**, *15*, 2591-2600

ORBITAL TORQUE IN COFE/CU/AL$_2$O$_3$: INVESTIGATION ON THE LARGE TORQUE WITHOUT HEAVY ELEMENT

Junyeon KIM
Center for Emergent Matter Science, RIKEN

Introduction

Recently, sizeable orbital torque is experimentally observed in CoFe/Cu/Al_2O_3 stacks [1]. This orbital torque is indeed caused by the generation of nonzero orbital angular momentum (OAM) at the Cu/Al_2O_3 interface (Fig. 1). Nowadays, the orbital torque greatly draws interest for the spin accumulation since there is no clear restrictions on materials for the nonzero OAM generation. It is apparently contrast to the spin angular momentum generation which is mainly shown in material systems consisted of heavy elements.

A recent theoretical study reports that the orbital hybridization between the *p*-orbital of oxygen atom and the *d*-orbital atom serves the formation of a chiral orbital texture by orbital Rashba effect (Fig. 1(a)) [2]. For further understand on the nonzero OAM generation at the Cu/Al_2O_3 interface, we require detailed material characterization. Also observation of a modulation of the energy spectrum by a generation of nonzero OAM is also desired.

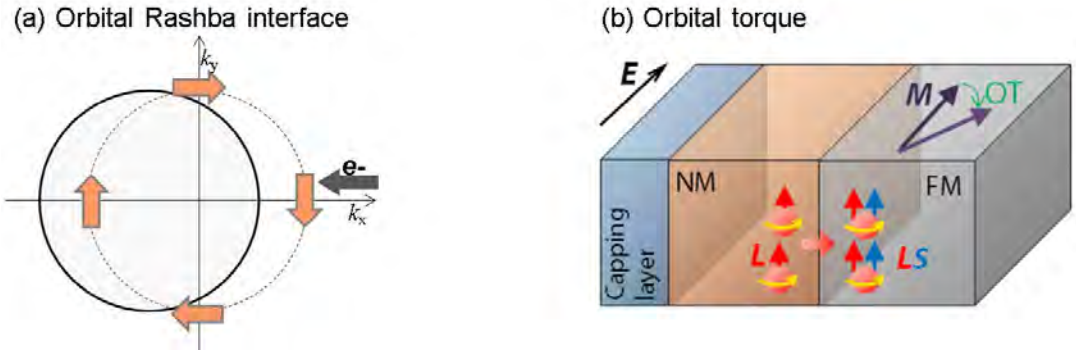

Fig. 1(a)Excess OAM generation at a chiral orbital texture. Here the chiral orbital texture is formed by orbital Rashba effect. (b) Orbital torque in FM/Cu/Oxide system.

Experimental method

For the observation of the Cu/Al_2O_3 interface, L-edge X-ray magnetic circular dichroism (XMCD) was utilized. Nominally, the 3*d* orbital state of Cu is known to be fully occupied. However Grioni et al. claimed that there is still unoccupied 3*d* orbital state for Cu due to a hybridization between *s* state and *d* states [3]. And the number of unoccupied 3*d* orbital state can be promoted by formations of compounds such as CuOx. Thus we could expect the L2, 3 edge X-ray absorption.

As a first, we attempt to obtain the energy spectrum nearby the Cu/Al_2O_3 interface. Next, we also attempt to obtain a clue of the nonzero OAM generation by turning on/off the charge current.

The observation was performed in superconducting magnet magneto-optical observation system in the free board. The CoFe/Cu/Al_2O_3 and the Cu/Al_2O_3 stacks are electronically connected by the silver paste. And the observation was carried out by high speed switching of the circularly polarized light and total electron yield (TEY) technique. To optimize the sample condition, 2, 5, 7, 10 nm of Al_2O_3 was tested considering with the detection length of the TEY technique (~10 nm).

Experimental results and discussion

As shown in Fig. 2, the energy spectrum is successfully obtained by the TEY technique for the CoFe/Cu/Al_2O_3 and the Cu/Al_2O_3 stacks. Here the Cu peak is clearly found for all the stacks, but the CuO or Cu_2O peak is not shown. It asserts that formation of Cu oxide mostly does not occur, although temperature would drastically increase during the Al_2O_3 layer deposition. We think the Al_2O_3 is extremely stable as showing large Gibbs free energy, thus it is not easily decomposed even in extreme conditions. We think this result is quite helpful for further analysis of the interfacial condition. We also attempt to observe the nonzero OAM generation by the XMCD, but it is not successful due to a drastic Joule heating during the observation..

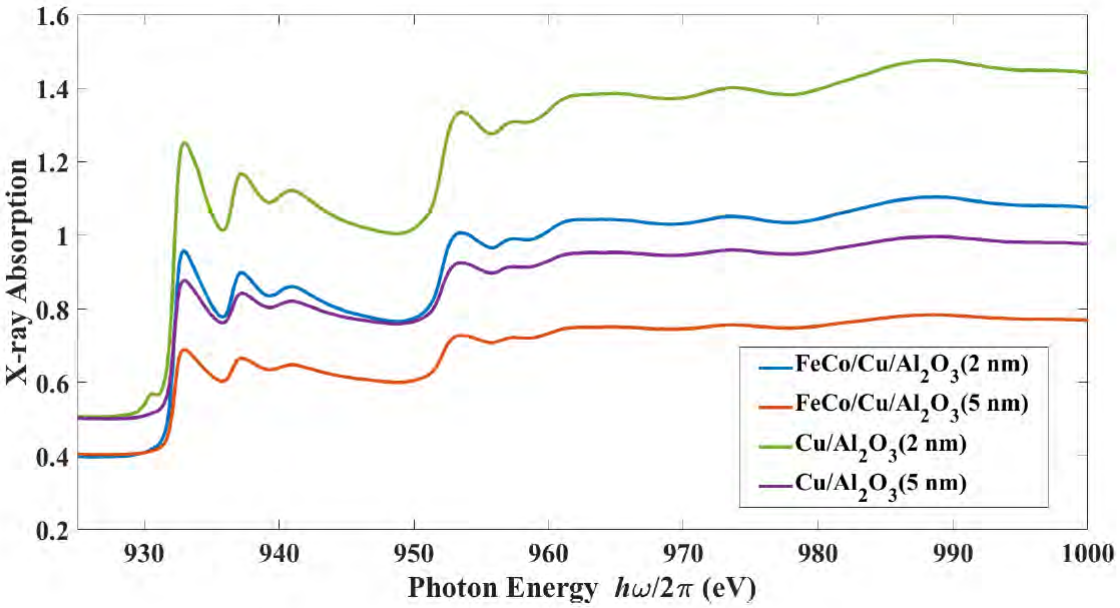

Fig. 2 Energy spectrum for the several CoFe/Cu/Al_2O_3 and the Cu/Al_2O_3 stacks observed by the TEY technique.

REFERENCES

[1] J. Kim *et al*. Phys. Rev. B **103**, L020407 (2021).
[2] D. Go *et al*., Phys. Rev. B **103**, L121113 (2021).
[3]M. Grioni *et al*., Phys. Rev. B **39**, 1541 (1989).

MAGNETIC STATE OF VNB3S6 DETERMINED BY X-RAY MAGNETIC CIRCULAR DICHROISM

Masafumi HORIO[1], Tomoaki SENOO[1], Tetsuya WADA[1], Yasuyuki HIRATA[2], Shota OKAZAKI[3], Takao SASAGAWA[3], Iwao MATSUDA[1]

[1]*The Institute for Solid State Physics, The University of Tokyo*

[2]*Department of Applied Physics, National Defence Academy*

[3]*Materials and Structures Laboratory, Tokyo Institute of Technology*

Transition metal dichalcogenides TX_2 (T = Mo, Nb, W, X = S, Se, Te) are model semiconductors with various intriguing aspects such as charge ordering, Weyl semimetalicity, valleytronics, Mottness, and superconductivity, and have established themselves as a major research field in condensed matter physics. In the 1970s and 1980s, there has been a trend to extend the physical properties of TX_2 by intercalating 3*d* metal M into TX_2. It was demonstrated that magnetic ordering appears with a strong dependence on the inserted 3*d* transition metal [1]. One of the reasons why the MT_3X_6 system attracted much attention is that the intercalation of Cr into NbS_2 results in a helical magnetic structure called chiral soliton lattice. Recently, due to the coexistence of the space-inversion and time-reversal symmetry breaking, the MT_3X_6 system has attracted a renewed attention from a topological point of view. In particular, VNb_3S_6, which is known to be ferromagnetic below Tc~50 K, has been predicted by first-principles calculations to host a Weyl point in the ferromagnetic phase and exhibit an anomalous Hall effect [2]. The prediction has triggered intense efforts to synthesize high-quality MT_3X_6 single-crystal samples and to evaluate their physical properties. Surprisingly, a recent neutron scattering study [3] reported that VNb_3S_6 is not ferromagnetic but in a canted antiferromagnetic state, contrary to the understanding accepted for 40 years [1]. Under these circumstances, it is required to precisely determine the intrinsic magnetic state of VNb_3S_6, excluding the possibility of impurities, in order to elucidate the origin of the anomalous Hall conductivity of VNb_3S_6.

We have therefore performed x-ray absorption spectroscopy (XAS) and x-ray magnetic circular dichroism (XMCD) measurements of VNb_3S_6 single crystals. The samples were cleaved in air and immediately introduced into an ultra-high vacuum chamber equipped with a superconducting magnet at SPring-8 BL07LSU. The measurements were conducted in the total electron yield mode at T = 30 K, below the magnetic transition temperature, under a magnetic field of 3 T. Both normal and grazing (20 degree) incidence conditions were employed.

Figure 1 shows the XAS and XMCD spectra of VNb_3S_6 measured with the grazing incidence condition. Whereas transition-metal ions intercalated into NbS_2 have been usually assumed to be trivalent, the broad absorption spectrum without well-defined pre-edge does not seem compatible with V^{3+} [4-6]. Instead, it is more consistent with intermediate valence state lower than 3+, as seen in systems like $V_{0.1}(Bi_{0.32}Sb_{0.68})_{1.9}Te_3$ [7]. This deviation suggests strong hybridization of V orbitals with surrounding NbS_6 layers. The spectral shape of obtained XMCD spectrum is also close to that of $V_{0.1}(Bi_{0.32}Sb_{0.68})_{1.9}Te_3$ [7] rather than those of the V^{3+} compounds [4-6], further supporting this conclusion. Due to the overlap of L_2 and L_3 absorption edges, the sum rule cannot be applied for V L-edge XMCD and hence it is not straightforward to quantitatively evaluate the magnetic moment. Nevertheless, a naive comparison with a cluster calculation [6] yields an approximate value of ~0.4 μ_B which is one order of magnitude smaller than the values from previous magnetization measurements which reported ferromagnetism [1]. The magnitude of the XMCD signal did not substantially change under the normal incidence setup (not shown). The obtained results are therefore in favor of

canted antiferromagnetism rather than the ferromagnetism. Combined with our ongoing photoemission measurements, the present work will establish the electronic structure of VNb_3S_6 and set a starting point to discuss the origin of anomalous Hall conductivity.

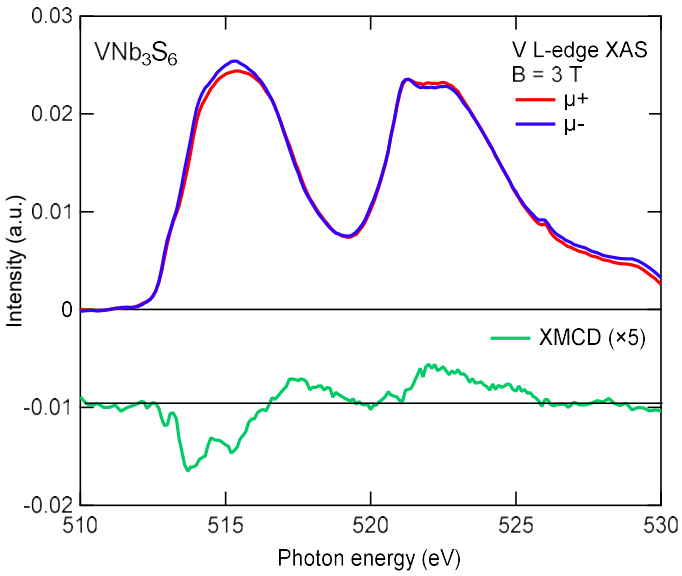

Fig. 1: XAS and XMCD spectra of VNb_3S_6 measured at the incidence angle of 20 degree and at T = 30 K under the magnetic field of 3 T.

REFERENCES

[1] S.S.P. Parkin *et al*, Philos. Mag. B **41**, 65 (1980).
[2] T. Inoshita *et al*., Phys. Rev. B **100**, 121112(R) (2019).
[3] K. Lu *et al*., Phys. Rev. Mater. **4**, 054416 (2020).
[4] M. Abbate *et al*., J. Electron Spectrosc. Relat. Phenom. **62**, 185 (1993).
[5] M. Horio *et al*., J. Phys. Spc. Jpn. **87**, 105001 (2018).
[6] Y. Nonaka *et al*., Phys. Rev. B **97**, 205126 (2018).
[7] T. R. F. Peixoto *et al*., npj Quantum Materials **5**, 87 (2020).

MEASUREMENT OF X-RAY MAGNETIC LINEAR DICHROISM BY ROTATING POLARIZATION ANGLE OF SOFT X-RAY GENERATED BY A SEGMENTED CROSS UNDULATOR

Masafumi HORIO[1], Yoshiki KUDO[1], Toshihide SUMI[1], Tetsuya WADA[1], Yasuyuki HIRATA[2], Kohei YAMAMOTO[3], Takuo OHKOCHI[4,5], Toyohiko KINOSHITA[4], Iwao MATSUDA[1]

[1]*The Institute for Solid State Physics, The University of Tokyo*

[2]*Department of Applied Physics, National Defence Academy*

[3]*Department of Materials Molecular Science, Institute for Molecular Science*

[4]*Japan Synchrotron Radiation Research Institute (JASRI)*

[5]*RIKEN SPring-8 Center*

X-ray magnetic linear dichroism (XMLD) is a widely used technique for studying magnetic anisotropy. By measuring the absorption of soft X-rays while changing the relative angle between the linear polarization of the soft X-rays and the crystal axis, information about the orientation of the spin of the magnet can be obtained. Because of the limitation in controlling the polarization of soft X-rays, the sample is conventionally rotated around a certain axis to perform XMLD measurements. Therefore, the measurement conditions were limited, especially when measuring non-uniform samples under *operando* conditions. In the present study, we report a novel method for XMLD measurements operated by continuously rotating the linear polarization angles while samples are fixed.

At BL07LSU at SPring-8, continuous polarization modulation of a soft X-ray beam was achieved using a segmented cross undulator [1]. The source consists of eight insertion devices (IDs) and seven phase shifters; the ID segments are a horizontal figure-8 undulator and a vertical figure-8 undulator, which generate horizontal and vertical linear polarization, respectively. To generate linear polarization at arbitrary angles, we first prepared two sets, set A and set B, consisting of two sets of horizontal and vertical figure-8 undulators, as shown in Fig. 1. By adjusting phase shifters #1-3 and #5-7, each set can generate right or left circular polarization. For example, the four undulators in the front (set A) generate right circular polarization, while the four undulators in the rear (set B) generate left circular polarization. The roles of Set A and Set B can be interchanged. The two waves of right and left circular polarization are then combined to produce linear polarization. There, the rotation angle of the linearly polarized light was controlled by changing the phase between Set A and Set B using a phase shifter (PS#4 in Fig. 1). As a sample, we prepared a single crystal of NiO (Néel temperature $T_N = 523$ K). The crystal was cleaved with a knife to expose the (001) plane and fixed on a copper plate with carbon tape. The sample was then introduced into an ultra-high vacuum chamber. Here, in addition to the conventional XAS/XMLD measurements, a novel "rotational" XMLD measurement was performed. All spectra were recorded at room temperature in the total electron yield mode.

Figure 2(a) shows the Ni L absorption edge XAS spectrum of a NiO crystal, measured with horizontal and vertical polarization with an incident angle of 80° from the (001) surface [see Fig. 1]. The XAS spectrum was normalized by the integrated intensity in the range 878-881 eV. The XMLD spectrum of the NiO crystal was obtained by taking the difference between the XAS spectra recorded with horizontal and vertical linear polarization [Fig. 2(b)]. Linear dichroism is clearly found. Focusing on the L2a and L2b peaks in the figure, we see that the L2a peak is enhanced by horizontal polarization and the L2b peak by vertical polarization. This contrasting response to light polarization gives rise to the XMLD signal plotted in Fig.

2(b). These results are consistent with previous L-absorption edge XMLD experiments on NiO [2] and suggest that the in-plane spin component is dominant on the cleaved NiO (001) surface.

After confirming the performance of the conventional method, we present the results of XMLD measurements while rotating the linear polarization angle. Here, we focus on the Ni L2 absorption edge peaks, L2a and L2b. The photon energy incident on these peaks was fixed, and the XAS intensity was detected while continuously changing the angle of linear polarization during the measurement. Figures 2(c) and (d) show the results. The intensity varies with a period of π, indicating a clear contrast in XMLD. The inversion of the order of the ID section (red and blue curves in the figure) also confirms that the signal is dichroic. Figures 2(c) and (d) also show that the dependence is opposite between L2a and L2b, as expected for the XMLD signal displayed in Fig. 2(b).

The advantage of this rotation method is that the linear dichroism signal is more reliable because the linear polarization angle dependence is tracked while the sample position is fixed. This method is useful for detecting the small electronic and magnetic anisotropies often found in quantum materials. Fixing the sample position also allows operando XMLD experiments, where sample size and rotational motion are severely restricted.

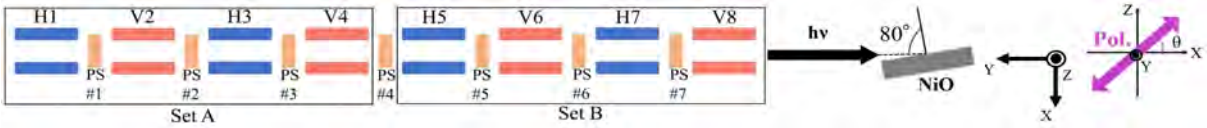

Fig. 1: A schematic of the segmented cross undulator and the measurement configuration. H and V denote IDs for horizontal and vertical polarization, respectively. Linearly polarized soft X rays travel along the Y axis and the polarization angle θ is varied within the X-Z plane.

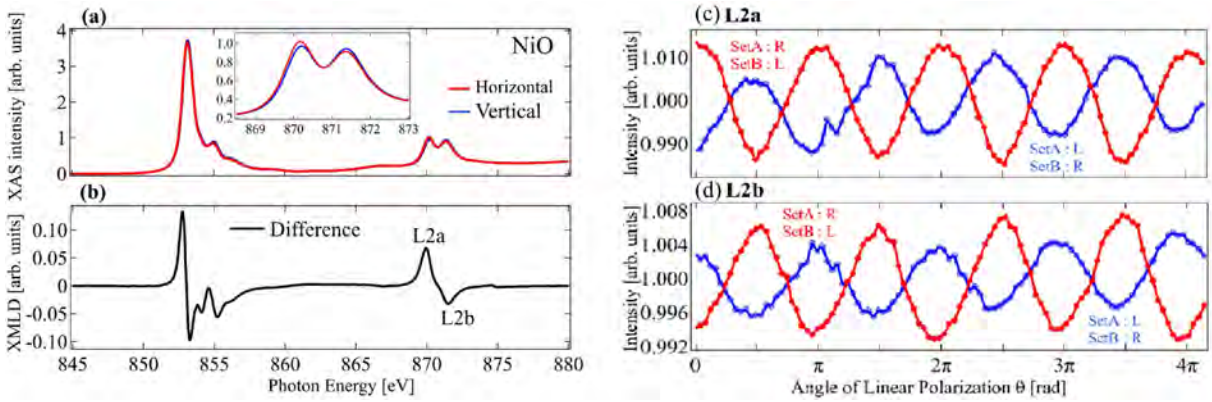

Fig. 2: Ni L-edge XMLD of NiO taken at an incident angle of 80 degree. (a) XAS measured with horizontal and vertical polarization. (b) XMLD obtained by taking the difference of two curves in (a). (c), (d) Rotational XMLD measured at L2a and L2b peaks [see (b)], respectively, plotted against linear polarization angle θ. For the red (blue) curve, undulator set A produces right (left) polarization while set B produces left (right) polarization.

REFERENCES

[1] S. Yamamoto et al., J. Synchrotron Rad. **21**, 352 (2014).
[2] G. van der Laan *et al*., Phys. Rev. B **83**, 064409 (2011).
[3] H. Ohldag *et al*., Phys. Rev. Lett. **86**, 2878 (2001).

DEVELOPMENT OF ANGLE-RESOLVED SOFT X-RAY EMISSION SPECTROSCOPY

Naoya Kurahashi[1], Jun Miyawaki[1], Kosuke Yamazoe[2] and Yoshihisa Harada[1]

[1]*Synchrotron Radiation Laboratory, The Institute for Solid State Physics, The University of Tokyo*

[2]*Japan Synchrotron Radiation Research Institute*

Soft X-ray emission spectroscopy is a powerful technique to observe the valence electronic state of occupied orbitals, as it involves emission of excess energy as light when a valence electron relaxes into a core hole generated by the soft X-ray excitation. The measurement under ambient pressure including wet condition is realized by using X-ray transmission windows such as silicon nitride. Photoelectron spectroscopy is another method for directly observing occupied electronic states, and it is possible that photoelectron spectroscopy and emission spectroscopy provide complementary information, as exemplified by the results of bulk water measurements [1]. While soft X-ray emission spectroscopy can approach samples in a variety of environments, it tends to have a broad natural width of the spectrum, due to the short lifetime of the core hole. Because of this, it may not be possible to completely separate the electronic states only by the emission energy but a method utilizing other physical parameters for assigning electronic states is required.

Since photoelectron spectroscopy for atoms and molecules has long been used to study photo-excitation dynamics, there has been a need for a method to understand the electronic excitation states. To solve this problem, a photoelectron velocity mapping method[2] has been developed that enables simultaneous observation of the kinetic energy and emission angle of photoelectrons. In the process of photoelectron emission, the orbital angular momentum of electrons changes by ±1 according to the law of conservation of angular momentum ($\Delta l = \pm 1$). For example, electrons from the *s*-orbital are emitted in the form of *p*-orbitals, while those in the *p*-orbital are emitted as a superposition of *s*- and *d*-orbitals. As a result, by measuring the kinetic energy and emission angle distributions of photoelectrons, information on the energy levels and angular momenta of the original orbitals can be obtained, which enables precise assignment of electron orbitals.

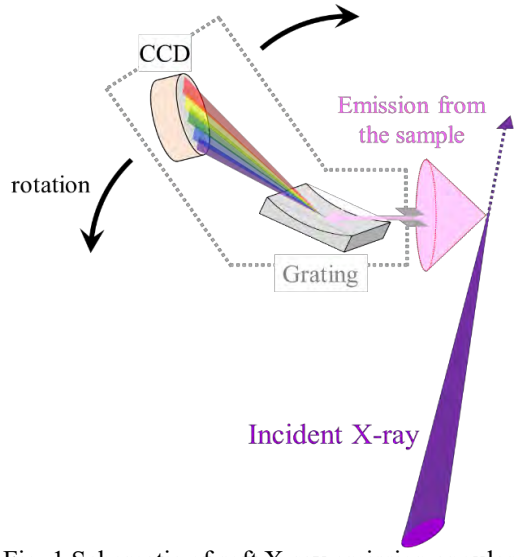

Fig. 1 Schematic of soft X-ray emission angular anisotropy measurement. The incident light and emission points were fixed and the spectrometer was rotated in the horizontal plane.

As in X-ray emission spectroscopy, $\Delta l = \pm 1$ should hold and the angular momentum change of the electron orbitals is expected to be emitted in the form of light. Therefore, the soft X-ray emission is expected to be anisotropic, reflecting the symmetry of the electron orbitals. Therefore, we planned to observe the angular anisotropy of soft X-ray emission from a gaseous sample.

In emission spectroscopy, a portion of the light emitted from a sample is cut off and dispersed by a spectrometer. In a soft X-ray emission angular anisotropy experiment, the angular anisotropy of soft X-ray emission from a sample can be observed by performing emission spectroscopy measurements with linearly polarized light incident on the sample and the entire grating and detector rotated around the sample (Fig. 1). By using a gas-phase sample, the angular emission anisotropy is considered to depend only on the angle between the

molecular axis and the electric field plane of light and the symmetry between the core-excited intermediate and final states of the molecule, making it easy to compare with theoretical calculations. Due to the trade-off between energy resolution and detection efficiency in emission spectroscopy, and the low efficiency of X-ray fluorescence for light elements, soft X-ray emission spectroscopy for gaseous samples has been considered difficult. To solve this problem, we have developed a method to increase the density of a target gaseous element at the sample position. In this method, X-ray is introduced very close to the sample introduction nozzle (within a few-μm) by devising the shape of the sample introduction nozzle, allowing emission measurement in a high-density region before the sample diffuses. This method achieves a signal intensity 100 times higher than that of conventional gas nozzles, while maintaining a high vacuum in the chamber by reducing the absolute amount of sample. We performed soft X-ray emission observation of oxygen gas and succeeded in the first soft X-ray emission angle anisotropy measurement of gaseous molecules (Fig. 2). The pressure in the vacuum chamber remained at around 10^{-4} Pa even though 100 kPa pure-oxygen gas was introduced, and no influence on the light source or other devices was observed.

When the excitation energy was 530.8 eV, which is the $1s$-σ_u to $2p$-$1\pi_g$* excitation ($^3\Sigma_g^- \rightarrow {}^3\Pi_u$), and the polarization was horizontal, the $^3\Sigma_g^-$ signal intensity was dependent on the angle of the spectrometer. The $^3\Sigma_g^-$ emission from $^3\Pi_u$ is stronger in the direction perpendicular to the polarization direction of the incident light. On the other hand, no clear angular anisotropy was observed for $^3\Pi_g$ emission; both $^3\Sigma_g^-$ and $^3\Pi_g$ emission angular anisotropies differed from theoretical predictions and from the results of photoelectron angular anisotropy. The presence of a relatively long-lived component in $^3\Sigma_g^-$ may have weakened the information on angular anisotropy due to molecular rotation[3]. The results of the present study were compared with the theoretical calculations.

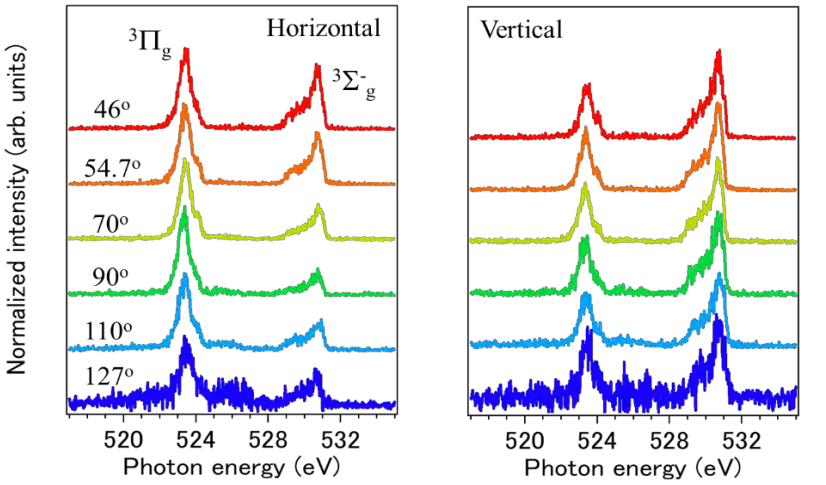

Fig. 2 Soft X-ray emission angle anisotropy measurements of oxygen excited at 530.8 eV. The angle in the figure indicates the angle between the optical axis of the incident light and the monochromator.

No angular anisotropy was observed in any of the peaks when the polarization was set to vertical. This indicates that the measurement system maintains cylindrical symmetry in vertical polarization. This means that the sample emission occurred at the center of rotation of the spectrometer.

With this research, we succeeded in a windowless experiment of soft X-ray emission spectroscopy, and also succeeded in measuring the soft X-ray emission angular anisotropy. We would like to compare our understanding of the measurement results with theoretical calculations.

REFERENCES

[1] T. Fransson *et al.*, *Chem. Rev.*, 116, 7551 (2016).
[2] T. Suzuki, *Annu. Rev. Phys. Chem.*, 57, 555 (2006).
[3] J.-E. Rubensson *et al.*, *J. Electron Spectros. Relat. Phenomena*, 185, 294 (2012).

CHARGE EXCITATION RESEARCH ON THE T* PHASE HOLE-DOPED CUPRATES BY RESONANT SOFT X-RAY SCATTERING

Xie PEIAO[1], Shinnosuke KITAYAMA[1], Takanori TANIGUCHI[1], Hisao KIUCHI[2], Kenji ISHII[3], and Masaki FUJITA[1]

[1] *Institute for Materials Research, Tohoku University, Sendai 980-8577, Japan*
[2] *Institute for Solid State Physics, University of Tokyo, Kashiwa 277-8581, Japan*
[3] *Synchrotron Radiation Research Center, National Institutes for Quantum and Radiological Science and Technology, Hyogo 679-5148, Japan*

Recently, the momentum-dependent charge excitations have been found to exist on the hole-doping $La_{2-x}(Br, Sr)_xCuO_4$ from the O *K*-edge resonant inelastic x-ray scattering (RIXS) experiment [1]. The results showed the outwardly dispersive mode which contains the same behaviors as the NCCO L_3-edge RIXS spectrum [2,3]. The authors ascribed it's come from the charge excitations. However, the existence of the dispersive mode originating from charge excitations in all cuprate families is still under debate [4,5]. In this experiment, we first performed the charge excitations study for another 214-type cuprate — the T* phase family, which contained CuO_5 pyramid coordination formed by alternate stacks of rock-salt layers (T phase) and fluorite layers (T' phase). The SC state of T* phase cuprates emerged after oxidation annealing (O-AN) under high pressure to repair the oxygen deficiency around the apical site. Due to such a unique crystal structure, this research may inspire us further understand the physical nature of charge excitations.

The measurement was performed on the beamline BL07LSU at SPring-8. The $SmLa_{0.75}Sr_{0.25}CuO_4$ (SLSCO) of the as-sintered (AS) samples were grown by the traveling solvent floating zone (TSFZ) method with 2.5 atoms of oxygen. The quality of the crystal was checked by the x-ray back-scattering Laue method. The representative Laue pattern taken with the x-ray beam parallel to [0, 0, 1] crystalline axis is shown in Fig. 1 (a). The oxygenized (O-AN) samples were prepared by annealing the AS samples in oxygen gas under ~ 46MPa at 500 °C for 80 h. Fig. 1 (b) shows the magnetic susceptibility of the O-AN sample. We tuned the incident photon energy for the RIXS measurements to the hole peak value at ~528.3eV by scanning the total fluorescence yield. In this measurement, we set the *c* axis of AS and O-AN samples kept parallel to the horizontal scattering plane. The samples were cleaved in the air just before the measurements.

Figures 2 (a) – (d) show the O *K*-edge RIXS spectra and image plot for both AS and O-AN samples with the whole $\boldsymbol{q}$ range in our measurement. We observed the RIXS signal (grey line) of T*-type cuprates and the oxidation annealing effect on the charge excitations for the first time. The signal was obtained by subtracting the elastic and fluorescence peak, and all the data were normalized by the integrated intensity of fluorescence at $\boldsymbol{q}$ = (0.1, 0) of the O-AN sample. Because it was difficult to fit the RIXS signal systematically, the spectral intensity over 90% of the maximum has been chosen as the peak's region. Notably, the elastic peak of O-AN samples contained an obvious additional peak at around 0.2 - 0.3 eV. We fitted only elastic peak by Gaussian function to extract such a peak. For

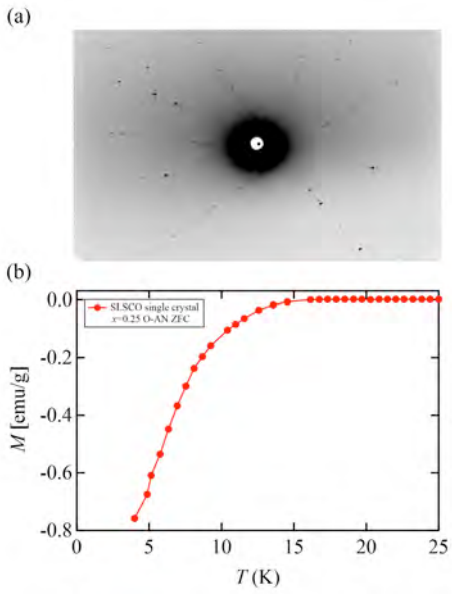

Fig. 1 (a) Laue pattern and (b)magnetic susceptibility of O-AN $SmLa_{0.75}Sr_{0.25}CuO_4$.

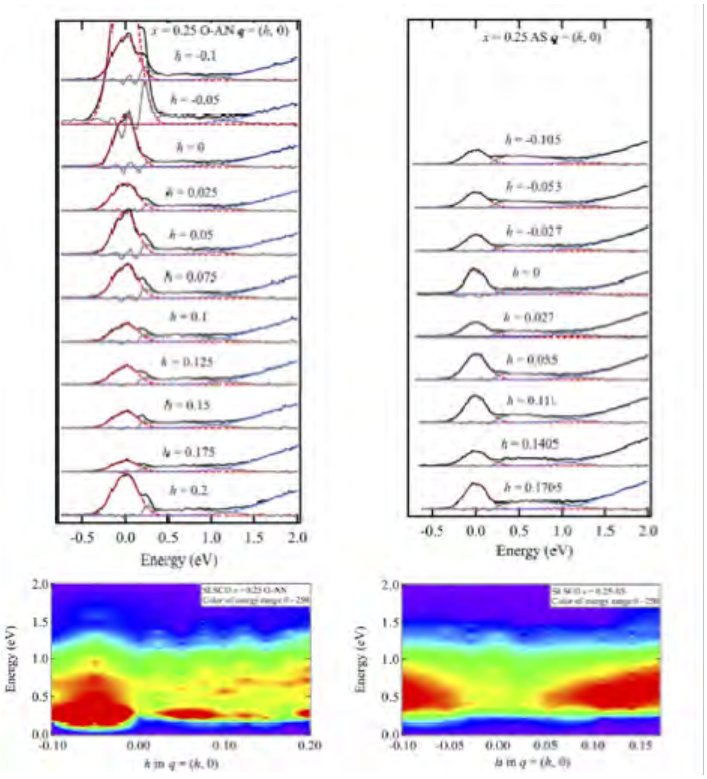

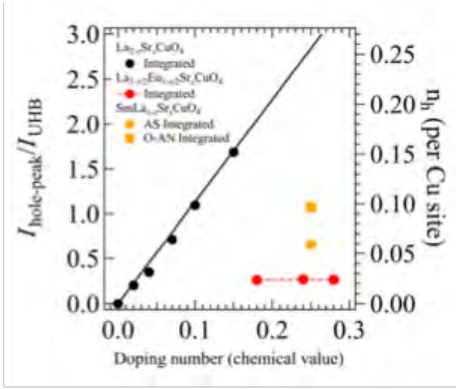

Fig 2. RIXS spectra and image plots of (a), (c) AS and (b), (d) O-AN $SmLa_{0.75}Sr_{0.25}CuO_4$. (e) Doping dependence of the ratio value from the integral intensity of hole and upper Hubbard band peaks, the LSCO results plotted in the black line as a reference.

both O-AN and AS samples, the RIXS signal was much weaker than the LSCO in the previous report with faintly momentum-dependent charge excitations. O-AN sample contained an additional peak near the elastic peak independent of ***q***, and the intensity of the elastic peak in the O-AN sample changed non-successive with the momentum. In contrast, the AS sample showed relatively higher intensity than the O-AN sample. Furthermore, by comparing the image plot results of AS and O-AN samples, the spectra weight of RIXS in AS sample is more concentrated.

In Fig. 2 (e), we plotted the ratio value of the integrated intensity of peaks corresponding to the hole-induced state and a hybridized state of the Cu upper Hubbard band with the O 2*p* states. Comparing them with the standard value of $La_{2-x}Sr_xCuO_4$ (LSCO) from the published report, it's clearly shown that the actual doping amount of strontium in both AS and O-AN samples is much lower than the chemometric value [6]. Meanwhile, the RIXS spectrum of $La_{2-x}(Sr, Ba)_xCuO_4$ in a lightly doped region showed a momentum-independent behavior with a relativity weaker signal than the higher doping region, which would be one of the explanations for our results. However, from the theoretical part, the effect of apical oxygen is strongly correlated with the hopping parameter *t*, which may play an important role but is not taken into account. For the next step, the doping dependence of RIXS for the T* phase cuprates is important [7].

REFERENCES

[1] K. Ishii, *et al.* Phys. Rev. B **96**, 115148 (2017).
[2] C. Jia, *et al.* Phys. Rev. X **6**, 021020 (2016).
[3] K. Tsutsui and T. Tohyama, Phys. Rev. B **94**, 085144 (2016).
[4] W. S. Lee, *et al.* Nature Phys. **10,** 883 (2014).
[5] A. Greco, *et al.* Phys. Rev. B **94**, 075139 (2016).
[6] C. T Chen, *et al.* Phys. Rev. Letter **66**, 104 (1991).
[7] Y. Ohta, *et al.* Phys. Rev. B **43**, 2968 (1991).

Co L_3-edge Soft X-ray Emission spectroscopy of $La_{0.6}Sr_{0.4}CoO_{3-\delta}$ for solid oxide fuel cells

Daisuke Asakura[1,2], Eiji Hosono[2,3], Tomohiro Ishiyama[1], Riyan Achmad Budiman[1], Haruo Kishimoto[3], Kosuke Yamazoe[4], Naoya Kurahashi[4], Ralph J. Ugalino[4], Hisao Kiuchi[4], and Yoshihisa Harada[2,4]

[1]*Research Institute for Energy Conservation, National Institute of Advanced Industrial Science and Technology (AIST)*

[2]*AIST-UTokyo Advanced Operando-Measurement Technology Open Innovation Laboratory, AIST*

[3]*Global Zero Emission Research Center, AIST*

[4]*Synchrotron Radiation Laboratory, The Institute for Solid State Physics, The University of Tokyo*

Solid oxide energy devices including oxide-based all-solid-state Li-ion battery (LIB) are characteristic of the stability compared to energy devices with liquid systems. For example, solid oxide fuel cell (SOFC) is a well-known solid oxide energy device. SOFC is a fuel cell working at a high temperature (around 800 °C) with oxygen ion conduction. Oxygen in the air is supplied to the cathode (air electrode) and converted to O^{2-} ion with electrons from the circuit. The O^{2-} ions are transferred through a solid-state electrolyte and reach at the anode (fuel electrode). In the anode, the O^{2-} ions react with H_2 and are converted to H_2O with generating electrons, resulting in electricity generation. This is the operating principle of SOFC.

For the cathode of SOFC, 3*d* transition-metal oxides with the Perovskite structure are widely used. $La_{1-x}Sr_xCoO_{3-\delta}$ (LSC) is one of the prototypical cathode materials for SOFC while LSC has also been studied in the research field of strongly correlated electron systems. To further enhance the performance of LSC as the SOFC cathode, the electronic structure analysis for the Co 3*d* and O 2*p* orbitals is particularly important to understand the redox reaction and O^{2-} ion conduction mechanisms. Here, we employ the Co *L*-edge X-ray absorption spectroscopy (XAS) and X-ray emission spectroscopy (XES) for LSC utilizing experiences for $LiCoO_2$ which is a Co-oxide cathode material for LIB.

We conducted the Co $L_{3,2}$-edge XAS and L_3-edge XES measurements for a bulk LSC ($La_{0.6}Sr_{0.4}CoO_{3-\delta}$, made in AIST) by using HORNET spectrometer at BL07LSU, SPring-8. For XAS, total-electron-yield (TEY) and partial-fluorescence-yield (PFY) detection modes were employed. The energy resolution for the XES measurement was set to 240 meV at 780 eV.

Figure 1 shows the Co $L_{3,2}$-edge TEY and PFY XAS spectra for the LSC. According to previous studies for $LaCoO_3$ and $LiCoO_2$,[1,2] the XAS line shape for the TEY spectrum is assigned to be mainly Co^{3+} state while the peaks for 777-779 eV suggests a small

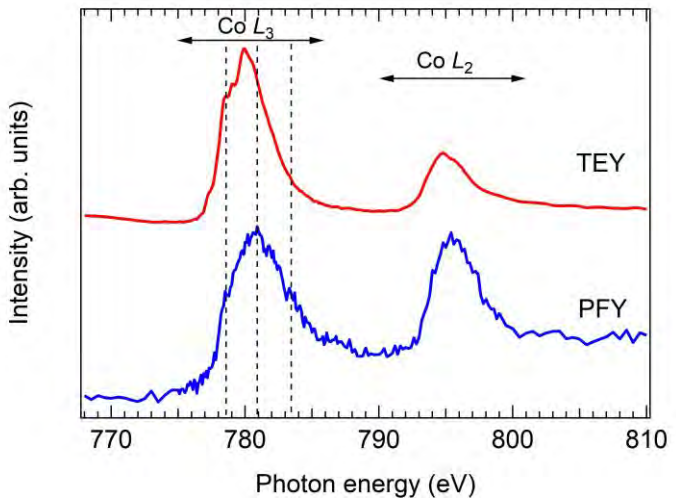

Fig. 1. Surface-sensitive TEY and bulk-sensitive PFY Co $L_{3,2}$-edge XAS spectra for $La_{0.6}Sr_{0.4}CoO_{3-\delta}$.

amount of Co^{2+} should coexist. For the PFY spectrum, the highest point of Co L_3 edge shifted by +1 eV and the structure around 783 eV was enhanced, indicating that the oxidation state of the bulk region is higher than that near the surface.[2] Most likely, the Sr content and/or oxygen defect contributing to hole doping on the Co cite should be suppressed near the surface. We selected three points characteristic of the Co L_3-edge PFY spectrum (the dotted lines in Fig. 1) as the excitation energies for XES.

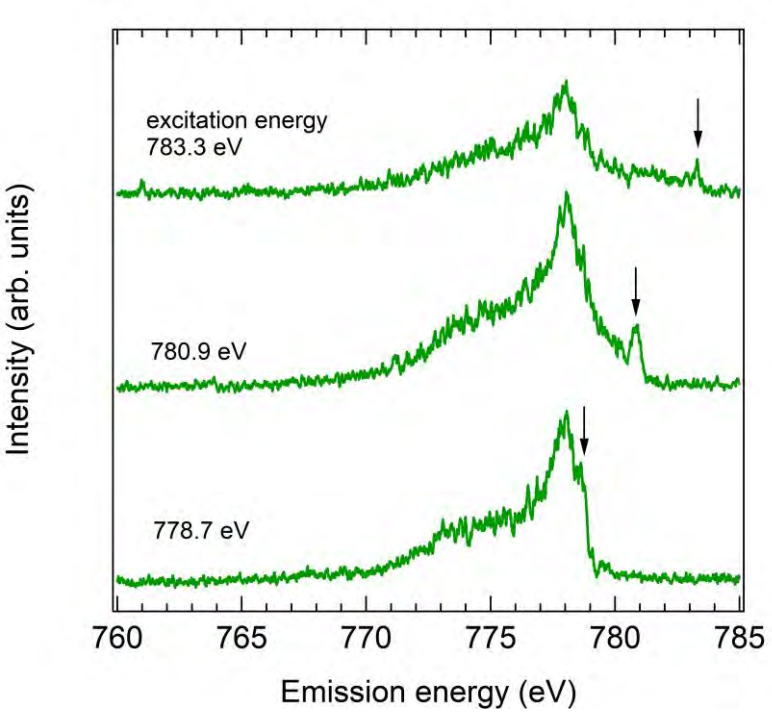

Fig. 2. Co L_3-edge XES spectra for $La_{0.6}Sr_{0.4}CoO_{3-\delta}$. The allows indicate the elastic scattering peaks.

The XES results are shown in Fig. 2. For the 780.9-eV excitation, the broad structure around 775 eV should be of charge-transfer excitation. The structures from 776 to 780 eV should be of *dd* excitation, while the strong peak at 778 eV is ascribed to the fluorescence peak because the peak position is independent of the excitation energy. On the other hand, for a previous study of $LaCoO_3$ thin film, the peak position of fluorescence is lower in emission energy scale.[1] This difference between the $LaCoO_3$ thin film and LSC should correspond to that the oxidation state of Co is higher observed from the PFY XAS result. Similar energy shift of the fluorescence depending on the oxidation state has been also reported for the Co L_3-edge XES for $LiNi_{0.65}Co_{0.25}Mn_{0.1}O_2$ (a cathode material for LIB).[3] Thus, the XES spectra for LSC should include the component of Co^{4+} state in addition to that of the Co^{3+} state. The XAS and XES spectra will be analyzed with multiplet calculation. The relation between the electronic structure and the performance as a cathode for SOFC will be further investigated. Also, we will try the *operando* measurement with developing an all-solid-state-type *operando* cell for SOFC.

REFERENCES

[1] Y. Yokoyama *et al*., Phys. Rev. Lett. **120**, 206402 (2018).

[2] For example, W.-S. Yoon *et al*., J. Phys. Chem. B **106**, 2526 (2002) and T. Mizokawa *et al*., Phys. Rev. Lett. **111**, 056404 (2013).

[3] H. M. Hollmark *et al*., J. Electrochem. Soc. **157**, A962 (2010).

POSSIBLE ANAPOLE ORDER IN THE ANTIFERROMAGNETIC PHASE OF MULTIFERROIC CUO

Ryusuke MISAWA[1], Keito ARAKAWA[1], Hiroki UEDA[2], Jun MIYAWAKI[3], Hisao KIUCHI[4], Yoshihisa HARADA[4], Yoshikazu TANAKA[5], and Tsuyoshi KIMURA[1]

[1]*Dept. of Adv. Mater. Sci., The University of Tokyo,* [2]*Paul Scherrer Institut,* [3]*National Institutes for Quantum and Radiological Science and Technology,* [4]*Synchrotron Radiation Laboratory, The Institute for Solid State Physics, The University of Tokyo,*[5]*RIKEN SPring-8 Center*

The orbital current is characterized by a time-odd polar vector that corresponds to an anapole or toroidal moment [1]. It is proposed as the order parameter in the pseudo-gap phase of high-T_c cuprate superconductors and in the hidden ordered phase in some 5*d* transition-metal systems such as $Sr_2(Ir,Rh)O_4$. Anapoles are formed by orbital currents between metal ions and ligands and between ligands as shown in Fig. 1. Symmetry breakings due to the orbital currents have been examined so far by several experimental techniques such as magneto-optical effects [2] and second harmonic generation [3]. Though some of the experimental results suggest the formation of anapole order, others do not support it [4]. In this study, we examined the presence of anapole order in antiferromagnetic CuO by using resonant x-ray diffraction (RXD) and resonant inelastic x-ray scattering (RIXS).

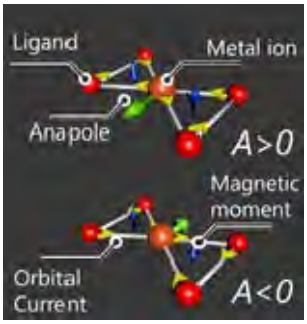

Fig.1. Schematic drawing of anapole moment induced by orbital currents.

CuO (space group: *C*2/*c*) exhibits successive magnetic transitions at T_{N1} =213 K and T_{N2} =230 K. At $T_{N1} < T < T_{N2}$, it shows an incommensurate (ICM) spiral magnetic order with the wavevector of $\mathbf{q}_{ICM}$ = (0.507, 0, -0.486). The spiral magnetic order induces spin-driven ferroelectricity [5]. The ferroelectricity disappears below T_{N1} where the magnetic structure transforms into a commensurate (CM) colinear antiferromagnetic one with the wavevector of $\mathbf{q}_{CM}$ = (0.5, 0, -0.5). Based on experimental results of circularly polarized resonant x-ray diffraction on CuO, the existence of anapole order induced by the orbital currents between copper and oxygen ions has been proposed in ref. [6]. However, some theoretical studies refute the interpretation [7], and no definitive conclusion has been reached on the proposed anapole-ordered state in CuO. The purpose of this study is to examine the anapole order and its domain state through scanning RXD and RIXS using circularly polarized x-rays.

We measured circularly polarized RXD and RIXS on a plate-shaped single crystal of CuO with the widest face parallel to the (10-1) plane. These measurements were carried out at BL07LSU, SPring-8. The incident x-ray energy was set near the Cu L_3 absorption edge. The incident x-ray beam was focused into ~34 μm (~5 μm) in the horizontal (vertical) direction at the sample surface position. RXD and RIXS at $\mathbf{q}_{ICM}$ were measured in the ICM phase while those at $\mathbf{q}_{CM}$ were obtained in the CM phase. The scattering geometry is illustrated in Fig. 2. The circular polarization dependence of these reflections and their spatial distributions were examined. We also examined the effect of electric fields on them. To apply the electric field, a pair of gold electrodes were deposited on the crystal surface (Fig. 2).

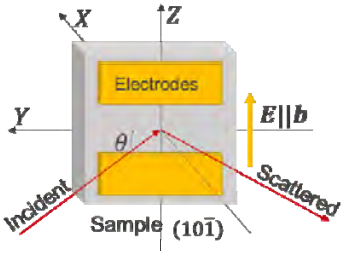

Fig. 2. Schematic drawing of scattering geometry.

The magnetic reflections in the two phases showed resonant enhancement at the energies around the Cu L_3 absorption edge (≈ 930 eV). In addition, they showed substantial circular polarization dependence. The circular polarization dependence in the ICM phase is explained by the spiral magnetic structure in the ICM phase while no confirmed mechanism

of that in the CM phase has not been provided yet. However, the electric field effect on the circular polarization dependence gives some clues for the understanding. Figure 3 shows the sample position dependence of the magnetic reflections in the ICM and the CM phases. For these measurements, the x-ray beam was scanned along the *Z* direction on the sample surface, and a positive or negative electric field was applied during the cooling of the sample and measurements. Figures 3(a) and 3(b) were obtained using the magnetic reflection with $\mathbf{q}_{ICM}$ at 220 K (ICM phase) while Figs. 3(c) and 3(d) were taken using that with $\mathbf{q}_{CM}$ at 200 K (CM phase). All the data shown in Fig. 3 were taken using incident x-rays with an energy of 929.7 eV. In all the measurements, a nearly uniform circular polarization difference over the sample area was observed. However, the sign of the circular polarization difference is reversed by a sign reversal of the electric field in both the phases. In addition, the sign of the circular polarization difference of the CM phase is the same as that of the ICM phase. At the present stage, we do not have a clear explanation for the origin of the circular polarization dependence in the CM phase. Clear supporting evidence of anapole order in the CM phase was not obtained. However, the similarity of the electric field effect observed in the ICM and the CM phases suggests that the order parameters of these two phases are correlated.

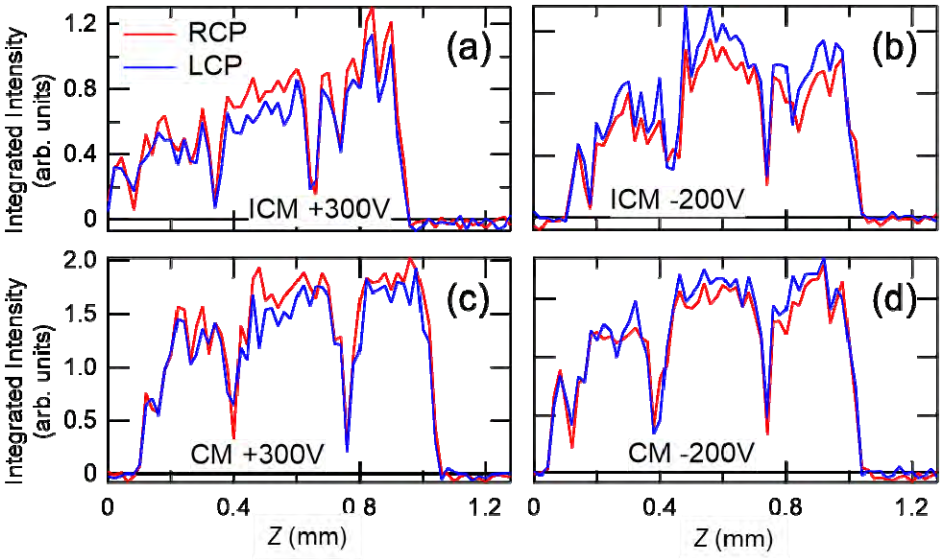

Fig. 3. Sample position dependence of magnetic reflection intensity measured using circularly polarized x-rays. (a,b) One dimensional scans of magnetic reflection at $\mathbf{q}_{ICM}$ = (0.507, 0, -0.486) in the ICM phase. (c,d) Those at $\mathbf{q}_{CM}$ = (0.5, 0, -0.5) in the CM phase. The scanning direction is along the *Z* direction. Measurements were carried out using right-circularly polarized (RCP) and left-circularly polarized (LCP) x-rays with energy corresponding to the Cu L_3 edge. The data of (a,c) were obtained in a positive electric field while those of (b,d) were taken in a negative electric field.

REFERENCES

[1] C. M. Varma, *Phys. Rev. B* **55**, 14554 (1997).

[2] Jing Xia, Elizabeth Schemm, G. Deutscher, S. A. Kivelson, D. A. Bonn, W. N. Hardy, R. Liang, W. Siemons, G. Koster, M. M. Fejer, and A. Kapitulnik, *Phys. Rev. Lett.* **100**, 127002 (2008).

[3] L. Zhao, D. H. Torchinsky, H. Chu, V. Ivanov, R. Lifshitz, R. Flint, T. Qi, G. Cao & D. Hsieh, *Nat. Phys.* **12**, 32 (2016).

[4] T. P. Croft, E. Blackburn, J. Kulda, Ruixing Liang, D. A. Bonn, W. N. Hardy, and S. M. Hayden, *Phys. Rev. B* **96**, 214504 (2017).

[5] T. Kimura, Y. Sekio, H. Nakamura, T. Siegrist, and A. P. Ramirez, *Nat. Mater.* **7**, 291-294 (2008).

[6] V. Scagnoli, U. Staub, Y. Bodenthin, R. A. de Souza, M. GarcíaFernández, M. Garganourakis, A. T. Boothroyd, D. Prabhakaran, and S. W. Lovesey, *Science* **332**, 696 (2011).

[7] Y. Joly, S. P. Collins, S. Grenier, H. C. N. Tolentino, and M. De Santis, *Phys. Rev. B* **86**, 220101(R) (2012).

ELECTRONIC STRUCTURE ANALYSIS OF OXYFLUORIDE CATHODE OF ALL-SOLID-STATE FLUORIDE BATTERY USING RESONANT INELASTIC X-RAY SCATTERING

Kentaro YAMAMOTO[1], Datong ZHANG[1], Hisao KIUCHI[2], Jun MIYAWAKI[2], Tomoki UCHIYAMA[1], Toshiki WATANABE[1], Tsuyoshi TAKAMI[1], Toshiyuki MATSUNAGA[1], Yoshihisa HARADA[2], Yoshiharu UCHIMOTO[1]

[1]*Graduate School of Human and Environmental Studies, Kyoto University*

[2]*Synchrotron Radiation Laboratory, The Institute for Solid State Physics, The University of Tokyo*

All-solid-state fluoride-ion battery is expected to be next-generation battery due to high electrochemical stability of F anion as charge carriers, as well as excellent theoretical energy densities which largely exceed those of conventional lithium-ion battery. Intercalation-type host materials, such as perovskite-, Ruddlesden−Popper-[1], etc., are particularly attractive owing to their high structural reversibility and F intercalation tolerance, compared with widely used conversion-type metal/metal fluoride systems (M/MF_x)[2]. It is important for topotactic materials to have anionic vacancies surrounding cationic coordination centers as F^- intercalation sites; therefore, those with low-coordination environment of cations can be promising host materials for F (de)intercalations. In this study, we introduced $Ca_{0.85}CuO_2$ as high-energy cathode material for all-solid-state fluoride-ion battery with an infinite-layer-related modulated chain structure. Slightly distorted square planar [CuO_4] provide sufficient rooms for F^- intercalation. Considering the large contributions to charge compensation from redox of oxygen in $Ca_{0.85}CuO_2$, the electronic structure of O was investigated by resonant inelastic X-ray scattering (RIXS) techniques.

$Ca_{0.85}CuO_2$ was synthesized via solid-state reactions. $CaCO_3$ and CuO were ground, pelletized and calcined at 800 °C for 20 hours with immediate regrinding afterward. The calcining and regrinding were repeated several times until single phase was acquired. Electrochemical properties were studied using bulk-type cells, with $La_{0.9}Ba_{0.1}F_{2.9}$ (LBF), $Ca_{0.85}CuO_2$/LBF/ vapor grown carbon fiber (VGCF) composite, and Pb/PbF_2/LBF/VGCF composite as solid electrolyte, cathode and anode, respectively. Ex situ Cu K-edge, Cu L2,3-edge and O K-edge XAS data were acquired in the partial fluorescence yield (PFY) mode at BL14B2 and BL27SU in SPring-8. Resonant inelastic X-ray scattering (RIXS) measurements were performed at BL07LSU in SPring-8 using a grazing flat-field type high resolution soft X-ray emission spectrometer. The measurements were conducted under vacuum and the samples were transferred from an Ar-filled glove box without exposure to air.

The $Ca_{0.85}CuO_2$ cathode showed high capacity of 890 and 630 mAh g^{-1} in initial charging and discharging in the cut-off range of -1.5 to 3.0 V, respectively, corresponding to approx. 4.3 and 3.1 F^- intercalation/deintercalation (Figure 1). A large irreversible capacity in initial discharging might be related to the loss of oxygen or irreversibility of oxygen redox. After controlling the oxidation state of oxygen by cut the initial capacity to that of 3.0 F intercalation, the initial coulombic efficiency was greatly enhanced. According to XAS results, in initial charging process, oxygen redox is the major contributor to charge compensation. In initial discharging, both Cu and O were reduced; the uncomplete reduction of O species was highly possible to be the origin of low coulombic efficiency of initial cycle. In RIXS results of charged $Ca_{0.85}CuO_2F_{3.0}$ sample, the peaks at the emission energy of 523.5 eV with an incident photon energy of 530.9 eV revealed the generation of O-O bond. This was also supported by the vibrations at 529 to 531 eV (energy loss of -2.0 to 0 eV), as well as the corresponding frequency of the first vibrational level (0.2 eV, approx. 1600 cm^{-1})[3]. In addition, it is also highly possible that Cu^{2+} in pristine-state $Ca_{0.85}CuO_2$ could be further oxidized to

higher valency upon charging since the number of intercalated F anions exceeds the capability of oxygen redox, which requires more decisive evidence.

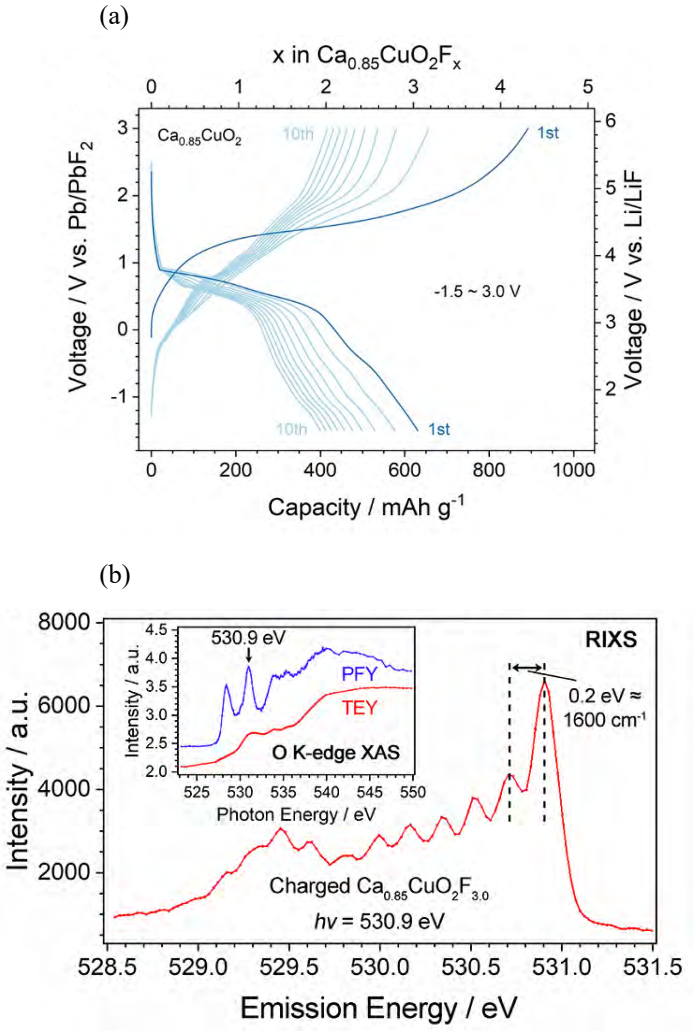

Fig. 1 (a) Charge-discharge profile of $Ca_{0.85}CuO_2$ cathode material with various cut-off conditions. (b) O K-edge XAS (inset) and corresponding RIXS results of charged $Ca_{0.85}CuO_2F_{3.0}$ sample.

REFERENCES

[1] M. A. Nowroozi, K. Wissel, J. Rohrer, A. R. Munnangi, and O. Clemens, *Chem. Mater.* 2017, **29**, 3441–3453.

[2] M. Anji Reddy and M. Fichtner, *J. Mater. Chem.* 2011, **21**, 17059–17062.

[3] R. A. House, U. Maitra, M. A. Pérez-Osorio, J. G. Lozano, L. Jin, J. W. Somerville, L. C. Duda, A. Nag, A. Walters, K.-J. Zhou, M. R. Roberts, and P. G. Bruce, *Nature* 2020, 577, 502–508.

OPERANDO AMBIENT PRESSURE PHOTOELECTRON SPECTROSCOPY OF CHEMICAL REACTION ON THE FUNCTIONALIZED BASAL AND EDGE SURFACES OF MoS_2

F. OZAKI, Y. CHOI, H. Li, Y. SAWAGUCHI, S. TANAKA, K. MUKAI, M. HORIO, I. MATSUDA and J. YOSHINOBU

The Institute for Solid State Physics, The University of Tokyo

Introduction

Molybdenum disulfide (MoS_2) is a layered substance that exists as a natural mineral (Fig. 1), and recently it is expected to be used for various applications such as field-effect transistors and photoelectric devices due to its unique physical properties [1]. In addition, it has been used as a catalyst for a long time. For example, Co-MoS_2 has been used industrially as a hydrodesulfurization catalyst to remove sulfur from oil [2]. Thus, the MoS_2 surface is a various catalytic reaction field involving hydrogen, and it is important to understand the interactions between the hydrogen molecules and MoS_2 surface.

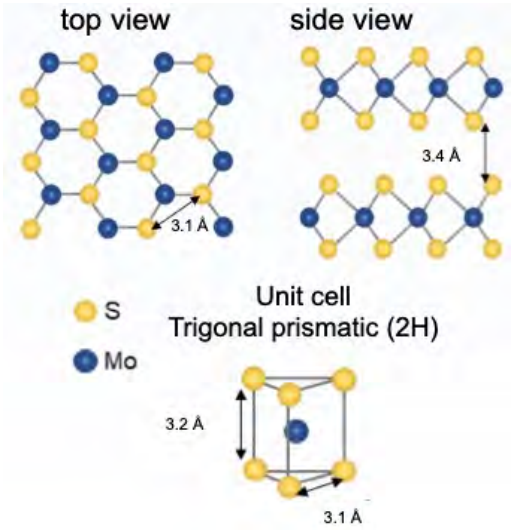

Figure 1 Structural model of MoS_2

It is known that the exfoliated MoS_2 (0001) basal surface is inert to the dissociation of molecular hydrogen, and the active site as a catalyst is mainly the edge of MoS_2. Tanaka and Okuhara have reported that the edge site plays a vital role, by comparing the catalytic activity of an un-cut MoS_2 with that of a MoS_2 cut by a pair of scissors to increase the edge area [3]. So far, the edge sites have only been studied by microscopic observation using scanning tunnelling microscopy and theoretical first-principles calculations due to their small scale and the difficulty of preparing a defined surface [4,5]. Therefore, it is a challenging issue to observe the chemical and electronic states of edge sites. In particular, the mechanisms of these reactions at the edge surfaces have not been elucidated yet. Therefore, we have conducted experimental observation of the chemical and electronic states of the edge surface using an ambient pressure photoelectron spectroscopy (AP-XPS).

Experimental

In this study, we prepared the edge surfaces of MoS_2 which were sharply cut perpendicular to the MoS_2 basal plane by ultrashort laser pulse processing at Kobayashi Laboratory in LASOR of The Institute for Solid States Physics (ISSP). In the case of mechanical cutting, possible metal contaminations from a scissors and edge-sagging by scission are inevitable. Laser processing does not cause edge-sagging and produces a fine edge surface (Figure 2). The spot size of SPring-8 BL07LSU is about 50 × 10 μm², and thus the edge can be selectively illuminated by synchrotron radiation. The incident photon energy was 655 eV and all measurements were carried out at room temperature. The MoS_2 single crystals were heated in ultra-high vacuum (UHV) to remove impurities, and the clean edge surfaces were observed by

XPS at SPring-8 BL07LSU. AP-XPS measurements were performed in hydrogen gas in order to investigate the reactivity of the edge surface with hydrogen molecules.

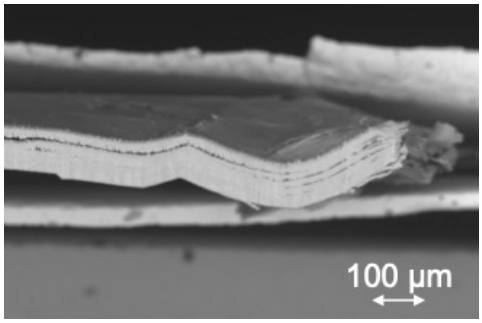

Figure 2 A secondary electron microscopy image of the MoS_2 edge prepared by ultrashort laser pulse processing

Results and discussion

The edge surface of MoS_2 was observed by XPS in UHV in order to investigate the changes caused by heating treatment. Figure 3 shows a series of Mo 3d XPS spectra in UHV. The Mo 3d spectrum of an "As installed" sample (Figure 3: blue) shows small oxidized components at ~230.9 and ~234.0 eV on the high binding energy side of the main Mo $3d_{5/2}$ and $3d_{3/2}$ peaks, respectively. After annealing at 700 K for 30 min, the oxidized components decreased in intensity. After further annealing at 700-800 K for 220 min, a shoulder appeared at ~228.3 eV. This shoulder component may be assigned to Mo^{2+} indicating a less coordinated state (missing S) than Mo^{4+} in the bulk MoS_2.

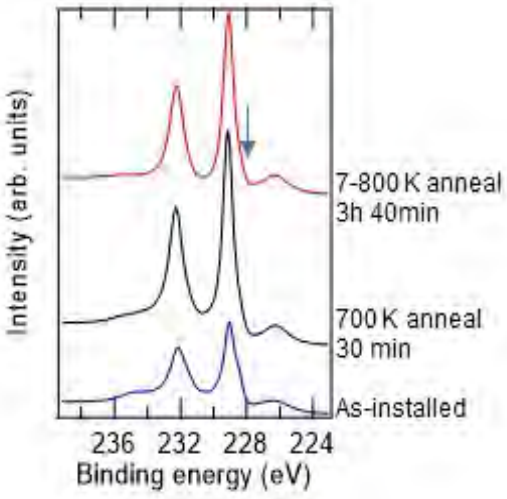

Figure 3 A series of Mo 3d XPS spectra of the MoS_2 edge surface in UHV.

The annealed sample was then transferred and installed at an AP-cell to investigate the reaction between the unsaturated Mo sites and hydrogen gas. The shoulder peak of Mo 3d XPS that appeared after the heat treatment decreased with the introduction of hydrogen (not shown here). This may be due to the dissociative adsorption of hydrogen at the less-coordinated Mo sites at the edge. The details of the present study will be reported elsewhere.

In this study, we have succeeded in directly measuring the electronic state of the coordinatively unsaturated Mo sites on the edge surface which was prepared by ultrashort pulse laser processing. AP-XPS results have shown that these sites are involved in the adsorption.

ACKNOWLEDGMENTS

We thank Dr. S. Tani (Kobayashi laboratory in LASOR, ISSP) for preparing the edge surface of MoS_2 by ultrashort pulse laser processing. The AP-XPS measurements using synchrotron radiation were performed at SPring-8 BL07LSU as joint research between the Synchrotron Radiation Research Organization and The Institute for Solid State Physics, The University of Tokyo (Proposal No. 2021B7432).

REFERENCES

[1] M. Chhowalla *et al*., Nat. Chem. **5**, 263-275 (2013).
[2] Y. Okamoto, Catal. Today **132**, 9 (2008).
[3] K.-I. Tanaka, T. Okuhara, J. Catal. **78**, 155-164 (1982).
[4] F. Besenbacher, J.V. Lauritsen, J. Catal. **403**, 4-15 (2021).
[5] M. Sun *et al*., J. Catal. **233**, 411-421 (2005).

ELECTRONIC STATE ANALYSIS OF EARTH-ABUNDANT FE–AL–SI THERMOELECTRIC (FAST) MATERIALS USING SCANNING PHOTOELECTRON MICROSCOPY

Yoshiki TAKAGIWA[1], Shunsuke TSUDA[1], Naoka NAGAMURA[1,2], Asako YOSHINARI[1,3], Shingo TAKEZAWA[1,3], Kenta OISHI[1,2,3], Kentaro FUKU[4], Wenxiong ZHANG[5]

[1]*National Institute for Materials Science (NIMS), Tsukuba, Ibaraki, Japan.*
[2]*PRESTO, Japan Science and Technology Agency, Honcho, Saitama, Japan.*
[3]*Tokyo University of Science, Katsushika, Tokyo, Japan*
[4]*Tohoku University, Sendai, Miyagi, Japan*
[5]*The University of Tokyo, Kashiwa, Chiba, Japan*

To develop new thermoelectric materials that are non-toxic and low-cost with sufficient power output for autonomous power supplies to drive sensor devices, in particular, at a low-temperature region below 400 K, we performed materials screening of ternary Fe-Al-Si system using first-principles band structure calculations [1,2]. We found that the ternary τ_1-$Fe_3Al_2Si_3$ phase forms a narrow bandgap of ~0.2 eV near the Fermi level and has shown potential as a novel thermoelectric material (FAST materials: **Fe**-**Al**-**Si** **T**hermoelectric Materials). We have demonstrated that the Al/Si ratio fine-tuning could control its conduction type and enhance the power factor without chemical substitutions [2]. Relatively large power factors were obtained for both p- and n-type thermoelectric materials below 400 K, which possessed high oxidation resistance and excellent mechanical properties [3]. Recently, we enhanced the power factor at mid-temperatures using machine-learning-assisted synthesis and evaluation [4]. We have established a mass production process for FAST materials and succeeded in the bonding technology to build a small-sized and highly integrated thermoelectric power generation module: the operation of temperature/humidity sensors and wireless transmission was performed [5]. Furthermore, we have succeeded in a synthesis of composition graded samples to find an optimized composition using a bulk combinatorial method with diffusion couple and mapping measurements [6]. Both theoretical [7,8] and experimental works [6,9] are essential to enhancing the thermoelectric properties. The remaining issue is to investigate the electronic structure experimentally and obtain the additional route for better thermoelectric performance.

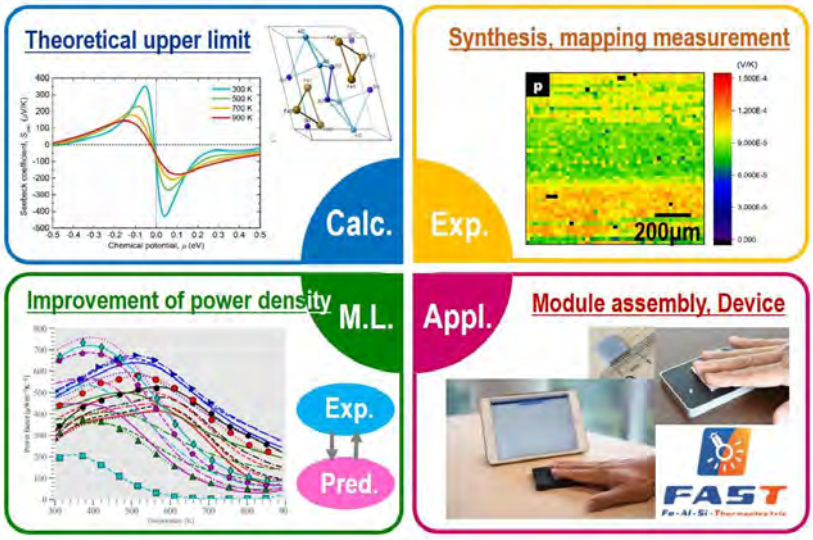

Fig. 1 Research and development of FAST materials using experiments, theoretical calculation, machine learning, and module development.

In this experiment, based on the FAST material of τ_1-$Fe_3Al_2Si_3$, (1) bulk samples of n-type and p-type semiconducting FAST materials with high thermoelectric properties and (2) composition gradient samples were prepared. The core level spectra (Fe 2p, Al 2p, Si 2p, C 1s, O 1s) and valence spectra were measured in each sample. At first, a sample was prepared, as shown in Fig. 2(a). Since severe surface oxidation and carrier charging were observed, the bulk sample was fixed with silver paste, and gold was deposited, as shown in Fig. 2(b). And then made it break in a vacuum.

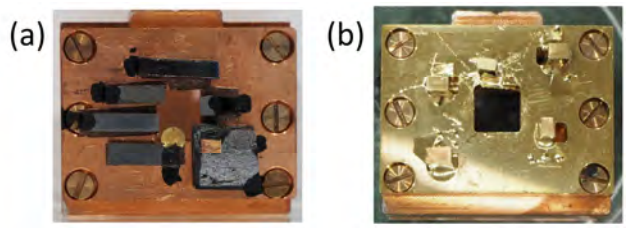

Fig. 2 Photos of sample holders.

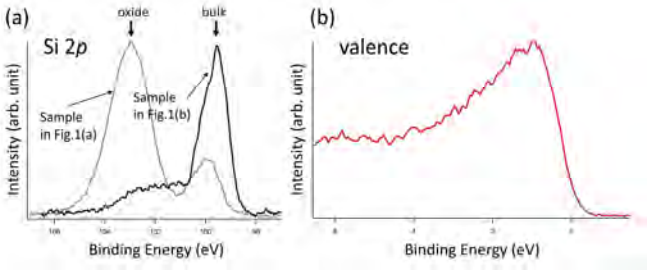

Fig. 3 (a) Si 2p core level spectra (b) valence spectrum.

The beamline used BL07LSU, which has high energy resolution in the soft X-ray region, and the device used a multi-dimensional operando photoelectron spectroscopy named "operando 3D nano-ESCA", which has a high spatial resolution (~ 70 nm). For the single composition bulk samples of FAST material, the spectrum derived from the oxide is significantly reduced in the spectrum measured by the sample holder of Fig. 1(b), as compared with the spectrum measured by the sample holder of Fig. 1(a). It was found that a spectrum derived from a bulk sample excluding the influence of surface oxidation was successfully obtained, as shown in Fig. 3(a). For the composition graded sample, the core level spectrum derived from the dopant could not be obtained with sufficient intensity; therefore, the sample preparation and measurement sample were considered major issues for the next beam time.

The valence spectrum is also measured, and the valence band maximum in each sample is specified from the rising edge, as shown in Fig. 3(b). Based on the results obtained this time, we will acquire data to quantitatively evaluate the difference in thermoelectric characteristics/transport characteristics and the core level spectrum/valence spectrum of FAST material samples at the next beam time.

REFERENCES

[1] Y. Takagiwa, Y. Isoda, M. Goto, and Y. Shinohara, J. Therm. Anal. Calorim. **131**, 281 (2018).
[2] Y. Takagiwa, Y. Isoda, M. Goto, and Y. Shinohara, J. Phys. Chem. Solids **118**, 95 (2018).
[3] Y. Takagiwa and Y. Shinohara, Scripta Mater. **172**, 98 (2019).
[4] Z. Hou, Y. Takagiwa, Y. Shinohara, Y. Xu, and K. Tsuda, ACS Appl. Mater. Interfaces **11**, 11545 (2019).
[5] Y. Takagiwa, T. Ikeda, and H. Kojima, ACS Appl. Mater. Interfaces **12**, 48804 (2020).
[6] Y. Takagiwa, Z. Hou, K. Tsuda, T. Ikeda, and H. Kojima, ACS Appl. Mater. Interfaces **13**, 53346 (2021).
[7] Z. Hou, Y. Takagiwa, Y. Shinohara, Y. Xu, and K. Tsuda, J. Phys.: Condens. Matter **33**, 195501 (2021).
[8] N. Sato and Y. Takagiwa, crystals **11**, 388 (2021).
[9] A. K. Srinithi, H. Sepehri-Amin, Y. Takagiwa, and K. Hono, J. Alloys Compds. **903**, 163835 (2022).

ANALYSIS OF WATER STRUCTURE OF THERMORESPONSIVE POLYMER MODIFIED INTERFACE

Kenichi NAGASE[1], Naoya KURAHASHI[2], Hisao KIUCHI[2], Yoshihisa HARADA[2]

[1]*Faculty of Pharmacy, Keio University*

[2]*Synchrotron Radiation Laboratory, The Institute for Solid State Physics, The University of Tokyo*

Introduction

Thermoresponsive polymer, poly(*N*-isopropylacrylamide)(PNIPAAm), exhibits temperature-responsive hydration and dehydration across lower critical solution temperature (LCST) of 32°C [1]. Using the property, PNIPAAm have been utilized various types of biomedical applications, such as drug delivery systems, bioseparation materials, and cell culture substrates [2,3]. However, the detailed investigation of the hydration property of PNIPAAm on substrate were not investigated, although the PNIPAAm hydration/dehydration in solution state was already clarified. In this study, we investigate the water structure in the modified PNIPAAm on substrate using high-resolution soft X-ray emission spectroscopy (XES).

Experiments

a) Sample preparation

PNIPAAm was synthesized by activator regenerated by electron transfer atom transfer radical polymerization (ARGET-ATRP) [4]. NIPAAm was dissolved in 2-propanol and water mixed solvent. Then, ATRP catalyst, $CuCl_2$, tris[2-(dimethylamino)ethyl]amine, and L-ascorbic acid, were added in the solution. ARGET-ATRP of NIPAAm was performed at 25°C for 16 h. After the polymerization, the prepared PNIPAAm was purified by dialysis and freeze drying. The prepared PNIPAAm was dissolved into methanol, and the PNIPAAm solution was casted to Au-coated SiC membrane. The methanol in casted solution was evaporated in a drying oven.

b) Soft X-ray emission spectroscopy (XES) measurement

Soft XES measurement of PNIPAAm cast film was performed by using ultra-high resolution soft X-ray emission spectrometer HORNET [5] installed at the SPring-8 BL07LSU. Water vapor was supplied by steam-generation equipment, and nitrogen was used as the carrier gas. Ultrapure water was used as the water source. Moisture was passed over the PNIPAAm casted film and then drained from the outlet port. Relative humidity was ranged from 0%-100%. Temperature was set at 20°C and 40°C.

Results

The water content of the PNIPAAm modified cast film was estimated at various relative humidity (Figure 1). Water content λ (water molecule/oxygen atom) increased with increasing the relative humidity, because the adsorbed water on PNIPAAm increased with relative humidity. Higher water content of the PNIPAAm was observed at 20°C compared to that of 40°C, because of the temperature-dependent hydration of PNIPAAm. The XES spectra at 20°C and 40°C were observed (Figure 2). Higher peak intensity was observed at 20°C compared to that at 40°C. The result indicates that the adsorption of water molecules to carbonyl group of PNIPAAm is enhanced at 20°C compared to that at 40°C, which is attributed to the temperature-dependent hydration of casted PNIPAAm on the substrate.

The XES measurement can observe the temperature-dependent adsorption of water molecules onto the carbonyl group of the modified PNIPAAm on the substrate. The obtained results can be utilized for the design of the PNIPAAm modified substrate.

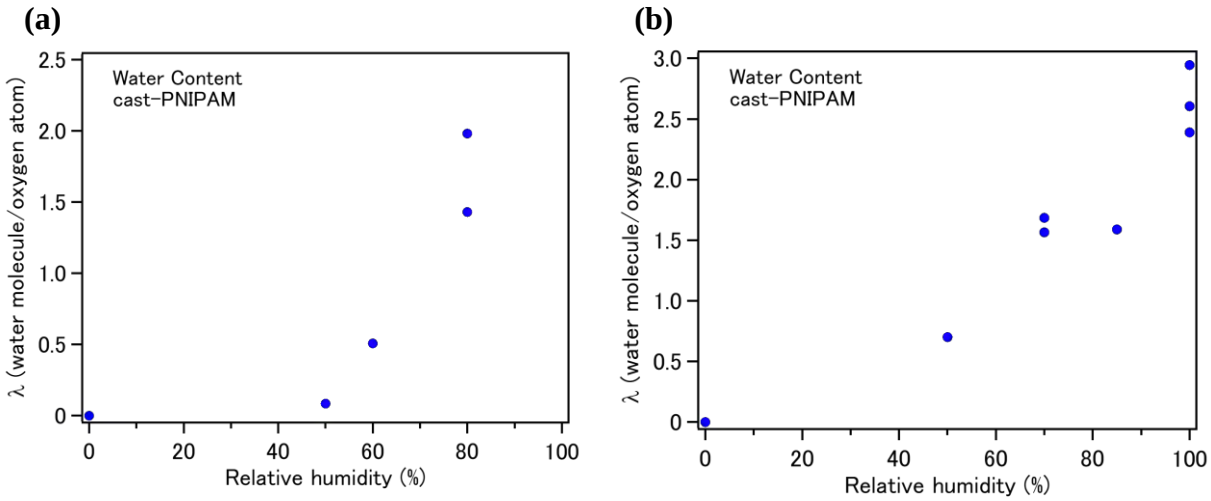

Fig.1 Water content (water molecule/oxygen atom) in PNIPAAm cast film at various relative humidity (a) at 20°C and (b) at 40°C.

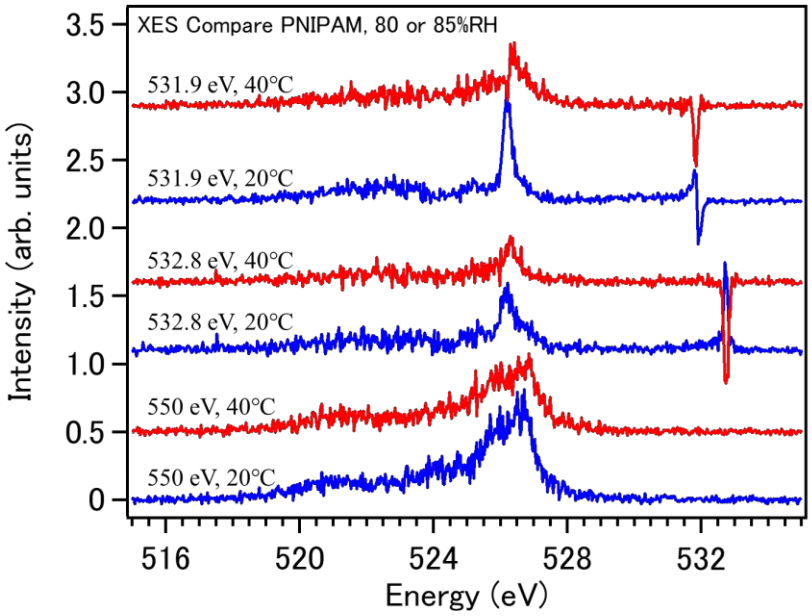

Fig.2 XES spectra of PNIPAAm cast film at 20°C and 40°C.

REFERENCES

[1] Heskins, M., Guillet, J. E., *J. Macromol. Sci. A* 2: 1441-1455, (1968)
[2] Nagase, K., Yamato, M., Kanazawa, H., Okano, T., *Biomaterials* 153: 27-48, (2018)
[3] Nagase, K., *Advances in Colloid and Interface Science* 295: 102487, (2021)
[4] Nagase, K., Shimura, M., Shimane, R., Hanaya, K., Yamada, S., Akimoto, A. M., Sugai, T., Kanazawa, H., *Biomaterials Science* 9(3): 663-674, (2021)
[5] Yamazoe, K., Higaki, Y., Inutsuka, Y., Miyawaki, J., Cui, Y.-T., Takahara, A., Harada, Y., *Langmuir* 33(16): 3954-3959, (2017)

RESONANT INELASTIC X-RAY SCATTERING SPECTROSCOPY OF CU-PROTEINS

Kentaro FUJII[1,2], Jun MIYAWAKI[2], Naoya KURAHASHI[3], Hisao, KIUCHI[3], Yoshihisa HARADA[3], Motoyasu ADACHI[1], Akinari YOKOYA[1]

[1]*Institute for Quantum Life Science, National Institutes for Quantum Science and Technology*

[2]*Advanced Synchrotron Radiation Centre, National Institutes for Quantum Science and Technology*

[3]*Synchrotron Radiation Laboratory, The Institute for Solid State Physics, The University of Tokyo*

Amicyanine and Azurin are classified as Class I TICu protein amicyanine, whose axial ligand is the sulfur atom of methionine. Both protein molecules share the asymmetric structure of four amino acids, Met, Cys, and two His, as the ligand for the copper atom (Fig. 1). Azurin contains an additional second axial ligand in addition to methionine in one axial position, as seen in the difference in distance to the oxygen atom. Crystallographic analysis has revealed that this asymmetry differs by a few percent between azurin and amicyanine[1]. Their redox potentials differ by about 30 mV at pH 8.0. In addition, both amino acid mutations have been introduced by genetic recombination technology, and significant redox potential changes of 500 mV or more have been observed when amino acid substitutions are introduced directly or indirectly at the copper atom. Especially, the changes of nearly 100 mV have been reported even at positions more than 10 Å from the copper atom. In order to reveal these phenomena, we examined the resonant inelastic soft X-ray scattering (RIXS) measurement of these solutions.

Both proteins were prepared as recombinant proteins expressed in E. coli using BL21 (DE3) and pET24a vector. The samples were purified with Ni-sepharose and ion-exchange columns. The ion-exchange columns used were HiTrap Q XL columns for amicyanine and HiTrap SP XL columns for azurin. The final solutions (~ 3mM) were

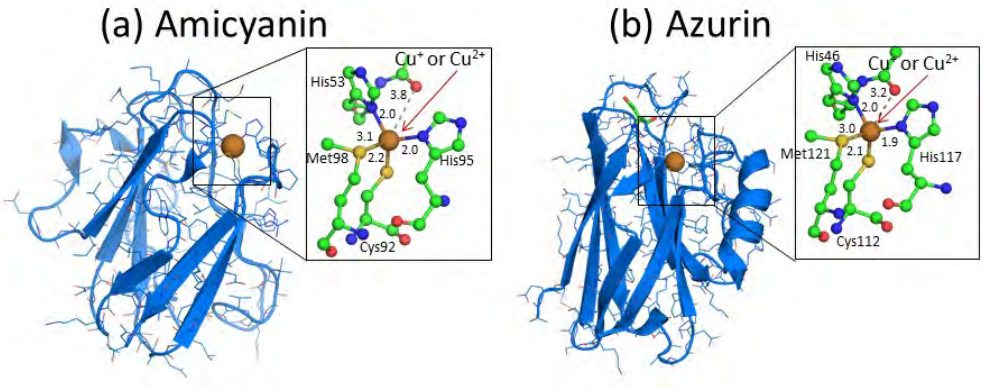

FIG 1 Molecular picture of (a) amicyanin and (b) azurin. The structures around Cu-atom are superimposed. Cu-atom is surrounded by Met, Cys and two His.

obtained by dialyzing in 20 mM Tris-HCl buffer (pH 8.0). The measurement the protein solutions was performed using a solution cell under ambient pressure by circulating the sample solution. To avoid oxidation of the sample, the circulated solutions were bubbled with nitrogen gas during the measurement.

Soft X-ray emission spectra around Cu-Ledge and resonant inelastic scattering emission spectra after Cu-L pre-edge resonance excitation (931eV excitation) were shown in Figure 2 and Figure 3, respectively. These spectra were obtained using a high-resolution soft X-ray emission spectrometer HORNET[2] installed at the end of the BL07LSU of SPring-8. The apparent peak structures of each spectrum were observed. In order to assign these peak structures, we are currently performing density functional theory simulations using a model molecule that imitates the coordination of amino acids around Cu. N.J. Fowler et al., predicted reduction potentials for several Cu proteins containing mutants using DFT calculation. In the future, we plan to perform RIXS spectroscopy on mutants with different amino acid residues surrounding Cu or different pH to obtain information on the correlation between the structure and electronic properties around Cu. This information regarding copper proteins has useful for general use in biotechnology, such as enzyme-catalyzed fuel cells or valorization of lignocellulosic biomass.

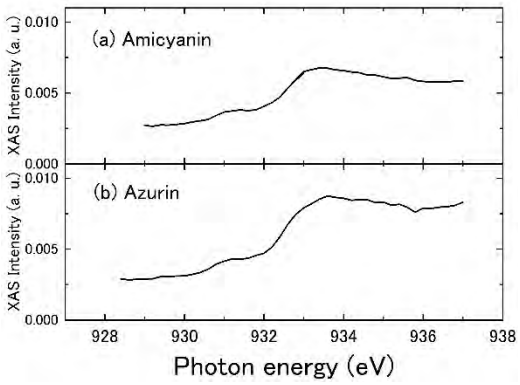

FIG 2 Cu *L*-edge XAS of (a) amicyanin and (b) azurin with 20mM Tris-HCl buffer solutions (~3mM).

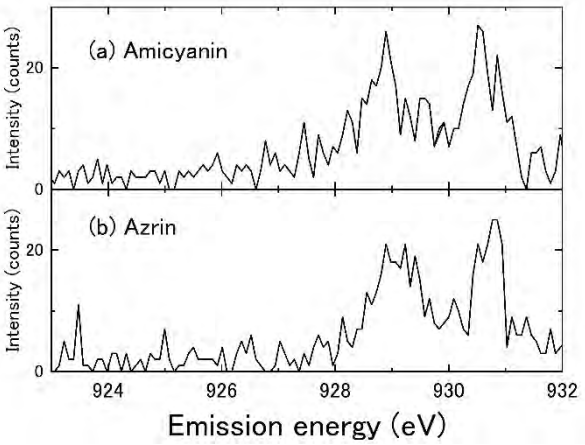

FIG 3 Cu *L*-edge RIXS spectra of (a) amicyanin and (b) azurin with 20mM Tris-HCl buffer solutions (~3mM).

REFFERENCES

[1] N.J. Fowler, C.F. Blanford, J. Warwicker, S.P. de Visser, Chem. Eur. J. 12 (2017) 15436-15445.

[2] Y. Harada et al., Rev. Sci. Instrum. 83 (2012) 013116.

STUDY ON THE HELICAL SPIN TEXTURE OF TOPOLOGICAL SURFACE STATE IN SUPERCONDUCTOR 2M-WS_2

Soonsang Huh[1], Soohyun Cho[2], Hua Bai[3], Yuqiang Fang[2], Fuqiang Huang[2], Yuto Fukushima[1], Ayumi Harasawa[1], Yunhao Lu[3,], Gang Mu[2] and Dawei Shen[2,4] and Takeshi Kondo[1,5]

1. Institute for Solid State Physics, University of Tokyo, Kashiwa 277-8581, Japan

2. Center for Excellence in Superconducting Electronics, State Key Laboratory of Functional Materials for Informatics, Shanghai Institute of Microsystem and Information Technology, Chinese Academy of Sciences, Shanghai 200050, China

3. Zhejiang Province Key Laboratory of Quantum Technology and Device, Department of Physics, Zhejiang University, Hangzhou 310027, China

4. Center of Materials Science and Optoelectronics Engineering, University of Chinese Academy of Sciences, Beijing 100049, China

5. Trans-scale Quantum Science Institute, University of Tokyo, Tokyo 113-0033, Japan.

Layered transition metal dichalcogenides (TMDs) of MX_2 (M = Mo, W; X = S, Se, Te) have been studied intensively because of a great interest in both fundamental and applied research. Among the stable phases of TMDs, Monolayer 1T′-MX_2 (M = Mo, W; X = S, Se, Te) were suggested as a promising candidate to realize quantum spin Hall (QSH) effect in strictly two-dimensional systems [1-4]. QSH insulators are expected to have two conducting edge channels with quantized electric conductance $2e^2/h$ and opposite spin polarizations, which are robustly protected by the time-reversal symmetry. It could provide a possible alternative to quantum electronic devices with low dissipation. However, because of the limitation of monolayer, the TSS of QSH insulators in TMDs have been not addressed by the experimental tools.

Recently, new stable structure phase 2M-MX_2 have been found with the topological surface state (TSS) and the superconductivity with the highest transition temperature 8.8 K among TMDs [5-10]. Because the crystal structure of bulk 2M phase is identical with monolayer 1T′-MX_2, 2M-MX_2 have a similar band structure and TSS that is similar dispersion with TSS of monolayer 1T′-MX_2. The observation of TSS in 2M-MX_2 can provide the information of topological feature in monolayer 1T′-MX_2 as well as own great interesting feature such as a possible candidate for the QSH insulator and the Majorana bound state together with the superconductivity [11].

We investigated the electronic and spin structure of the TSS in 2M-WS_2 utilizing high-resolution angle- and spin- resolved photoemission spectroscopy. The low-energy photoemission spectra taken from the laser-based ARPES with 6.994 eV photons clearly describe the fine dispersion of the topological surface state with the higher momentum resolution in Fig. 1(a). The hole-like band dispersion near the $k_y = 0$ is corresponding to the lower part of the Dirac cone of topological surface state, and the crossing point is expected to be located above the Fermi level. To show the helical spin structure of the topological surface state, we exploit the spin-resolved ARPES. Figure 1(b) show the spin-resolved EDCs of s_y with red and blue colour code with spin up and spin down, respectively. The result indicates

that the sign of s_y is reversed between k_L and k_R. Moreover, we obtain that the in-plane spin-polarization P_y is reversed between k_L and k_R near the Fermi level, but another spin-polarization P_x and P_z are negligible. It was expected that the topological surface state of 2M-WS_2 show the helical spin texture, thus allowing the opposite spin direction between left and right momentum at the Fermi level. In the view of the Fermi surface as the schematic picture based on our experimental results, the lower Dirac cone branch of the topological surface state in 2M-WS_2 has the helical spin texture with a clockwise rotation as shown in Fig. 1(d). Given the crystal and electronic structural similarity between 2M-WS_2 and monolayer 1T′-MX_2, our results can provide the general knowledge about the edge conductance and spin-based device as manufactured with quantum spin Hall insulator, monolayer 1T′-MX_2.

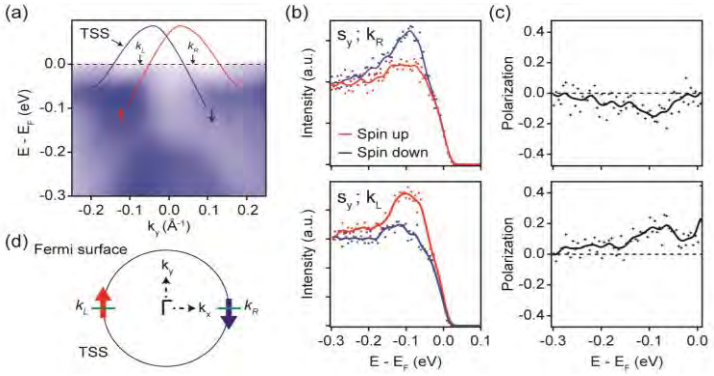

Figure 1(a) ARPES spectra of 2M-WS_2 with the TSS obtained from the band calculation and the possible direction of the spin momentum based on the experimental results. The red (blue) arrow indicates the spin up (down). (b) Spin-resolved EDCs of the TSS at the left and right momentum cuts as marked in (a). The spin-resolved EDCs at k_L and k_R shows spin texture along the S_y direction. (c) Representative spin-polarization magnitude for the TSS at k_L and k_R, whose obtained from the spin-resolved EDCs in (b). (d) Schematic picture of the helical spin texture for the TSS at Fermi surface based on the spin-resolved EDC and polarization. in (b) and (c)

REFERENCES

[1] M. S. Lodge *et al*., Adv. Mater. **2021**, 33, 2008029.
[2] Z. Fei *et al*., Nat. Phys. **2017**, 13 677.
[3] X. Qian *et al*., Science **2014**, 346, 6215.
[4] S. Wu *et al*., Science **2018**, 359, 6371 76.
[5] Y. W. Li *et al*., Nat. Commu. **2021**, 12, 2874.
[6] Y. Fang *et al*., Adv. Mater. **2019**, 31, 1901942.
[7] X. Che *et al*., npj Quantum Mater. **2019**, 4, 50.
[8] L. S. Wang *et al*., Rev. B 2020, 102, 024523.
[9] Y. Fang *et al*., J. Mater. Chem. C **2019**, 7, 8551.
[10] P. Samarawickrama *et al*., ACS Omega **2021**, 6, 4 2966.
[11] Y. Yuan *et al*., Nat. Phys. **2019**, 15 1046.

ENHANCED RASHBA-SPLITTING OF AU(111) SURFACE STATES BY THE MELAMINE HONEYCOMB LAYERS

Rena MOUE[1], Yuta KOKUBO[1], Kozo MUKAI[2], Hirotaka MIZUSHIMA[1], Yuto FUKUSHIMA[2], Kaishu KAWAGUCHI[2], Takeshi KONDO[2,3], Ayumi HARASAWA[2], Jun YOSHINOBU[2], Shik SHIN[2], Kaname KANAI[1]

[1]*Department of Physics, Faculty of Science and Technology,*

[2]*The Institute for Solid State Physics, The University of Tokyo,*

[3]*Trans-scale Quantum Science Institute, The University of Tokyo.*

In quasi-two-dimensional electron systems with broken spatial inversion symmetry, such as metal surfaces and semiconductor interfaces, Rashba-type spin-orbit interactions (Rashba effect) are known to occur through atomic spin-orbit interactions. The Rashba effect has been actually demonstrated in quantum wells and thin films based on III-V semiconductors, as well as in two-dimensional electron gases in the metal surface, and is expected to play an important role as an elemental technology in spintronics.

Many studies have shown that the Rashba coupling can be modified by the adsorption of atoms and molecules on metal surfaces and by distortions at the semiconductor interface. In recent years, it has become possible to intentionally control the strength of the Rashba coupling and design systems for various applications. For example, adsorption of noble gases or organic molecules on noble metal (111) changes the strength of the Rashba coupling[1].

Organic materials such as metal-organic frameworks (MOFs) and covalent organic frameworks have been extensively studied over the past few decades and are potentially attractive for a variety of applications, including gas storage and separation, catalysis, chemical sensors, and drug delivery[2]. On the other hand, new porous materials called hydrogen-bonded organic frameworks (HOFs), which are constructed from pure organic or metal-containing organic building blocks by hydrogen bonds, have recently attracted much attention. Although many pioneering studies have been conducted on HOFs, their progress has lagged behind that of MOFs and others. The main reason for the lag is that the structure of many HOFs collapses when solvent molecules are removed from the pores formed by weak hydrogen bonds. On the other hand, the instability of HOFs is caused by weak hydrogen bonds, but on the contrary, they are rather flexible compared to strong covalent or coordination bonds. The use of this soft hydrogen bond is also beneficial for the flexibility of the framework of porous materials. Carbon nitride molecules such as melamine (1,3,5-Triazine-2,4,6-triamine) and melem (2,5,8-triamino-heptazine) are typical supramolecular species that form HOFs through highly electronegative nitrogen-mediated hydrogen bonds. The studies in these HOFs are rather well known for cyanuric acid and melamine complexes, which have been studied for many years, where cyanuric acid and melamine are combined by N-H···O and N-H···N hydrogen bonds to form rosette-shaped superstructure[3]. On the other hand, melamine and melem are known to readily form highly oriented monolayers consisting of two-dimensional ordered supramolecular structures by adsorption on metal surfaces (surface HOF: SHOF), without the help of solvent molecules. This is probably due in large part to the flexibility of hydrogen bonding. Surfaces modified by such supramolecular structures are becoming powerful tools in applications such as chemical sensors and nanoelectronics, thanks to their ability to exhibit molecular recognition features. However, melamine is one of the most basic units in the systems that create such SHOFs, but even for the structure of the SHOFs of melamine, the determination of their structures remains arbitrary so far, although there are a few reported studies using STM[4]. Furthermore, there are no reported studies that have conducted detailed investigations of the formation process of melamine SHOFs, their electronic structure, or their interfacial electronic structure with metal surfaces. Therefore, even now, many problems remain in understanding the basic physical properties of melamine SHOFs as a prototype of SHOF.

In this study, we determine the formation process and the structure of melamine SHOFs on Au(111) by X-ray photoemission spectroscopy (XPS), low-energy electron diffraction (LEED) and their effect on the Au(111) surface electronic structure by angle-resolved photoemission spectroscopy (ARPES) and spin-resolved and angle-resolved photoemission spectroscopy (SARPES). The SHOF formed when melamine adsorbs on Au(111) is a simple but most typical system, so clarifying its formation is inevitable for understanding the formation of other SHOFs. From the LEED results shown in Figure 1, melamine, upon adsorption on Au(111), immediately forms a unique hexagonal SHOF through cooperative intermolecular hydrogen bonds. Many other organic molecules, whose main cohesive force is dispersion force, do not form such cooperative superstructures and usually involve molecular deformation upon adsorption to a surface, but in the case of melamine SHOFs, molecular deformation is minimized by multiple hydrogen bonds between the molecules. The SHOF retains its two-dimensionality, like graphene adsorbed on Au(111). Theoretical calculations also show that the SHOF induces a slight, but obvious, change in the position of nuclei in the outermost layer of Au(111) in the surface vertical direction. This indicates that there is strong orbital mixing between SHOF and Au(111), meaning that SHOF forms a new periodic potential on the surface. Such a strong coupling between the SHOF and the metal surface electron system has a significant effect on the electronic structure of the surface electron system, leading to a reconfiguration of the surface charge density and a modulation of the electrostatic potential in the outermost layers of the surface. As a result, it is shown to significantly enhance Rashba coupling in Shockley state (SS) of Au(111). The conclusions drawn here indicate that SHOF may provide new guidelines in the manifestation of the spin-galvanic effect, the Edelstein effect, and the inverse Edelstein effect, which are attracting attention as elemental technologies in spintronics.

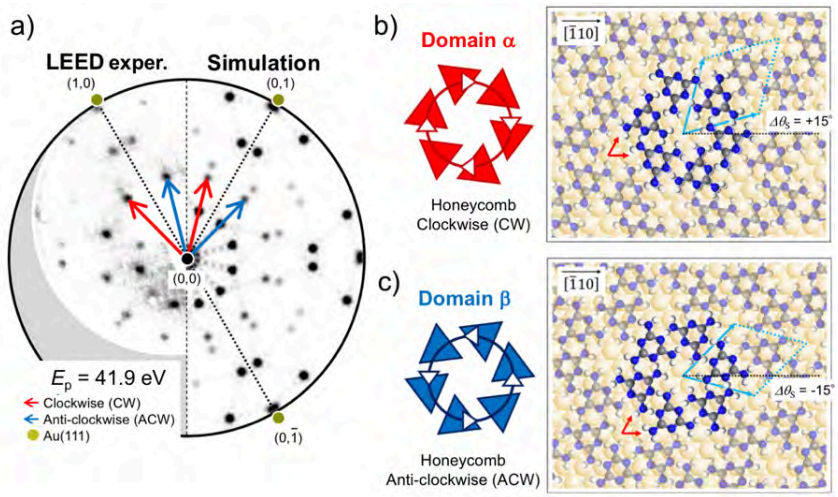

Figure 1. a) Experimental and simulated LEED results for melamine/Au(111). The left half of the circle shows the LEED pattern observed at primary energy of E_p = 41.9 eV; the right half of the circle shows the simulated LEED pattern. Red and blue arrows indicate diffraction spots from two domains α and β with different pseudo-chirality, respectively. b) Schematic drawing of the adsorption structure of domains α and β of melamine/Au(111).

REFERENCES

[1] For example, F. Forster *et al*., Surf. Sci., 2006, **600**, 3870–3874
[2] For example, H. Li, M. Eddaoudi *et al*., Nature, 1999, **402**, 276–279
[3] For example, S. J. Makowski *et al*., Chem. Eur. J. 2012, **18**, 3248–3257
[4] For example, P. A. Staniec *et al*., J. Phys. Chem. C, 2007, **111**, 886-893

ELECTRONIC STATES OF TOPOLOGICAL SEMIMETALS STUDIED BY SPIN- AND ANGLE-RESOLVED PHOTOEMISSION SPECTROSCOPY

Y.X. Wan[1], K. Kuroda[1], C. Bareille[1], Y. Ishida[1], A. H. Mayo[2,3], H. Takahashi[2, 3], M. S. Bahramy[1,4], C. Lin[1], Y. Arai[1], H. Tanaka[1], Y.Y. Dong[1], M. Hashimoto[5], D.H. Lu[5], T. Muro[6], S. Ishiwata[2, 3], T. Kondo[1]

[1]*The Institute for Solid State Physics, The University of Tokyo*

[2]*Department of Applied Physics, The University of Tokyo*

[3]*Graduate School of Engineering Science, Osaka University*

[4]*Center of Spintronics Research Network (CSRN), Osaka University*

[5]*Department of Physics and Astronomy, The University of Manchester*

[6]*Stanford Synchrotron Radiation Lightsource, SLAC National Accelerator Laboratory*

[7]*Japan Synchrotron Radiation Research Institute (JASRI)*

INTRODUCTION

By breaking the time reversal symmetry in Dirac semimetals, one would obtain topological Weyl semimetals or nodal line semimetals [1]. However, usually only extremely large external magnetic field can realize such topological phase transition, which is challenging in the laboratory. A layered phosphide, EuP_3, has been reported to archive topological phase transition when external magnetic field is applied: it would be a magnetic Weyl semimetal in perpendicular magnetic field, but nodal-line semimetal in in-plane magnetic field [2]. This material has drawn increasing attention for it can be an ideal platform to study the topological phase transition, as well as its promising application in engineering.

We have observed of the band structure in α-EuP_3 by angle-resolved photoemission spectroscopy (ARPES) with synchrotron lightsource. We used resonant photoemission to directly confirm the *f-p* coupling. Further, with the high-resolution ARPES, we discovered an unexpected band splitting in the valence band. This band splitting occurs only along k_y direction without any global symmetry breaking. To compare with the results, we also measured an isostructural material SrP_3, and found similar splitting. This result suggests that the crystal structure contributes to the band splitting. We need to confirm whether this kind of band splitting is intrinsic by measure their spin texture with SARPES.

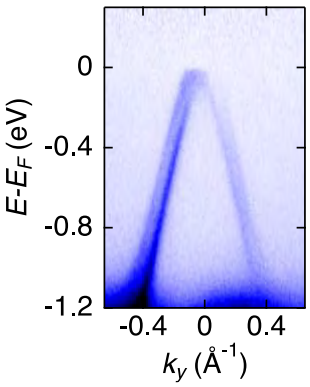

Fig.1 Band dispersion of EuP_3, showing an unconventional splitting.

EXPERIMENTS

During the experiment, all EuP_3 and SrP_3 samples were cleaved *in situ* with top posts, and the *ab* plane [(001) surface] was exposed and measured. The *ab* plane is flat and shiny, suggesting that the compounds is metallic. It should be noted that there is another cleavage except (001) surface but no band dispersion can be observed from that.

The experiment was carried out with the spin-resolved laser ARPES (SARPES) at ISSP, the

University of Tokyo. The light source is 7 eV laser from KBBF crystal.

RESULTS

We measured the in-plane spin texture of EuP_3 and SrP_3. Although due to the matrix element effect, we cannot directly observe the two splitting band dispersions, we found that the valence bands are spin-polarized. The spin textures of both materials are Dresselhaus-like, suggesting the space reversion symmetry is broken by unknown mechanism. However, we need further study to confirm whether the splitting is a combination of Dresselhaus and Zeeman effects because we have not excluded the out-of-plane spin polarization. μSR can directly demonstrate direct evidence of the spin fluctuation [3]. We also need theoretical study to explain why Dresselhaus effect occurs in the centrosymmetric EuP_3 and SrP_3 crystals.

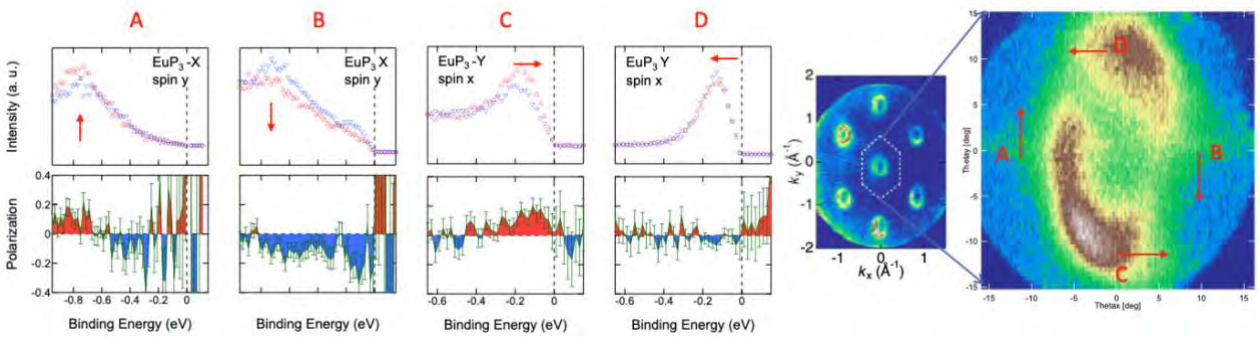

Fig. 2 Spin texture of EuP_3. The valence band is spin-polarized along both *x* and *y* directions, suggesting a Dresselhaus-like band splitting.

REFERENCES

[1] M. Koshino *et al.*, *Phys. Rev. B* **93**, 045201 (2016)

[2] A. H. Mayo *et al.*, *Phys. Rev. X* **12**, 011033 (2022)

[3] J. Z. Ma *et al.*, *Sci. Adv.* **5**, eaaw4718 (2019).

LASER-SARPES STUDY OF SPIN-POLARIZED ELECTRONIC STATES FOR $PB(BI_{1-X}SB_X)_2TE_4$

Koichiro YAJI[1], Yuya HATTORI[2], Shunsuke YOSHIZAWA[1], Shunsuke TSUDA[1], Youhei YAMAJI[3], Yuto FUKUSHIMA[4], Kaishu KAWAGUCHI[4], Takeshi KONDO[4], Yuki TOKUMOTO[5], Keiichi EDAGAWA[5], and Taichi TERASHIMA[2]

[1]*Research Center for Advanced Measurement and Characterization, NIMS*

[2]*International Center for Materials Nanoarchitectonics, NIMS*

[3]*Center for Green Research on Energy and Environmental Materials, NIMS*

[4]*Institute for Solid State Physics, The University of Tokyo*

[5] *Institute of Industrial Science, The University of Tokyo*

The formation mechanism of a topological surface state (TSS) is well established, where the bulk band inversion between the top of the valence band and the bottom of the conduction band is required. The phase transition from a trivial insulator to a topological insulator is known as a topological phase transition. The topological phase transition can be controlled by tuning the composition, the lattice constant, and the film thickness of the system [1-4]. Understanding the modification in an electronic structure induced by topological phase transitions is essential not only for fundamental interests but also for applications.

A family of Pb-based ternary compounds, $Pb(Bi_{1-x}Sbx)_2Te_4$, has been revealed to be topological insulators [5-8]. In the previous angle-resolved photoemission spectroscopy (ARPES) studies [7,8], the TSSs above a Dirac point (DP) have been clearly observed, where the TSSs exist in a projected bulk band gap. On the other hand, the dispersive feature is unclear below DP, which might be due to the existence of the bulk electronic states in the close vicinity of the TSSs. In addition, no spin-resolved ARPES (SARPES) study has been reported so far.

In the present study, we have investigated spin-polarized electronic states of $Pb(Bi_{1-x}Sb_x)_2Te_4$ (x = 0.70, 0.79) by SARPES using a laser (laser-SARPES). Our laser-SARPES reveals Rashba-type occupied surface resonances near the TSSs. Besides, the TSSs continuously connects to a branch of the Rashba-type surface resonances. Our results provide direct evidence that the present system undergoes the topological phase transition.

Laser-ARPES and -SARPES measurements have been performed at the Institute for Solid State Physics, The University of Tokyo [9]. The samples were cleaved with scotch tape in an ultra-high vacuum chamber below the base pressure of 2.0 x 10^{-8} Pa. The photoelectrons were excited by a quasi-continuous-wave laser with a photon energy of 6.994 eV. The energy resolutions for laser-ARPES and -SARPES were set to 5 and 10 meV, respectively. The sample temperature was kept at 30 K during the measurements.

Figure 1 displays an ARPES intensity map for x = 0.70 taken along the $\bar{\Gamma}\bar{M}$ direction. Overall dispersive features of the TSS and the bulk conduction bands agree with the previous studies [7,8]. The precise band structure near the Dirac point has been demonstrated thanks to the high-resolution laser-ARPES. The Dirac

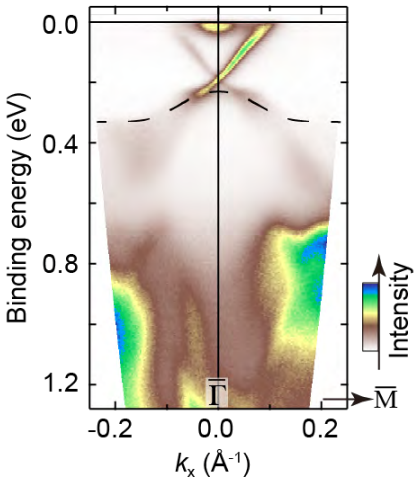

Fig. 1 ARPES intensity map for x = 0.70 along $\bar{\Gamma}\bar{M}$. A dashed curve represents the projected bulk band edge determined by a leading edge of the corresponding photoelectron intensity.

point (DP) is observed at the binding energy of 190 meV. The photoelectron intensity from the TSS in the bulk band gap is prominent. The TSS penetrates into the projected bulk bands at k = ±0.05 Å^{-1}, indicating that the surface states change to surface resonances. The surface resonances disperse in the binding energy range of 0.2-0.5 eV. One can notice here that the spectrum widths of the surface resonances are broadened compared with those of the TSSs. We also find several bands below $E_B \sim 0.7$ eV.

Laser-SARPES measurements have been performed for x = 0.70 and x = 0.79 samples [Fig. 2(a,b)] in the $\bar{\Gamma}\bar{M}$ direction with a p-polarized light. The dispersive feature for x=0.79 is quite similar to that for x = 0.70. Here, the DP for x=0.79 is located above E_F. The observed spin direction is inverted with respect to the $\bar{\Gamma}$ point, meaning the TSSs possess a helical spin texture. More interestingly, spin components opposite to the TSS are observed below DP, corresponding to the spin textures of the surface resonances.

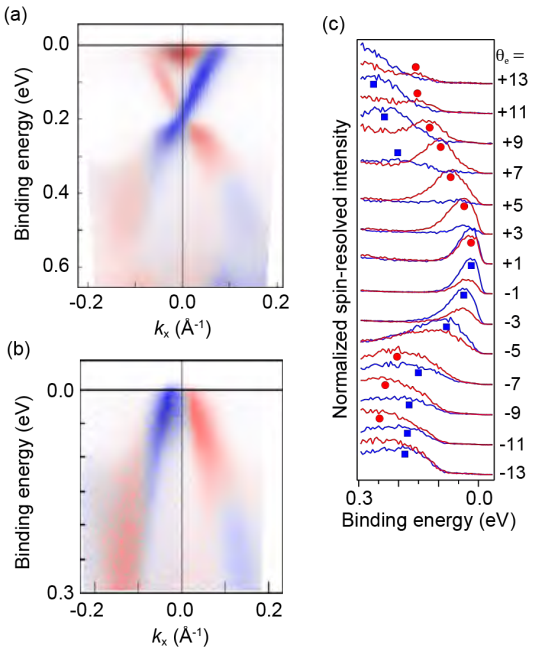

Fig. 2 SARPES images for (a) x = 0.70 and (b) x = 0.79 along $\bar{\Gamma}\bar{M}$. (c) Spin- and angle-resolved spectra for x = 0.79.

The band structures of the TSS and the surface resonances are identified from spin-resolved energy distribution curves [Fig. 2(c)]. The surface resonances are spilt into two in the energy direction in |k| = 0.1–0.2 Å^{-1}. The surface resonance that appears in the lower binding energy side possesses the same spin orientation as the TSS. Another surface resonance dispersing in the energy range of 0.2–0.3 eV possesses the spin direction opposite to that of the counterpart.

In addition, the spin polarizations of the surface resonances are inverted with respect to the $\bar{\Gamma}$ point. Thus, we conclude that the surface resonances exhibit the Rashba-type spin splitting. More importantly, the upper branch of the surface resonances is continuously connected to the TSS. Our result provides direct evidence that the system undergoes the topological phase transition.

REFERENCES

[1] S.-Y. Xu *et al*., Science **332**, 560 (2011).
[2] M. Brahlek *et al*., Phys. Rev. Lett. **109**, 186403 (2012).
[3] Y. Zhang *et al*., Nat. Phys. **6**, 584 (2010).
[4] C. Lin *et al.*, Nat. Mater. **20**, 1093 (2021).
[5] T. V. Menshchikova *et al*., JETP Lett. **93**, 15 (2010).
[6] H. Jin *et al*., Phys. Rev. B **83**, 041202(R) (2011).
[7] S. Souma *et al*., Phys. Rev. Lett. 108, 116801 (2012).
[8] K. Kuroda *et al*., Phys. Rev. Lett. **108**, 206803 (2012).
[9] K. Yaji *et al.*, Rev. Sci. Instrum. **87**, 053111 (2016).

ELECTRONIC STRUCTURES OF HALF-METALLIC FERROMAGNET $La_{1-x}Sr_xMnO_3$ BY HIGH-RESOLUTION SPIN-RESOLVED PHOTOEMISSION SPECTROSCOPY

T. Setoguchi[1], N. Kataoka[1], K. Kawaguchi[2], Y. Fukushima[2], A. Harasawa[2], K. Kuroda[2], T. Kondo[2], S. Shin[2], T. Wakita[1,3], Y. Muraoka[1,3], and T. Yokoya[1,3]

[1]*Graduate School of Natural Science and Technology, Okayama University, Okayama 700-8530, Japan*

[2]*Institute for Solid State Physics, The University of Tokyo, Kashiwa, Chiba 277-8581, Japan*

[3]*Research Institute for Interdisciplinary Science, Okayama University, Okayama 700-8530, Japan*

Half metallic ferromagnets have a unique spin dependent electronic structure near the Fermi level (E_F), where only one of the spin states cross E_F [1]. The unique electronic structure gives rise to many body effects different from other systems. Theoretically, the electronic states induced by many-body effects in half metals has been proposed as non quasiparticle (NQP) states [2]. The experimental verification for NQP states has been made recently for a half metallic ferromagnet CrO_2 by using high-resolution (HR) spin-resolved photoemission spectroscopy (SRPES) [3]. In the present research, we have performed HRSRPES of another half metallic ferromagnet $La_{1-x}Sr_xMnO_3$ to experimentally explore the characteristics and universality of NQP states. $La_{1-x}Sr_xMnO_3$ is one of the famous perovskite materials, exhibiting colossal magnet resistance around Sr concentration x of 0.3. The previous SRPES study has provided evidence for half metallic electronic structure of $La_{1-x}Sr_xMnO_3$ at 40 K[4]

Homoepitaxial films of $La_{1-x}Sr_xMnO_3$ were grown on the atomically-flat (001) surface of Nb-doped $SrTiO_3$ substrates using a laser MBE method. Laser-based SRPES experiments were performed at the Institute for Solid State Physics, The University of Tokyo [7]. The *p*-polarized light with $h\nu = 6.994$ eV was used to excite the photoelectrons. Photoelectrons were analyzed with a combination of a ScientaOmicron DA30L analyzer and a very-low-energy-electron-diffraction (VLEED) type spin detector. The energy and angular resolutions were set to 6 meV and 0.3˚ (corresponding to ~0.005 Å) for spin-integrated ARPES and 10 meV and 1˚ (corresponding to ~0.02 Å) for SARPES, respectively. During the measurement, the instrumental energy resolution was set to 20 meV and the base pressure was kept below 1×10^{-8} Pa. Calibration of E_F for the samples was achieved using a gold reference. The data were taken at $T = 20$, 50, 100 and 150 K. Clean surfaces of the samples for all measurements were obtained by *in situ* annealing at 200℃ for 20 minutes. We magnetized the LSMO(001) sample along the

magnetic easy axis ([110] direction) by bringing the sample close to a magnet . The approximate magnitude of the magnetic field at the sample position was 700 Oe.

We obtained HRSRPES data at 20, 50, 100, and 150K. Compared to the minority spin states showing negligible intensity around the near-E_F region, the minority spin states have enhanced intensity with a Fermi edge at all measured temperatures. These results are in line with the previous SRPES studies reporting that LSMO is a half metallic ferromagnet. However, we found that polarization is slightly smaller than 100%. We tentatively attribute the reduced polarization to detecting the information of the substrate. We plan to measure HRARPES with thicker films in the future experiment.

ACKNOWLEDGEMENT

This work was partially supported by JSPS KAKENHI Grand Numbers (JP20H0185313) from MEXT. We acknowledge M. Minohara and H. Kumigashira for providing the samples.

REFERENCES

[1] M.I. Katsnelson et al., Rev. Mod. Phys. **80**, 315-378 (2008).
[2] V.Y. Irkhin and M.I. Katsnelson, Usp. Fiz. Nauk **164**, 705 (1994).
[3] H. Fujiwara et al., Phys. Rev. Lett. **121**, 257201 (2018).
[4] J.-H. Park et al., Nature **392**, 794-796 (1998).
[5] K. Yaji *et al*., Rev. Sci. Instrum. **87**, 053111 (2016).

5. Staff

Director: HARADA Yoshihisa, Professor

MATSUDA Iwao, Professor

KIMURA Takashi, Associate Professor
KONDO Takeshi, Associate Professor
HAYASHI Tomohiro, Visiting Associate Professor
KURODA Kenta, Research Associate (~2021.8)
HORIO Masafumi, Research Associate
KIUCHI Hisao, Research Associate
TAKEO Yoko, Research Associate
HARASAWA Ayumi, Senior Technical Specialist
SHIBUYA Takashi, Technical Specialist
KUDO Hirofumi, Technical Specialist

Project Academic Specialist:
FUKUSHIMA Akiko
KOSEGAWA Yuka
ARAKI Mihoko

Secretary:
AIHARA Yumiko
YOSHIZAWA Motoko
TSUTSUMI Yumiko
IKEDA Kuniko
TERAMOTO Tomoka

Project Researcher:
OSHIMA Masaharu
OHDAIRA Takeshi
ZHANG Wenxiong
KURAHASHI Naoya
KITAKATA Emi
Al Samarai Mustafa (2021.8~)
LIU Daobin (2021.9~)
NIIBE Masahito (2021.10~)
TATSUTA Kazuo (2021.10~)
ANDO Hiroshi (2021.11~)

Graduate Student:
UGALINO Ralph John
SATO Yusuke
TSUJIKAWA Yuki
YANG Tianqi
ZHAO Yuhao (~2021.9)
KAMEDA Ayako
KUDO Yoshiki
SUMI Toshihide
WADA Tetsuya
LI Hao
ZHANG Xiaoni
ZHAO Haochong
FURUYA Noboru
SAKURAI Kai
SENOO Tomoaki
YIN Heming

Harima Paper 2021

No	Title	Authors	Journal	Vol.	No.	Page	Year
1	Functionalization of the MoS−−−2 basal plane for activation of molecular hydrogen by Pd deposition	Fumihiko Ozaki, Shunsuke Tanaka, Wataru Osada, Kozo Mukai, Masafumi Horio, Takanori Koitaya, Susumu Yamamoto, Iwao Matsuda, Jun Yoshinobu	Applied Surface Science	593		153313	2022
2	Soft X-ray ptychography system using a Wolter mirror for achromatic illumination optics	Takashi Kimura, Yoko Takeo, Kai Sakurai, Noboru Furuya, Satoru Egawa, Gota Yamaguchi, Yusuke Matsuzawa, Takehiro Kume, Hidekazu Mimura, Mari Shimura, Haruhiko Ohashi, Iwao Matsuda, Yoshihisa Harada	Optics Express	30	15	26220-26228	2022
3	Materials Science Research by Ambient Pressure X-Ray Photoelectron Spectroscopy Systems at Synchrotron Radiation Facilities in Japan: Applications in Energy, Catalysis, and Sensors	Susumu Yamamoto, Yasumasa Takagi, Takanori Koitaya, Ryo Toyoshima, Masafumi Horio, Iwao Matsuda, Hiroshi Kondoh, Toshihiko Yokoyama & Jun Yoshinobu	Synchrotron Radiation News	35	3	19-25	2022
4	Operando resonant soft X-ray emission spectroscopy of LiMn2O4 cathode using an aqueous electrolyte solution	Daisuke Asakura, Yusuke Nanba, Hideharu Niwa, Hisao Kiuchi, Jun Miyawaki, Masashi Okubo, Hirofumi Matsuda, Yoshihisa Harada, Eiji Hosono	Phys. Chem. Chem. Phys.	24		19177-19183	2022
5	Hole Dynamics in Photoexcited Hematite Studied with Femtosecond Oxygen K-edge X-ray Absorption Spectroscopy	Yohei Uemura, Ahmed S. M. Ismail, Sang Han Park, Soonnam Kwon, Minseok Kim, Hebatalla Elnaggar, Federica Frati, Hiroki Wadati, Yasuyuki Hirata, Yujun Zhang, Kohei Yamagami, Susumu Yamamoto, Iwao Matsuda, Ufuk Halisdemir, Gertjan Koster, Christopher Milne, Markus Ammann, Bert M. Weckhuysen, and Frank M. F. de Groot	J. Phys. Chem. Lett.	13	19	4207-4214	2022
6	雰囲気軟 X 線光電子分光を用いた触媒表面反応のオペランド計測	山本達、小板谷貴典、松田巌、吉信淳	放射光	35		182	2022
7	Electronic Structure of Carbon Dioxide in Sylgard-184 evaluated by using X-ray Emission Spectroscopy	Ryosuke Matsuno, Yokajaksusri Nutthon, Akira Miyano, Kakeru Ninomiya, Maiko Nishibori, Hisao Kiuchi, Shigenori Fujikawa, Yoshihisa Harada, Atsushi Takahara	Chem. Lett.	51	6	650-653	2022
8	Editorial: Interfacial Water：A Physical Chemistry Perspective, Volume II	Yoshihisa Harada	Front. Chem.	10		896586	2022
9	オペランド軟X線発光分光で見るリチウムイオン電池負極材料のコンバージョン反応	朝倉大輔、細野英司、原田慈久	電気化学	90	1	44660	2022
10	磁場中共鳴非弾性軟X線散乱によるハーフメタル型ホイスラー合金のスピン偏極電子構造研究	藤原秀紀、梅津理恵、宮脇淳、原田慈久、菅滋正	放射光	35	2	78-87	2022
11	放射光を用いた固体高分子型燃料電池正極触媒のオペランド解析	尾嶋正治、原田慈久	燃料電池	21	3	44755	2022
12	6-GHz lattice response in a quantum spin-orbital liquid probed by time-resolved resonant x-ray scattering	Kou Takubo, Takashi Mizokawa, Huiyuan Man, Kohei Yamamoto, Yujun Zhang, Yasuyuki Hirata, Hiroki Wadati, Daniel I. Khomskii, Satoru Nakatsuji	Phys. Rev. B	104		205110	2021
13	Critical In-plane Density of Polyelectrolyte Brush for the Ordered Hydrogen-bonded Structure of Incorporated Water	Kosuke Yamazoe, Yuji Higaki, Yoshihiro Inutsuka, Jun Miyawaki, Atsushi Takahara, Yoshihisa Harada	Langmuir	38	10	3076-3081	2022
14	Interpretation of the x-ray emission spectra of liquid water through temperature and isotope dependence	Osamu Takahashi, Ryosuke Yamamura, Takashi Tokushima, Yoshihisa Harada	Phys. Rev.Lett.	128	8	086002	2022
15	Identification of Valence Electronic States Reflecting the Hydrogen Bonding in Liquid Ethanol	Ryosuke Yamamura, Kosuke Yamazoe, Jun Miyawaki, Yoshihisa Harada, Osamu Takahashi	J. Phys. Chem. B	126	5	1101-1107	2022
16	Hydration Mechanism in Blood-Compatible Polymers Undergoing Phase Separation	Daiki Murakami, Kosuke Yamazoe, Shin-nosuke Nishimura, Naoya Kurahashi, Tomoya Ueda, Jun Miyawaki, Yuka Ikemoto, Masaru Tanaka, Yoshihisa Harada	Langmuir	38	3	1090-1098	2022

17	Hydrogen Absorption and Diffusion Behaviors in Cube-Shaped Palladium Nanoparticles Revealed by Ambient-Pressure X-ray Photoelectron Spectroscopy	J. Tang, O. Seo, D. S. R. Rocabado, T. Koitaya, S. Yamamoto, Y. Nanba, C. Song, J. Kim, A. Yoshigoe, M. Koyama, S. Dekura, H. Kobayashi, H. Kitagawa, O. Sakata, I. Matsuda, J. Yoshinobu	Applied Surface Science	587		152797	2022
18	Growth of MoS2-Nb-doped MoS2 lateral homojunctions: A monolayer p?n diode by substitutional doping	Mitsuhiro Okada, Naoka Nagamura, Tarojiro Matsumura, Yasunobu Ando, Anh Khoa Augustin Lu, Naoya Okada, Wen-Hsin Chang, Takeshi Nakanishi, Tetsuo Shimizu, Toshitaka Kubo, Toshifumi Irisawa, Takatoshi Yamada	APL Materials	9		121115(1-10)	2021
19	Fast and versatile polarization control of X-ray by segmented cross undulator at SPring-8	Jun Miyawaki, Susumu Yamamoto, Yasuyuki Hirata, Masafumi Horio, Yoshihisa Harada Iwao Matsuda	AAPPS Bulletin	31	25	44585	2021
20	Soft X-Ray Emission Studies on Hydrate-Melt Electrolytes	Tatau Shimada, Norio Takenaka, Eriko Watanabe, Yuki Yamada, Yi-Tao Cui, Yoshihisa Harada, Masashi Okubo, Atsuo Yamada	J. Phys. Chem. B	125	41	11534-11539	2021
21	Comparative Study of H2O and O2 Adsorption on the GaN Surface	Masahiro Sato, Yuki Imazeki, Takahito Takeda, Masaki Kobayashi, Susumu Yamamoto, Iwao Matsuda, Jun Yoshinobu, Yoshiaki Nakano, Masakazu Sugiyama	The Journal of Physical Chemistry C	125	46	25807–25815	2021
22	Hydrogen-bonded structure of water in the loop of anchored polyrotaxane chain controlled by anchoring density	Keishi Akada, Kosuke Yamazoe, Jun Miyawaki, Rina Maeda, Kohzo Ito, Yoshihisa Harada	Frontiers in Chemistry	9		743255	2021
23	Detecting halfmetallic electronic structures of spintronic materials in a magnetic field	H. Fujiwara, R.Y. Umetsu, F. Kuroda, J. Miyawaki, T. Kashiuchi, K. Nishimoto, K. Nagai, A. Sekiyama, A. Irizawa, Y. Takeda, Y. Saitoh, T. Oguchi, Y. Harada, S. Suga	Scientific reports	11		18654	2021
24	A novel measurement approach for near-edge x-ray absorption fine structure: Continuous 2π angular rotation of linear polarization	Yoshiki Kudo,Yasuyuki Hirata,Masafumi Horio,Masahito Niibe,Iwao Matsuda	Nucl. Instrum. Methods Phys. Res. A	1018		165804	2021
25	Electronic Surface Reconstruction of TiO2 Nanocrystals Revealed by Resonant Inelastic X-ray Scattering	Cheng-Hao Chuang, Chieh-Ming Chen, Yu-Cheng Shao, Ping-Hung Yeh, Chih-Ming Chang, Way-Faung Pong, Mukes Kapilashrami, Per-Anders Glans, Sheraz Gul, Gongming Wang, Yat Li, Jin Zhang, Jun Miyawaki, Hideharu Niwa, Yoshihisa Harada, Jin-Ming Chen, Jinghua Guo	Journal of Vacuum Science & Technology A	39	6	63204	2021
26	ビスマス薄膜を通して「見る」表面物理学の新展開	伊藤　俊，松田　巌	日本物理学会誌	76	9	566-574	2021
27	Electronic structure of a borophene layer in rare-earth aluminum/chromium boride and its hydrogenated derivative, borophane	Masahito Niibe, Mathis Cameau, Nguyen Thanh Cuong, Omeji Ilemona Sunday, Xiaoni Zhang, Yuki Tsujikawa, Susumu Okada, Kunio Yubuta, Takahiro Kondo, and Iwao Matsuda	Phys. Rev. Materials	5	8	84007	2021
28	「計測インフォマティクスを応用したX線顕微分光によるナノ表界面分析」	永村直佳, 松村太郎次郎, 永田賢二, 赤穂昭太郎, 安藤康伸	表面と真空	64	8	382-389	2021
29	【水】と機能性ポリマーに関する材料設計・最新応用, 第2章 第2節 "高分子内に入り込んだ水の電子状態観測"	倉橋直也、山添康介	技術情報協会	2116		42-52	2021
30	Extreme Ultraviolet Second Harmonic Generation in a Polar Metal	Emma Berger*, Sasawat Jamnuch, Can B. Uzundal, Clarisse Woodahl, Hari Padmanabhan, Angelique Amado, Paul Manset, Yasuyuki Hirata, Yuya Kubota, Shigeki Owada, Kensuke Tono, Makina Yabashi, Cuixiang Wang, Youguo Shi, Venkatraman Gopalan, Craig P. Schwartz, Walter S. Drisdell, Iwao Matsuda, John W. Freeland, Tod A. Pascal, and Michael Zuerch	Nano Lett	21	14	6095–6101	2021
31	Spin-orbital liquid in Ba3CuSb2O9 stabilized by oxygen holes	Kou Takubo, Huiyuan Man, Satoru Nakatsuji, Kohei Yamamoto, Yujun Zhang, Yasuyuki Hirata, Hiroki Wadati, Akira Yasui, Takashi Mizokawa, and Daniel I. Khomskii	Phys. Rev. Materials	5	7	75002	2021

32	A Global Shutter Wide Dynamic Range Soft X-Ray CMOS Image Sensor with Backside-Illuminated Pinned Photodiode, Two-Stage Lateral Overflow Integration Capacitor and Voltage Domain Memory Bank	Hiroya Shike, Rihito Kuroda, Ryota Kobayashi, Maasa Murata, Yasuyuki Fujihara, Manabu Suzuki, Shoma Harada, Taku Shibaguchi, Naoya Kuriyama, Takaki Hatsui, Jun Miyawaki, Tetsuo Harada, Yuichi Yamasaki, Takeo Watanabe, Yoshihisa Harada, Shigetoshi Sugawa	IEEE Transactions on Electron Device	68	4	2056-2063	2021
33	放射光オペランド計測の近未来：軟 X 線吸収・発光分光の発展と機能材料分析	原田慈久	精密工学会誌	87	1	34-38	2021
34	Spectrum adapted expectation-conditional maximization algorithm for extending high-throughput peak separation method in XPS analysis	Tarojiro Matsumura, Naoka Nagamura, Shotaro Akaho, Kenji Nagata, and Yasunobu Ando	Science and Technology of Advanced Materials(STAM) Methods	1		45-55	2021
35	2D boron: Boraphene, Borophene, Boronene	I. Matsuda and K. Wu ed.,	Springer				2021
36	Ion Selectivity of Water Molecules in Subnanoporous Liquid-Crystalline Water-Treatment Membranes: A Structural Study of Hydrogen Bonding	Ryusuke Watanabe, Takeshi Sakamoto, Kosuke Yamazoe, Jun Miyawaki, Takashi Kato, Yoshihisa Harada	Angew. Chem. Int. Ed	59	52	23461-23465	2020

E-labo. Paper 2021

No.	Title	Authors	Journal	Vol.	No.	Page	Year
1	Structure and electronic structure of van der Waals interfaces at a Au(111) surface covered with a well-ordered molecular layer of n-alkanes	Hirotaka Mizushima, Harunobu Koike, Kenta Kuroda, Koichiro Yaji, Ayumi Harasawa, Yukiaki Ishida, Mitsuhiro Nakayama, Kazuhiko Mase, Kozo, Mukai, Tatsuya Kitazawa, Takeshi Kondo, Jun Yoshinobu, Shik Shin, Kaname Kanai	Applied Surface Science	535		147673	2021
2	Evidence for a higher-order topological insulator in a three-dimensional material built from van der Waals stacking of bismuth-halide chains.	Ryo Noguchi, Masaru Kobayashi, Zhanzhi Jiang, Kenta Kuroda, Takanari Takahashi, Zifan Xu, Daehun Lee, Motoaki Hirayama, Masayuki Ochi, Tetsuroh Shirasawa, Peng Zhang, Chun Lin, Cédric Bareille, Shunsuke Sakuragi, Hiroaki Tanaka, So Kunisada, Kifu Kurokawa, Koichiro Yaji, Ayumi Harasawa, Viktor Kandyba, Alessio Giampietri, Alexei Barinov, Timur K. Kim, Cephise Cacho, Makoto Hashimoto, Donghui Lu, Shik Shin, Ryotaro Arita, Keji Lai, Takao Sasagawa, Takeshi Kondo	Nature Materials	20		473	2021
3	Observation and control of the weak topological insulator state in $ZrTe_5$	Peng Zhang, Ryo Noguchi, Kenta Kuroda, Chun Lin, Kaishu Kawaguchi, Koichiro Yaji, Ayumi Harasawa, Mikk Lippmaa, Simin Nie, Hongming Weng, V. Kandyba, A. Giampietri, A. Barinov, Qiang Li, G. D. Gu, Shik Shin & Takeshi Kondo	Nature Comm.	12		406	2021
4	Visualization of the strain-induced topological phase transition in a quasi-one-dimensional superconductor $TaSe_3$	Chun Lin, Masayuki Ochi, Ryo Noguchi, Kenta Kuroda, Masahito Sakoda, Atsushi Nomura, Masakatsu Tsubota, Peng Zhang, Cedric Bareille, Kifu Kurokawa, Yosuke Arai, Kaishu Kawaguchi, Hiroaki Tanaka, Koichiro Yaji, Ayumi Harasawa, Makoto Hashimoto, Donghui Lu, Shik Shin, Ryotaro Arita, Satoshi Tanda & Takeshi Kondo	Nature Materials	20		1093	2021
5	Scaling law for Rashba-type spin splitting in quantum-well films.	Ryo Noguchi, Kenta Kuroda, Mitsuaki Kawamura, Koichiro Yaji, Ayumi Harasawa, Takushi Iimori, Shik Shin, Fumio Komori, Taisuke Ozaki, and Takeshi Kondo.	Physical Review B	104		L180409	2021